Space-Charge Driven Transverse Beam Instabilities in Synchrotrons

Raumladungsinduzierte transversale Strahlinstabilitäten in Synchrotrons
Zur Erlangung des Grades eines Doktors der Naturwissenschaften (Dr. rer. nat.)
vorgelegte Dissertation von Yao-shuo Yuan, M.Sc aus Hebei, China
Tag der Einreichung:

1. Gutachten: Prof. Dr. Oliver Boine-Frankenheim — TU Darmstadt
2. Gutachten: Prof. Dr. Ulrich Ratzinger — Goethe Universität Frankfurt

TECHNISCHE
UNIVERSITÄT
DARMSTADT

Fachbereich Elektrotechnik
und Informationstechnik
Institut für
Theorie Elektromagnetischer Felder

Space-Charge Driven Transverse Beam Instabilities
in Synchrotrons
Raumladungsinduzierte transversale Strahlinstabilitäten in Synchrotrons

Vorgelegte Dissertation von Yao-shuo Yuan, M.Sc aus Hebei, China

1. Gutachten: Prof. Dr. Oliver Boine-Frankenheim TU Darmstadt
2. Gutachten: Prof. Dr. Ulrich Ratzinger Goethe Universität Frankfurt

Tag der Einreichung:

Darmstadt — D 17

URN: urn:nbn:de:tuda-tuprints-82155
URL: http://tuprints.ulb.tu-darmstadt.de/8215

Space-Charge Driven Transverse Beam Instabilities in Synchrotrons

Vom Fachbereich Elektrotechnik und Informationstechnik
der Technischen Universität Darmstadt

zur Erlangung des Grades
eines Doktors der Naturwissenschaften
(Dr. rer. Nat.)

genehmigte Dissertation
von Yao-shuo Yuan M.Sc. aus Hebei, China

1. Gutachter: Prof. Dr. Oliver Boine-Frankenheim
2. Gutachter: Prof. Dr. Ulrich Ratzinger

Tag der Einreichung: 27.04.2018
Tag der mündlichen Prüfung: 06.11.2018

Darmstadt 2018
D17

Erklärung zur Dissertation

Hiermit versichere ich, die vorliegende Dissertation ohne Hilfe Dritter nur mit den angegebenen Quellen und Hilfsmitteln angefertigt zu haben. Alle Stellen, die aus Quellen entnommen wurden, sind als solche kenntlich gemacht. Diese Arbeit hat in gleicher oder ähnlicher Form noch keiner Prüfungsbehörde vorgelegen.

Darmstadt, den November 27, 2018

(Yao-shuo Yuan)

Acknowledgements

At this point of completing this dissertation, I would like to express my gratitude to all the people, who directly or indirectly helped me a lot throughout the whole time of this Ph.D. study.

First of all, I would like to thank Prof. Dr. Oliver Boine-Frankenheim for offering me a PhD position at TEMF in TU-Darmstadt and giving constructive criticism on my work. Due to him, it was possible for me to explore the accelerator science and participate many international conferences. Prof. Oliver Boine-Frankenheim convinced me to publish a lot and to interact as much as possible with other scientists, which opened plenty of opportunities and broadened my knowledge.

I am very grateful to Prof. Dr. Ingo Hofmann. He shared me with his deep understanding of space charge physics, which inspired me to extend my knowledge. He also helped a lot on improving several manuscripts for publication. His patience and diligent work spirit impressed me and inspires me into the future career.

Moreover, I wish to thank Dr. Giuliano Franchetti for the great scientific guidance. Whenever I encountered a problem or got stuck, he had an open door for me and helped me with his extensive knowledge and his advices. Many fruitful discussions with him improved this work.

Special thanks are given to Dr. Sabrina Appel for her help concerning the simulation code. She gave me valuable hints on debugging program.

Further thank goes to Prof. Dr. Ulrich Ratzinger for being the second referee in this thesis, and for his carefully reviewing and correcting of manuscripts for the papers.

Great gratitude is due to the beam dynamics group in GSI and TEMF in TU-Darmstadt. I thank my colleagues in the two teams for collaboration and for the productive environment. By name I wish to thank Dr. Ivan Karpov, Dr. Vladimir Kornilov, Dr. Vera Chetvertkova at GSI, and Dr. Uwe Niedermayer, Dr. Lewin Eidam, Aamna Khan, Jens Harzheim and Aleksandr Andreev at TU-Darmstadt, just to name a few.

I thank Dr. Stefan Sorge, Dr. William D. Stem, Dr. David Bizzozero and Dr. Markus Kirk for proofreading this thesis.

Additionally, I would like to thank my former Master degree supervisor Prof. Sheng Wang, who guided me into the region of accelerator science.

Last but not least, I would like to express my gratitude to my mother and father, whose constant love supports me pursuing my dreams.

List of publications

The present cumulative dissertation summarizes the essential scientific findings reported in the following articles:

1. Y. S. Yuan, O. Boine-Frankenheim, G. Franchetti and I. Hofmann, “Dispersion-Induced Beam Instability in Circular Accelerators” in *Physical Review Letters* 118, 154801 (2017).

2. Yao-Shuo Yuan, Oliver Boine-Frankenheim, and Ingo Hofmann, “Modeling of second order space charge driven coherent sum and difference instabilities” in *Physical Review Accelerators and Beams*, 20, 104201 (2017).

3. Yao-Shuo Yuan, Oliver Boine-Frankenheim, and Ingo Hofmann, “Intensity limitations due to space charge for bunch compression in synchrotrons”, in *Physical Review Accelerators and Beams*, 21, 074201 (2018).

Zusammenfassung

Intensive Protonen- und Ionenstrahlen in Teilchenbeschleunigern sind von fundamentaler Bedeutung für viele Forschungsgebiete, die auf solchen Strahlen beruhen, wie beispielsweise solche, die Spallationsneutronen oder radioaktive Strahlen erfordern. Der Gegenstand der vorliegenden Arbeit ist die Untersuchung von Bewegung und Stabilität intensiver Strahlen in Beschleunigern, insbesondere in Ringbeschleunigern. Die Untersuchungen basieren auf zwei Methoden, so genannten particle-in-cell (PIC) simulationen und auf numerischen Methoden zur Berechnung der Bewegung der Strahlenveloppe. Für erstere wurde das Computerprogramm PyORBIT verwendet. Für letztere wurde das weit verbreitete zweidimensionale Strahlenveloppenmodell um eine Dispersionsgleichung erweitert, um die kohärente Beweung des Strahles unter gleichzeitigem Einfluss von Raumladung und Dispersion in Ringbeschleunigern zu beschreiben. Die vollständige numerische Lösung des erweiterten Enveloppenmodells zeigt, dass neben den wohlbekannten Enveloppenschwingungen eine weitere kohärente Schwingungsart existiert, nämlich die Dispersionsschwingung. Die auf Störungsrechnung basierende Analyse der Strahlstabilität zeigt, dass für einen Phasevorschub von mehr als 120° und genügend hohe Intensität die Dispersionsschwingung instabil wird und die neu entdeckte 120°-Dispersionsinstabilität hervor ruft. Diese numerischen Ergebnisse wurden mit PIC-Simulationen validiert. Es wurde gute Übereinstimmung gefunden.

Die so-genannte bunch compression is ein übliches Schema, um durch schnelle Rotation eines Teilchenpaketes im longitudinalen Phasenraum kurze intensitve Teilchenpakete für verschiedene Anwendungen zu erzeugen. In dieser Arbeit wurden die transversalen Envoppengleichungen unter Einbeziehung der Dispersion mit der longitudinalen Enveloppengleichung gekoppelt, um die dreidimensionale Bewegung eines Teilchenpakets während der bunch compression zu beschreiben. Außerdem wird eine Analyse der relevanten raumladungsgetriebenen Strahlinstabilität und der Teilchenresonanzphänomene während der bunch compression präsentiert, die auf dem dreidimensionalen Enveloppenmodell mit transversal-longitudinaler Kopplung und PIC-Simulationen basiert. Der Mechanismus, der die Dominanz der Strahlinstabilität oder der Teilchenresonanz bewirkt, wird für zwei Fälle diskutiert, bei denen der Phasenvorschub einen bestimmten Wert kreuzt, und auf das GSI-Schwerionensynchrotron SIS-18 angewendet. Es wird gezeigt, dass während der bunch compression eine vierzahlige Einteilchenresonanz angeregt wird, wenn der Phasenvorschub 90° kreuzt. Dagegen wird die kürzlich entdeckte dispersionsgetriebene Instabilität angeregt, wenn der Phasenvorschub 120° kreuzt. Die Übereinstimmung der Ergebnisse des Enveloppenmodells und der PIC-Simulationen zeigt, dass das stop band durch die 120°-Dispersionsinstabilität definiert ist, die daher während der bunch compression vermieden werden sollte.

Diese Arbeit untersucht auch die Stabilität aller möglichen kohärenten Strahlschwingungen zweiter Ordnung mit einem vollständigen System von Zweite-Moment-Schwingungsgleichungen. Ergebnisse werden mit älteren Ergebnissen zu Schwingungsfrequenzen verglichen, die durch Lösung der linearisierten Vlasov-Poisson-Gleichung erhalten wurden. Exzellente Übereinstimmung wurde im Falle der so genannten tilting instability für konstante Fokussierung gefunden, was die Äquivalenz der beiden Modelle bei Berücksichtigung von Störungen bis zur zweiten Ordnung bestätigt. In Strukturen mit periodischer Fokussierung wurden die stop bands der so genannten sum envelope instability erhalten, wobei eine gute Übereinstimmung zu Ergebnissen der PIC-Simulationen gefunden wurde. Dies vervollständigt das Bild der kohärenten Schwingungen zweiter Ordnung in zweidimensionalen Strahlen hoher Intensität.

Abstract

Intense proton or ion beams in charged-particle accelerators are of fundamental importance for many research areas, which relay on such beams, such as those requiring spallation neutrons or radioactive beams. The main subject of this thesis is the detailed investigation of the intense beam motion and instability in synchrotrons, based on two approaches: particle-in-cell (PIC) simulations and the numerical methods for calculating the beam's envelope motion. In the former approach, the accelerator simulation code pyORBIT is employed. In the latter, the widely-used two dimensional (2-D) beam envelope model is extended with a dispersion equation, to describe the beam's coherent motion under the combined effect of space charge and dispersion in circular accelerators. Full numerical solution of the extended envelope model reveals that a new coherent mode, namely, dispersion mode, exists besides the well-known envelope modes. Based on the perturbation theory, the analysis of the beam stability shows that for a phase advance larger than 120° and sufficiently high intensity, the dispersion mode becomes unstable, and induces the newly discovered "120° dispersion instability". These numerical results were validated with PIC simulations, showing good agreement.

Bunch compression achieved via a fast bunch rotation in longitudinal phase space is a well-accepted scheme to generate short, intense ion bunches for various applications. In this thesis, the set of transverse envelope equations including dispersion are coupled with the longitudinal envelope equation to describe the three dimensional (3-D) beam motion during bunch compression. Furthermore, based on the 3-D coupled envelope model and PIC simulations, an analysis of the relevant space-charge driven beam instability and the particle resonance phenomena during bunch compression is presented. The agreement between the envelope and PIC results indicates that the stop band of the 120° dispersion instability should be avoided during bunch compression.

This work also investigates the stability of all possible second order coherent modes of beams, with a complete set of second-moment oscillation equations. Results are compared with earlier results on mode frequencies obtained from the linearized Vlasov-Poisson equation. Excellent agreement is found in the case of the "tilting instability" in constant focusing, which confirms the equivalence of both models - on the level of second order perturbations. In periodic focusing structures the stop bands of the "sum envelope instability" are obtained and found to be in

very good agreement with PIC simulations, which completes the picture of second order coherent modes in 2-D high intensity beams.

Contents

1 Introduction

Particle accelerators have been widely used in many scientific research to understand fundamentals of the nature. Consistent development of accelerator design and technology, extended their applications from academic research to medicine and industry applications. The efficiency precision of accelerators as diagnostics tools, in turn, depends strongly on the intensity or brightness of beams.

During the research and development of accelerators, *accelerator physics*, concerned with designing, building and operating accelerators, is established. In accelerator physics, an important topic is to obtain maximum beam current (i.e., maximum beam intensity) in an accelerator. In this context, the interaction between charged particles in a beam, i.e., the *effect of space charge*, plays an essential role of the limitation of maximum beam intensity, since space charge can drive coherent beam instability and incoherent resonance: the former is characterized with the beam coherent oscillation [1], where the particles in the beams move as a whole and are characterized by a coherent frequency, while the latter is a resonance of a single particle and can be described by a single particle Hamiltonian including space-charge driven forces (see, for example, in Ref. [2]). The situation in circular accelerators is further complicated because of the *effect of dispersion*, which is usually characterized by the dispersion function to quantify the influence of the energy spread in a beam on the motion of particles in the beam. Therefore, there is a combined effect of space charge and dispersion acting on the motion of intense beams in circular accelerators. Furthermore, space charge has influence on dispersion and leads to space-charge-modified dispersion, which is a characterization of circular accelerators transporting high-intensity beams.

This thesis is mainly dedicated to a detailed study of the motion and instability of high-intensity proton or ion beams in circular accelerators, where both space charge and dispersion play an essential role. Examples of such accelerators are the SIS-18 at GSI (Gesellschaft für Schwerionenforschung) and the SIS-100 for the upcoming FAIR [3] (Facility for Antiproton and Ion Research) project. The theory of beam dynamics in previous literatures is generalized to the case including both space charge and dispersion for intense beams transported in circualr accelerators. Based on the generalized theory and detailed particle-in-cell (PIC) simulations, the mechanism of beam motion and beam stability under the combined effect of space charge and dispersion in periodically focused channels of circular accelerators is investigated in detail. In particular, a novel beam instability induced by space charge and dispersion [4] is presented. As an important application of the generalized theory, the beam behavior during bunch compression in SIS-18 is investigated, and intensity limitation during bunch compression related to coherent beam instabilities and incoherent single particle resonances are analyzed. Another focus of this thesis is to develop and present a complete set of second order space-charge driven modes. This is achieved by using a self-consistent set of equatins derived by Chernin [5]. Based on the set of space-charge driven modes, accurate information of stability properities of intense beam transported in either periodic or constant focusing structures, such as the stop bands and growth rates of beam instabilities, are obtained [6].

In this thesis, long derivations are put in the Appendix to keep the flow of the text concise and clear. SI units are used throughout the thesis. A description and the unit for each symbol can be found in the Symbol List in the Appendix.

1.1 Circular and Linear Accelerators

Accelerators can be classified into linear accelerators and circular accelerators, depending upon whether the accelerated particles go straight in a linear accelerator (*linac*) or accumulated for many turns cycling in a ring (circular accelerator). In a linac, particles pass once through the accelerating cavity, whereas in a circular accelerator, particles pass through an accelerating cavity many times.

A typical modern linac consists of sections of waveguides or high-Q resonant cavities which can excite electromagnetic fields. Particles go through these cavities, interact with the electromagnetic field and gain kinetic energy. The radio-frequency quadrupole (RFQ) and drift-tube linac (DTL) are two common types of linac. A sketch of a DTL is in Fig. 1.1. For a large accelerator complex, linacs are employed as injectors to circular accelerators for further acceleration.

The most common type of modern circular accelerators are *synchrotrons*. A typical synchrotron consists of various magnets and RF cavities. The magnets are arranged as a “lattice” to provide alternating gradient focusing and bending forces to guide particles traveling around a closed path along the ring. Dipole magnets (or dipoles for short) are used for guiding particles along the curved path along the ring. Quadrupoles are used for particle focusing based on the alternating-gradient principle [1]. Injection and extraction magnets (septum magnets) are used for particle injection from a linac (or transport beam line) and particle extraction for further acceleration or for experiments. RF cavities provide accelerating electromagnetic field to the particles, with its frequency being synchronized with the one of particles [2]. The layout of a synchrotron is schematically shown in Fig. 1.2.

---

[1] Also known as “the principle of strong focusing”, is the principle that the net effect on a charged particle beam passing through alternating electromagnetic field gradients is to make the beam converge, see [7].

[2] According to the principle of phase stability, with an appropriate choice of phase advance of RF cavity, particles will gain or lose kinetic energy per passage through RF cavities and the whole beam remains stable, see [8, 9].

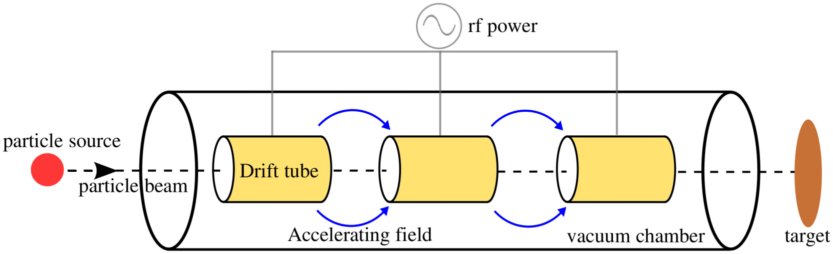

Figure 1.1.: Schematic drawing of a drift-tube linac (DTL). Particles feel electric field at each gaps between two adjacent tubes to increase kinetic energy, and feel zero field when traveling inside the tubes.

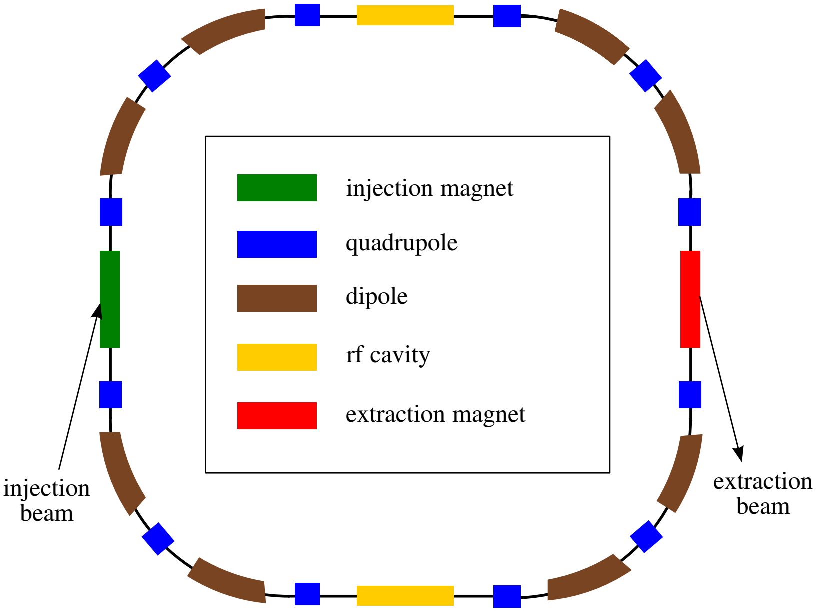

Figure 1.2.: Schematic drawing of a synchrotron. When particles travel along the ring through each element: dipoles guide the trajectory of particles along the ring; quadrupoles provide transverse focusing force; injection and extraction magnets (septum magnets) are used to beam injection and beam extraction; RF cavities provide the electric field for acceleration.

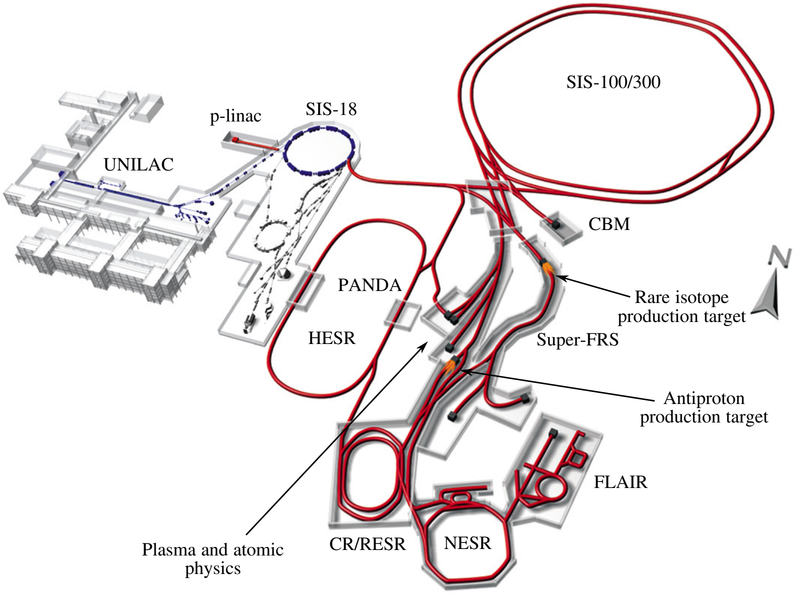

Figure 1.3.: Layout of the FAIR project. Ion beams generated at ion source (at the start point of UNILAC) are accelerated via UNILAC to 11.4 MeV/u, and injected to booster synchrotron SIS-18, where the typical kinetic energy of particles are at the range of 200 MeV/u to 4 GeV/u. Those particles are transported to SIS-100 for further acceleration, where the final kinetic energy of particles can reach up to 28 GeV/u (for protons). Particles can be extracted from SIS-100 for various experiments.(figure from [3])

1.2 FAIR Project at GSI

The GSI Helmholtzzentrum für Schwerionenforschung (Helmholtz center for heavy ion research) [10] is a worldwide unique large-scale accelerator facility for fundamental research with ion beams. It was set-up in 1969 and is jointly funded by the Federal Republic of Germany and the state of Hessen. As an international state-of-the-art, multipurpose accelerator complex in Europe, FAIR is currently under construction at GSI in cooperation of an international community of countries and scientists. FAIR will consist of ion synchrotron; the upgraded SIS-18, the SIS-100 and several storage rings as well as beam targets. The layout of the accelerator and experiment of FAIR are shown in Fig. 1.3.

1.3 Space Charge and Dispersion

Space charge and dispersion are two basic phenomena that affect high-intensity beam dynamics in circular accelerators. In accelerator physics, *space charge* refers to the electric field created by the Coulomb forces between the charged particles of a beam, partly cancelled by the magnetic field generated from the moving beam. For a beam with an arbitrary charged particle distribution, the joint forces from electric and magnetic fields (space-charge forces) is likely to be nonlinear. In 1959, Kapchinsky and Vladimirsky gave an ellipsoid beam distribution that generates a perfect linear space-charge force in the beam [11]. In this distribution, particles are random-uniformly distributed on both phase space and real space. This distribution (usually called K-V distribution in the literature) allows one to study space charge effects in a *self-consistent* manner because the distribution remains uniform during beam transporting. In most practical beams, however, the particle distribution is Gaussian-like, which generates nonlinear space-charge forces. In order to analyze a realistic particle distribution, Lapostolle and Sacherer in 1971 introduced the concept of *equivalent beams* [12, 13] and the *rms envelope equations*, which describe self-consistently the motion of non-K-V beams with space charge in a rms sense. Based on the rms envelope approach, improvements have been made on the understanding of the space charge dynamics in the past few decades: the particle core resonance; beam halo formation [14, 15]; the envelope oscillation and its instability [16, 17, 18, 19, 20, 21, 22]; high order beam collective modes and their instabilities [1, 23, 24]; and the space charge structural resonance [25, 26]. Recently with the successful experimental observations of fourfold structure and coupling emittance in high-intensity linear accelerators [27, 28], space-charge-driven particle resonance and beam instability have received renewed interest, since it represents a major intensity limitation not only in linacs, but also in circular machines.

Dispersion in accelerator physics is analogue to the optical dispersion, where a particle of higher momentum (or energy) is deflected through a lesser angle in a bending magnet. For a practical beam with momentum spread (or energy spread), the transverse beam size will enlarge as it passes through a bending magnet. The dispersion effect can be described quantitatively by the *dispersion function*, which is one of the most essential characteristics of a circular accelerator.

In recent years, with increasing demand of transporting high-intensity beams in circular accelerators, progress has been made on the study of the influences of space charge and dispersion on beam dynamics in circular accelerators. In 1998, Marco Venturini and Martin Reiser developed an envelope equation system with an generalized invariant emittance in the presence of both dispersion and space charge [29, 30]. In the same year, S. Y. Lee and H. Okamoto gave a Hamiltonian expression with a modified dispersion formula including higher order space charge potential terms [2]. Other methods involve a smooth approximation approach [31] or a modified particle-core model [32, 33, 34].

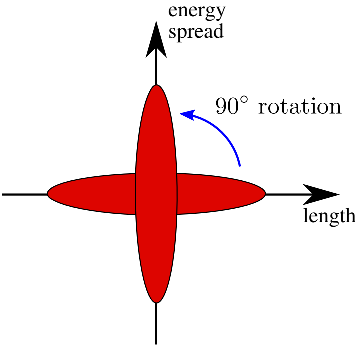

Figure 1.4.: Bunch compression by fast bunch rotation. The bunch in the horizontal position is rotated by 90° into an upright position.

1.4 Bunch Compression in Synchrotrons

In many accelerator-based facilities, short and intense ion or proton bunched beams (*bunches* for short) are required for various applications, such as the production and subsequent storage of exotic nuclei or antiprotons, generation of dense plasmas and spallation neutron sources. For instance, in both of the synchrotrons SIS-18 and SIS-100 at FAIR, short bunches are planned to be achieved via bunch compression process before extraction. During bunch compression, as the bunch is compressed, the beam current is increasing. The resulting space charge effect is enhanced and represents an important limitation for the maximum compression ratio as it leads to particle resonance and beam instability. Therefore, bunch compression must be completed as fast as possible in order to minimize the dwelling time of bunches in the extreme space charge regime.

A widely-accepted scheme to achieve bunch compression is a 90° non-adiabatic fast bunch rotation in longitudinal phase space due to a ramped high RF voltage. For instance, such a fast bunch rotation process is performed before extraction in the SIS-18 [35, 36], and proposed for the FAIR SIS-100 [37]. Fig. 1.4 shows a sketch of the fast bunch rotation. The bunch is rotated via 90° in the longitudinal phase space, decreasing the bunch length, at the cost of the energy spread increasing. The enlarged energy spread in the bunch is in inverse proportion to the reduced bunch length due to the invariant longitudinal emittance [3], and results in an enhanced effect of dispersion. In the past few years, the scheme of bunch compression based on fast rotation has been the subject of numerous theoretical studies investigating beam instability limits and beam quality evolution [38, 39, 40, 41, 42, 43, 44, 45, 46, 47].

---

[3] The "longitudinal emittance" refers to the area of the ellipse in Fig. 1.4. For more details see Chapter 2 and Chapter 7.

1.5 Motivation

The main goal of this thesis is dedicated to a detailed study of the beam instabilities driven by space charge in synchrotrons, in which the role of the combined effect of space charge and dispersion is fully taken into account in the beam dynamics, by using a numerical beam envelope approach inclduing dispersion and PIC simulations. Furthermore, a complete set of second order moment equations are developed to offer a unified framework to study the stability properties of high-intensity beams.

In order to investigate the beam intensity limitations due to space charge during bunch compression, another goal of the work addresses a study of the bunch compression in high-current sychrotrons, using a coupled longitudinal-transverse envelope equation system including dispersion, compared with the results from PIC simulations. The mechanism of competition between the beam instabiilty and particle resoancne are analyzed in detail.

1.6 Overview of the Thesis

To simplify the handling with the thesis, this subsection provides a short outline of the structure of the thesis. Chapter 2 introduces fundamentals of beam dynamics in accelerators, including single particle dynamics and space charge. It gives the theoretical background that is used in the thesis. Chapter 3 starts with a self-consistent treatment of beam dynamics with space charge, followed by the introdution of the concept of beam envelope motion, which is used throughout this thesis. Chapter 4 aims to make the reader familiar with the necessary details of the simulation model and numerical algorithms used in the thesis. Benchmarking between the two approaches are performed by several typical examples. In Chapter 5 we develop a model to calculate the complete set of second order instabilities. Chapter 6 investigates beam collective motion in the presence of space charge and dispersion in circular accelerators. The envelope approach introduced in Chapter 3 are generalized to the case including dispersion. With perturbation on the generalized envelope equations, the mechanism of beam stability is analyzed. The beam instability induced by the combined effect of space charge and dispersion is identified, characterized with a *dispersion mode*. Chapter 7 deals with the bunch compression in SIS-18 synchrotron at GSI. The generalized envelope equations are coupled with the longitudinal envelope equation to give a full description of bunch compression. The numerical solutions of the generalized equations are compared with PIC simulation results. The mechanism of the onset of beam instabilities and particle resonances which place threshold on the beam current are analyzed and explained. The thesis concludes with the summary of results and an outlook in Chapter 8.

2 Single Particle Dynamics

Beam dynamics is main theoretical essence of accelerator physics. The framework of beam dynamics evolves from the concepts of classical mechanics, electrodynamics, statistical physics and plasma physics. It aims to describe the behavior of a charged-particle beam traveling in an accelerator and used in accelerator design, operation, and optimization. In this chapter, we introduce the fundamentals of beam dynamics - the dynamcis of single particle - to the extent needed as a basis for the following chapters. In the framework of single particle dynamcis, we focus on the motion of individual particles. The collective motion of a beam will be discussed in the next chapter.

Section 2.1 starts with the Hamiltonian of a charged particle in electromagnetic field, to arrive at the equations of transverse motion. Main essential physical quantities, such as lattice functions, betatron tune, and transverse emittance are briefly presented. Section 2.2 introduces the concept of dispersion and the dispersion function, which will be further discussed in the following chapters. Section 2.3 focuses on longitudinal particle dynamics. The equaitons of longitudinal motion is derived governed by a longitudinal Hamiltonian. Section 2.4 discusses the basic theory of space charge, including both of the transverse and longitudinal components.

2.1 Transverse Particle Dynamics

2.1.1 Equations of Motion

A charged particle in electromagnetic field is governed by the Lorentz force [48]

$$\vec{F} = \frac{d\vec{p}}{dt} = q(\vec{E} + \vec{v} \times \vec{B}), \tag{2.1}$$

where q is the charge of the particle, $\vec{v}$ is the velocity of the particle, $\vec{p} = \gamma m \vec{v}$ is the particle momentum, with $\gamma = (1 - v^2/c^2)^{-\frac{1}{2}}$ the relativistic factor, c the speed of light, and $\vec{E}$ and $\vec{B}$ are respectively the electric field and magnetic field. The $\vec{E}$ and $\vec{B}$ fields follow the Maxwell equations [48]

$$\begin{aligned} \vec{E} &= -\nabla\Phi - \frac{\partial \vec{A}}{\partial t}, \\ \vec{B} &= \nabla \times \vec{A}, \end{aligned} \tag{2.2}$$

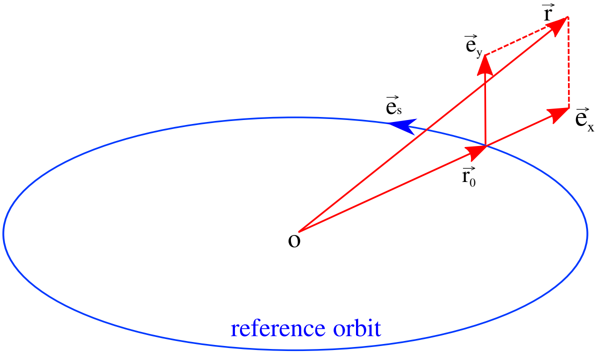

Figure 2.1.: Curvilinear coordinate system for particle motion in circular accelerators.

where, Φ and $\vec{A}$ are the scalar potential and vector potential, respectively. The Lorentz force in Eq. 2.1 can be derived from the Hamiltonian for particle motion (see, for example, in [49])

$$H_1 = c[m^2c^2 + (\vec{P} - q\vec{A})^2]^{\frac{1}{2}} + q\Phi, \tag{2.3}$$

in which $\vec{P} = \vec{p} + q\vec{A}$ is the canonical momentum.

In beam dynamics, it is convenient to adopt a curvilinear coordinate system for particle motion. As shown in Fig. 2.1, $\vec{r}$ denotes the reference orbit, and $\vec{e}_x$, $\vec{e}_y$, and $\vec{e}_s$ form the basis of the curvilinear coordinate system, in which $\vec{e}_x$ and $\vec{e}_y$ form the *transverse* plane, and $\vec{e}_s$ represents the *longitudinal* direction. Any particle's trajectory around the reference orbit can be expressed as $\vec{r}(s) = \vec{r}_0(s) + x\vec{e}_x + y\vec{e}_y$, with (x, y, s), the particle coordinates in the curvilinear system.

After establishing the curvilinear coordinate system, two steps of derivations are needed to obtain the equations of particle transverse motion in this coordinate system. At first, a Hamiltonian of particle motion H_2, in term of (x, y, s), with the corresponding conjugate coordinates (p_x, p_y, p_s) can be found by performing a canonical transformation from the Hamiltonian H_1 in Eq. 2.3

$$H_2 = q\Phi + c[m^2c^2 + \frac{(p_s - qA_s)^2}{(1 + x/\varrho)^2} + (p_x - qA_x)^2 + (p_y - qA_y)^2], \tag{2.4}$$

in which, ϱ is the radius of curvature of the curvilinear system, and the subscripts x, y, and s represent respectively the components in $\vec{e}_x$, $\vec{e}_y$ and $\vec{e}_s$ directions in the curvilinear coordinate system. Secondly, since in accelerators the scalar and vector potential Φ and

$\vec{A}$ are constant[1], the longitudinal momentum p_s can be chosen as a new Hamiltonian, which can be written as [50]

$$H_3 = -p(1+\frac{x}{\varrho}) + \frac{1+x/\varrho}{2p}[(p_x - qA_x)^2 + (p_y - qA_y)^2] - qA_s. \tag{2.5}$$

Here, we use the approximation that the transverse momenta p_x and p_y are much smaller than p_s.

The transverse equations of motion of a charged particle in the curvilinear coordinate system can be derived from the expression of the Hamiltonian H_3

$$\begin{aligned} \frac{d^2x}{ds^2} - \frac{\varrho + x}{\varrho^2} &= \pm \frac{B_y}{B\varrho}\frac{p_0}{p}(1+\frac{x}{\varrho})^2, \\ \frac{d^2y}{ds^2} &= \mp \frac{B_x}{B\varrho}\frac{p_0}{p}(1+\frac{x}{\varrho})^2, \end{aligned} \tag{2.6}$$

in which, p and p_0 are the momenta of the particle and the *reference particle*, respectively. $B_x = -\frac{\partial A_s}{\partial y}$ and $B_y = \frac{\partial A_s}{\partial x}$ are the transverse components of the magnetic fields. $B\varrho = p_0/q$ is the magnetic rigidity, defining the energy of the reference particle. A reference particle is chosen in such a way that it travels ideally through the center of the magnets (quadrupoles, dipoles and so on) with its coordinate $(x = 0, y = 0)$ along the reference orbit of the ring. After one complete turn the reference particle will remain on its trajectory and return its initial position. The one periodicity-turn trajectory of the reference particle is defined as a *closed orbit*. Eqs. 2.6 describes the motion of the particles with their coordinates $(x \neq 0, y \neq 0)$ moving around the closed orbit, which is called transverse *betatron motion*. We solve Eqs. 2.6 without energy spread (i.e., $p = p_0$) in this section. The case with energy spread (i.e., $p \neq p_0$), which brings the dispersion effect, will be discussed in next section.

Since the transverse amplitude of betatron motion (x, y) is small, we can linearize Eqs. 2.6 and obtain the Hill equations [51]

$$\begin{aligned} \frac{d^2x}{ds^2} + \kappa_{0,x}(s)x = 0, \\ \frac{d^2y}{ds^2} + \kappa_{0,y}(s)y = 0, \end{aligned} \tag{2.7}$$

where $\kappa_{0,y} = 1/\varrho^2 - B_1(s)/B\varrho$, $\kappa_{0,y} = B_1(s)/B\varrho$ are the effective focusing functions, and $B_1 = \frac{\partial B_y}{\partial x} = -\frac{\partial B_x}{\partial y}$ the quadrupole gradient function evaluated at the closed orbit. Because of the periodic property of synchrotrons, $\kappa_{0,x}$ and $\kappa_{0,y}$ are periodic functions of s, $\kappa_{0y,0x}(s) = \kappa_{0x,0y}(s + L)$ with the periodic length L. Most synchrotrons have separated

---

[1] For most elements in accelerators except the RF cavity, we have $\varphi = 0$. The non-zero electric potential φ plays a key role in the longitudinal motion of particles; magnetic elements in accelerators usually have transverse magnetic fields with $A_x = A_y = 0$

dipoles and quadrupoles for guiding/bending and alternating focusing particles, respectively. In a quadrupole where $1/\varrho \to 0$, we have $\kappa_{0,x} = -\kappa_{0,y} = B_1(s)/B\varrho$, indicating particles focus in one direction (for example in x-direction) and defocus in another direction (for example in y-direction). In a dipole, which usually lies on the xs-plane, we have $\kappa_{0,x} = 1/\varrho$ and $\kappa_{0,y} = 0$. In addition to guiding the direction of particles, dipoles also have weak focusing effects since $1/\varrho > 0$.

2.1.2 Twiss Parameters

Now let us consider the solution of the Hill equations in Eqs. 2.7. With the periodic condition, the Hill equations in Eqs. 2.7 are second order homogeneous differential equations with periodic varying coefficients, and can be solved using Floquet theorem [52]. For simplicity, we use the notation z to denote either x or y in transverse plane. The Hill equations in Eqs. 2.7 can be rewritten as[2]

$$\frac{d^2z}{ds^2} + \kappa_{0,z}(s)z = 0. \tag{2.8}$$

After some standard derivations and transformations in textbooks (see, e.g., Ref. [50]), the solution of Eq. 2.8 is

$$\begin{aligned} z &= \sqrt{\epsilon_z \beta_{0,z}(s)}\cos[k_{0,z}(s) + \varphi_0], \\ z' = \frac{dz}{ds} &= -\sqrt{\frac{\epsilon_z}{\beta_{0,z}(s)}}\left\{\alpha_{0,z}(s)\cos[k_{0,z}(s) + \varphi_0] + \sin[k_{0,z}(s) + \varphi_0]\right\}. \end{aligned} \tag{2.9}$$

Here, $\beta_{0,z}(s)$ is the betatron amplitude function, or *beta function*. The motion that a particle performs described in Eqs. 2.9 is called *betatron motion*. $\alpha_{0,z}(s)$ is the negative slope of $\beta_{0,z}(s)$ with $\alpha_{0,z}(s) = -\beta'_{0,z}(s)/2$. The functions $\beta_{0,z}(s)$, $\alpha_{0,z}(s)$, along with another quantity defined by $\gamma_{0,z} = (1+\alpha^2_{0,z})/\beta_{0,z}$ are called the Courant-Snyder parameters, or *Twiss parameters*, which characterize the fundamental properties of the sequences of the magnets (lattice) in accelerators. The quantity ϵ_z is the single particle *emittance*, which is a constant of integration and will be discussed in detail in the next subsection. φ_0 in Eqs. 2.9 is the initial phase advance and usually chosen as zero for simplicity. $k_{0,z}(s)$ is the betatron phase advance (or phase advance for short) in the z-dirction that a particle achieves after performing beatron motion on a length of s, and can be calculated by integrating the beta function over the length

$$k_{0,z}(s) = \int_0^s \frac{d\tilde{s}}{\beta_{0,z}(\tilde{s})}. \tag{2.10}$$

---

[2] Here, we use the subscript '0' in the κ and the quantities in the following to denote the quantities for accelerators, which are independent of the beam.

Consider a circular accelerator with its circumference of $C = nL$, where n is the number of periodic structures of the accelerator and L is the length of one period. After one revolution, the betatron phase advance (in the z-direction) that a particle achieves is

$$k_C = \int_0^{nL} \frac{ds}{\beta_{0,z}(s)}, \tag{2.11}$$

The number of betatron oscillations per revolution, also known as the betatron *tune* along the z-direction defined as

$$Q_{0,z} = \frac{k_C}{2\pi} = \frac{1}{2\pi}\int_0^{nL} \frac{d\tilde{s}}{\beta_{0,z}(\tilde{s})}. \tag{2.12}$$

In a beam, individual particles in betatron oscillation have individual tunes. The tune of a reference particle, is called a working point, and is important for accelerator design and operation since the particle resonance is usually related to the choices of tunes. For example, for a circular accelerator with an integer $Q_{0,z}$, particles return to each location in the accelerator with the same betatron phase, since the betatron phase advnace per passage is an integer multiple of 2π. We assume a small imperfection of dipole magnets exists at the position of s_0, particles experience a slight change of its coordinate due to the magnetic error at s_0 per passage. Upon subsequent passes, the change accumulates in phase and resulting in resonance, leading to the amplitude growth and particle loss[3].

With the Twiss parameters and phase advance in Eq. 2.9 and Eq. 2.10, the transverse betatron motion of Eq. 2.8 can be described in matrix form as

$$\mathbf{M}(s_2|s_1) = \mathbf{B}(s_2)\begin{pmatrix} \cos k_{0,z} & \sin k_{0,z} \\ -\sin k_{0,z} & \cos k_{0,z} \end{pmatrix}\mathbf{B}^{-1}(s_1), \tag{2.13}$$

with

$$\mathbf{B(s)} = \begin{pmatrix} \sqrt{\beta_{0,z}(s)} & 0 \\ -\frac{\alpha_{0,z}(s)}{\sqrt{\beta_{0,z}(s)}} & \frac{1}{\sqrt{\beta_{0,z}(s)}} \end{pmatrix}. \tag{2.14}$$

The matrix $\mathbf{M}(s_2|s_1)$ is called the transfer matrix and characterizes particle betatron motion from s_1 to s_2 by

$$\mathbf{z}(s_2) = \mathbf{M}(s_2|s_1)\mathbf{z}(s_1), \tag{2.15}$$

where $\mathbf{z} = (z,\ z')^T$ is the vector of transverse particle coordinates. Eq. 2.15 is widely used for solving the equation of betatron motion, as well as for particle tracking in simulations.

---

[3] Besides driven by the external magnetic imperfections of accelerator elements described here, particle resonance can also be driven by the electromagnetic field (space charge) of the beam itself, which will be discussed in Chapter 3.

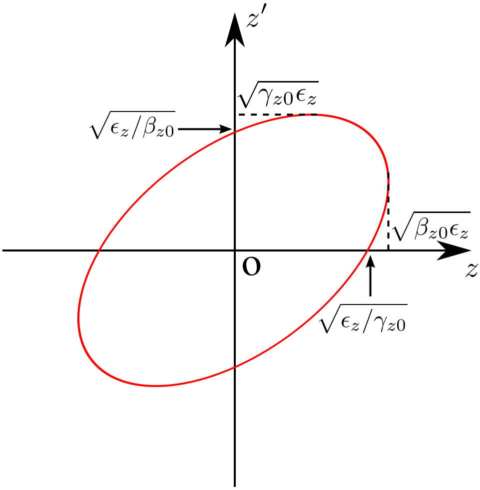

Figure 2.2.: Single particle emittance in z-direction: the invariant of a particle betatron motion in (z, z') phase space. The elliptical area enclosed is equal to $\pi\epsilon_z$. The maximum amplitude of betatron motion is $\sqrt{\beta_{0,z}\epsilon_z}$ and the maximum divergence angle is $\sqrt{\gamma_{0,z}\epsilon_z}$.

2.1.3 Emittance

Another essential quantity in beam dynamics is the emittance, as introduced in Eqs. 2.9. To show the physical meaning of the emittance, we combine the two equations in Eq. 2.9 and obtain

$$\epsilon_z = \gamma_{0,z}^2 z^2 + 2\alpha_{0,z} z z' + \beta_{0,z} z'^2, \tag{2.16}$$

which defines an ellipse in the *phase space* (z, z'), characterizing the trajectory of the betatron motion of a particle after traveling one periodic structure, as shown in Fig 2.2. The emittance of a single particle is determined by the initial coordinate of the particle, and independent of the external focusing strengths. Particles with different initial coordinates (z_0, z_0') have different emittances; however the emittance of each particle is an invariant as it is transported in an accelerator.

While the emittance defined in Eq. 2.16 characterizes the motion of single particle, to characterize the whole beam, the maximum single particle emittance is defined as the emittance of the beam,

$$\hat{\epsilon}_z = \epsilon_{z,max}. \tag{2.17}$$

In the $z - z'$ phase space, different single particle emittances define a series of concentration ellipse. The beam emittance $\hat{\epsilon}_z$ defines the largest concentration ellipse. The motion of the particles is associated with an equivalent motion of the corresponding points on each concentration ellipse. In most cases in accelerators, a beam can be assumed as a system of non-interacting particles. While accelerators consist of both of linear and nonlinear elements, for beam motion, the linear elements (i.e., focusing and guiding/bending) are the dominant component. According to Liouville's theorem, which states that the volume occupied by a given number of particles in phase space remains invariant with time, the emittance of a beam is constant during transport in accelerators. In the following chapters, the invariance of the emittance will be generalized to include electromagnetic interactions between charged particles.

2.2 Dispersion Function

In this section we consider a beam with energy spread (or momentum spread). A reference particle with momentum p_0 defining a closed orbit is called a *synchronous particle*. For a particle with momentum p, the fractional momentum deviation with respect to the synchronous particle is $\delta = |p - p_0|/p_0$, which is usually small (in the order of 10^{-4} to 10^{-2}). When traveling through bending magnets in a circular accelerator, particles with different momenta feel different Lorentz forces, and go on different trajectories, as shown in Fig. 2.3. This phenomenon in accelerator physics is called *dispersion*, since it is similar to the case when light travels through a prism. The dispersion effect in accelerators can be quantified by the dispersion functions.

The derivation of a dispersion function[4] $D_{0,x}(s)$ starts with expansion of the equations of transverse motion in x in Eqs. 2.6 to the first order in x/ϱ, since $x \ll \varrho$ [50],

$$x'' + \left[\frac{1-\delta}{\varrho^2(1+\delta)} - \frac{\tilde{\kappa}_{x0}(s)}{1+\delta}\right]x = \frac{\delta}{\varrho(1+\delta)}. \tag{2.18}$$

Here $\tilde{\kappa}_{x0}(s)$ is the focusing forces of quadrupole magnets with $\tilde{\kappa}_{x0}(s) = \frac{1}{\varrho^2} - \kappa_{x0}(s)$. The solution of Eq. 2.18 is a linear superposition of a homogeneous solution and a particular solution, i.e.,

$$x(s) = x_\beta(s) + D_{0,x}(s)\delta, \tag{2.19}$$

where $x_\beta(s)$ and $D_{0,x}(s)$ satisfies

$$\begin{aligned} x_\beta'' + [\kappa_{x0}(s) + \Delta\kappa_{x0}(s)]x_\beta &= 0, \\ D_{0,x}''(s) + [\kappa_{x0}(s) + \Delta\kappa_{x0}(s)]D_{0,x}(s) &= \frac{1}{\varrho(s)}. \end{aligned} \tag{2.20}$$

---

[4] The subscript '0' in $D_{0,x}$ denotes the case without space charge. In Chapter 6, the dispersion with space charge is written as 'D_x'.

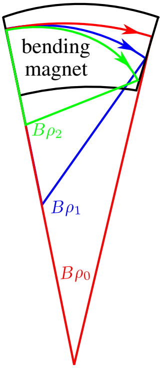

Figure 2.3.: Schematic drawing of particle trajectories with different momenta in bending magnets. Due to different moment p_i, the magnetic rigidity $B\varrho_i = p_i/q(i = 1, 2, 3)$ of each particle is different, defining different trajectories.

With the chromatic perturbation[5]

$$\Delta\kappa_{x0}(s) = [-\frac{2}{\varrho^2} + \kappa_{x0}(s)]\delta. \tag{2.21}$$

Here, we neglect high order terms of δ. If we further neglect $\Delta\kappa_{x0}(s)$, which is usually small, the second inhomogeneous equation in Eqs. 2.20 becomes,

$$D''_{0,x}(s) + \kappa_{x0}(s)D_{0,x}(s) = \frac{1}{\varrho(s)}, \tag{2.22}$$

which is called dispersion equation, and its solution $D_{0,x}(s)$ is called *dispersion function*. Since $\kappa_{x0}(s)$ and $\varrho(s)$ are periodic, the dispersion function and its derivative obey the periodic condition

$$D_{0,x}(s) = D(s + L), \quad D'_{0,x}(s) = D'_{0,x}(s + L), \tag{2.23}$$

where L is the length of one periodic structure. In the presence of dispersion, the transverse motion of a particle has two contributions: the betatron motion described by x_β, and the dispersion function described by $D_{0,x}(s)\delta$.

---

[5] In accelerator physics, the dependence of the focusing strength on the momentum of a particle is called “chromatic aberration”, which is beyond the scope of the thesis.

The solution of Eqs. 2.20 can be written in matrix form as

$$\begin{pmatrix} D(s_2) \\ D'(s_2) \\ 1 \end{pmatrix} = \begin{pmatrix} \mathbf{M}(s_2|s_1) & \bar{d} \\ 0 & 1 \end{pmatrix} \begin{pmatrix} D(s_1) \\ D'(s_1) \\ 1 \end{pmatrix}, \tag{2.24}$$

with particular solution

$$\bar{d} = \begin{cases} \begin{pmatrix} \frac{1}{\varrho \kappa_{x0}}(1 - \cos\sqrt{\kappa_{x0}} s) \\ \frac{1}{\varrho\sqrt{\kappa_{x0}}} \sin\sqrt{\kappa_{x0}} s \end{pmatrix} & \text{if } \kappa_{x0} \geq 0, \\ \\ \begin{pmatrix} \frac{1}{\varrho |\kappa_{x0}|}(\cosh\sqrt{|\kappa_{x0}|} s - 1) \\ \frac{1}{\varrho\sqrt{|\kappa_{x0}|}} \sinh\sqrt{|\kappa_{x0}|} s \end{pmatrix} & \text{if } \kappa_{x0} < 0. \end{cases} \tag{2.25}$$

Here, $\mathbf{M}(s_2|s_1)$ is the 2×2 transfer matrix introduced in Eq. 2.13, ϱ is the dipole bending radius, and κ_{x0} is the effective focusing force of quadrupole magnets (usually piecewise constant). With the initial condition $D(s_1)$ and $D'(s_1)$ at the initial position $s = s_1$, the dispersion function $D(s_2)$ and its derivative $D'(s_2)$ at $s = s_2$ can be obtained from Eq. 2.24. Moreover, with the periodic condition of Eqs. 2.23 imposed on Eq. 2.24, the dispersion function in a periodic structure can be calculated without any initial particle coordinates.

Conceptually, dispersion is to quantitatively characterize the coupling effect of the longitudinal beam energy spread and the transverse betatron motion. Dispersion functions, along with Twiss parameters, provide the quantitative basis for describing accelerator properties, and are essential for accelerator design and operation. Fig. 2.4 shows an example of dispersion functions and beta functions in one periodic structure in the synchrotron SIS-18 at GSI.

In the presence of dispersion, particles with different momenta travel on different closed orbits. To evaluate the total length difference of the closed orbit between particles, the concept of *momentum compaction factor* is introduced, as

$$\alpha_c = \frac{1}{C} \oint \frac{D(s)}{\varrho} ds, \tag{2.26}$$

in which C is the circumference. The *phase-slip factor* can be defined as $\eta = \alpha_c - \frac{1}{\gamma^2}$, connecting the revolution period with the momentum offset by

$$\frac{\Delta\omega}{\omega_0} = -\eta \frac{\Delta T}{T_0}. \tag{2.27}$$

Eq. 2.27 indicates that the shift of revolution frequency affects the longitudinal motion of particles, which will be discussed in the next subsection.

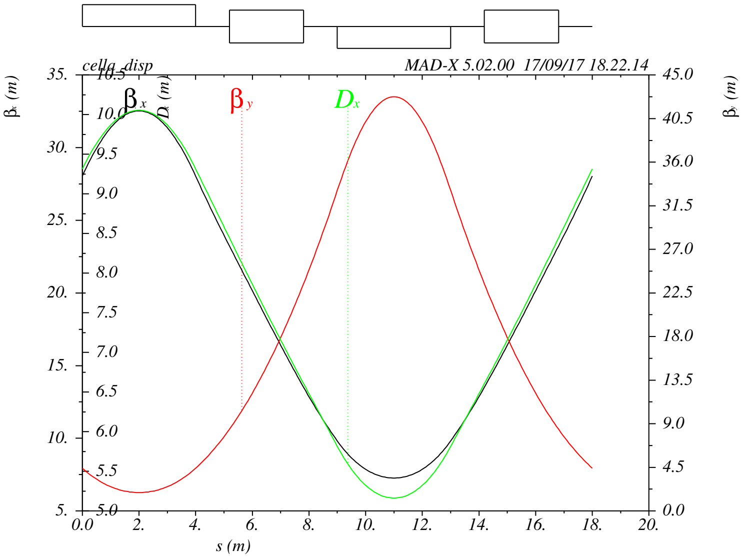

Figure 2.4.: Dispersion functions (in green color) and beta functions (β_x in black and β_y in red) calculated from MAD-X [53] in one periodic structure in SIS-18.

2.3 Longitudinal Particle Dynamics

2.3.1 Equations of Motion

In the longitudinal direction, RF cavities provide RF voltage for accelerating and focusing particles. The discovery of phase stability [8, 9] paves the way for the design of modern circular accelerators, i.e., synchrotrons. The longitudinal motion of particles is called synchrotron motion, and a particle which synchronizes with RF phase $\varphi = \varphi_s$ with revolution frequency ω_0 and momentum p_0 is called a synchronous particle. The energy that a synchronous particle and an asynchronous particle marked as i^{th} (or called off-momentum particle, with $p_i \neq p_0$) obtains per passage through the RF cavity is $\Delta E_0 = qV \sin\varphi_s$ and $\Delta E_i = qV \sin\varphi_i$, respectively, since most typical longitudinal electric fields generated in RF cavities in synchrotrons are sinusoidal. The equations of synchrotron motion of the i^{th} particle can be written as

$$\begin{aligned} \frac{d\delta_i}{dt} &= \frac{\omega_0 qV}{2\pi\beta^2 E}(\sin\varphi_i - \sin\varphi_s), \\ \frac{d\varphi_i}{dt} &= h\omega_0\eta\delta_i, \end{aligned} \tag{2.28}$$

in which $\delta_i = (p_i - p_0)/p_0$ is the fractional momentum deviation, V is the RF voltage, h is the harmonic number of the RF system, φ_i and φ_s are respectively the phase of the i^{th} particle and the synchronous particle with respect to the RF wave[6], ω_0, β and E are the angular velocity, linear velocity and the total energy of the synchronous particle, respectively. The first equation in Eqs. 2.28 is the equation of motion for the "energy difference" and the second one in Eqs. 2.28 is the phase equation. Eqs. 2.28 indicate that an asynchronous particle oscillates around the synchronous particle.

Equations 2.28 can be derived mathematically from a longitudinal Hamiltonian of the i^{th} particle, with (δ, φ) as the phase space coordinates

$$H_L = \frac{1}{2} h\omega_0 \eta \delta_i^2 + \frac{\omega_0 q V}{2\pi\beta^2 E}[\cos\varphi_i - \cos\varphi_s + (\varphi_i - \varphi_s)\sin\varphi_s], \tag{2.29}$$

in which the first term is "kinetic energy" and the second term is "potential energy". The *synchrotron frequency* for small amplitude synchrotron oscillation can be obtained from the Hamiltonian linearizion[7],

$$\omega_s = \frac{c}{R}\sqrt{\frac{hqV|\eta\cos\varphi_s|}{2\pi E}}, \tag{2.30}$$

where c is the speed of light and R the average radius of the synchrotron. The *synchrotron tune*, defined as the number of synchrotron oscillations per revolution, can be obtained from Eq. 2.30

$$Q_s = \frac{\omega_s}{\omega_0} = \sqrt{\frac{hqV|\eta\cos\varphi_s|}{2\pi\beta^2 E}}. \tag{2.31}$$

For ion or proton accelerators, typically the longitudinal beam length is much longer than transverse beam size, and Q_s is of the order of 10^{-3}, which is much smaller than the transverse betatron tune.

2.3.2 Bucket and Longitudinal Emittance

The nonlinear Hamiltonian in Eq. 2.29 defines the particle trajectories in the longitudinal phase space. The synchronous particle is located at the stable fixed point $(\varphi_s, 0)$, and performs no synchrotron oscillation. The trajectories of off-momentum particles perform synchrotron oscillations around the stable fixed point. For small amplitudes,

---

[6] In many literatures, φ_s is named as synchronous phase.

[7] For small amplitude, the linearized Hamiltonian is $\tilde{H}_L = \frac{1}{2} h\omega_0 \eta \delta_i^2 - \frac{\omega_0 q V \cos\varphi_s}{4\pi\beta^2 E}\varphi_i^2$.

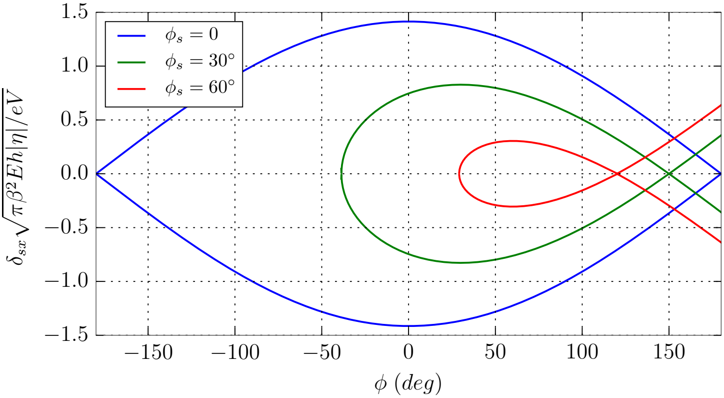

Figure 2.5.: The separatrix with $\varphi_s = 0°, 30°, 60°$. The separatrix area decreases with φ_s increases.

the trajectories become ellipses[8]. The largest trajectory can be found by the unstable fixed point $(\varphi = \pi - \varphi_s, \delta = 0)$

$$H_{sx} = \frac{\omega_0 qV}{2\pi\beta^2 E}[-2\cos\varphi_s + (\pi - 2\varphi_s)\sin\varphi_s], \tag{2.32}$$

which is called *separatrix*. The enclosed area of the separatrix is called the *bucket*. The bucket with $\varphi_s = 0$ has the largest area, as shown in Fig. 2.5 in blue curve. With a given RF voltage, the bucket area will shrink as φ_s increases. With a given φ_s, the bucket height is inversely proportional to the RF voltage.

Similar to the case in transverse phase space, the enclosed area of the particle trajectory in longitudinal phase space is called longitudinal emittance. With the small amplitude approximation, the longitudinal emittance can be written as the area of the ellipse $\epsilon_L = \pi\delta\varphi$, which is constant in the absence of acceleration.

2.4 Basic Theory of Space Charge

The framework of single particle dynamics that have been discussed so far are the investigation of the motion of an individual particle under the external electromagnetic field of various components (e.g., magnets and RF cavities) in accelerators. This picture holds well for particles in a beam with low intensity. For high-intensity beams, it no longer applies, since the interaction between charged particles, or the interaction between the beam and the its surroundings (for example, the beam vacuum pipe,

---

[8] This can be shown by the linearized Hamiltonian $\tilde{H}_L$.

beam diagnostics and so on) has to be taken into account. The former interaction is called direct space charge or *space charge*, and the later is called the indirect space charge or *impedance*. In fact, coulomb forces exist between charged particles, increasing from zero at beam center towards the edge, and push particles away from beam center. Meanwhile, as charged particles move along the path in an accelerator as a beam current, a magnetic field is generated between particles, which partially cancels the electrostatic defocusing effect of Coulomb forces. The combined effect of electrostatic defocusing and magnetic focusing, which is still repulsive, is the effect of space charge or *self fields* inside the beam [54]. On the other hand, the beam interacts electromagnetically with its surroundings, and can be treated as an *impedance* [55], which is beyond the scope of this thesis. Space charge is the most basic collective effect of charged particle beams. In principle, the treatment of space charge is a three-dimensional (3-D) problem. However, for most synchrotrons with proton or ion beams, the length of beam is usually much longer than the transverse width and the space charge coupling between transverse and longitduain direction can be neglected, thus the space charge can be decomposed into transverse and longitudinal components.

This section focuses on the fundamentals of space charge. In the following of this section, we will firsty introduce the transverse space charge, and secondly discuss briefly the longitudinal space charge.

2.4.1 Transverse Space Charge

Following the standard description of transverse space charge (see, for example, in Ref. [56]), we first consider the space charge in the case of an unbunched beam, or *coasting beam* with a round cross-section and uniform charge density traveling in a perfectly conducting round beam pipe with a constant longitudinal velocity. We assume that the radius of the beam pipe is much larger than the radius of the beam, so that the image charge phenomenon can be neglected. Such a coasting beam can be modeled as a “beam cylinder” with infinite length, as shown in Fig. 2.6.

To calculate electric and magnetic fields $\mathbf{E}$ and $\mathbf{B}$ generated by the coasting beam, we choose a small cylinder inside the beam with radius r and length l, as shown in red dashed lines in Fig. 2.6. According to Gauss’ law, in the cylindrical coordinate system we have

$$\iiint_V \nabla \cdot \mathbf{E} dV = \iiint_V \frac{\eta}{\epsilon_0} dV = \oint\!\!\!\oint_S \mathbf{E} \cdot d\mathbf{S}, \tag{2.33}$$

in which η is the uniform charge density in the unit of $[Cb/m^3]$, dV represents an unit volume inside the cylinder, and $d\mathbf{S}$ an unit of its surface. With integrals over the closed surface and the volume of the small cylinder, we obtain

$$E_r = \frac{I}{2\pi\epsilon_0\beta c}\frac{r}{a^2}. \tag{2.34}$$

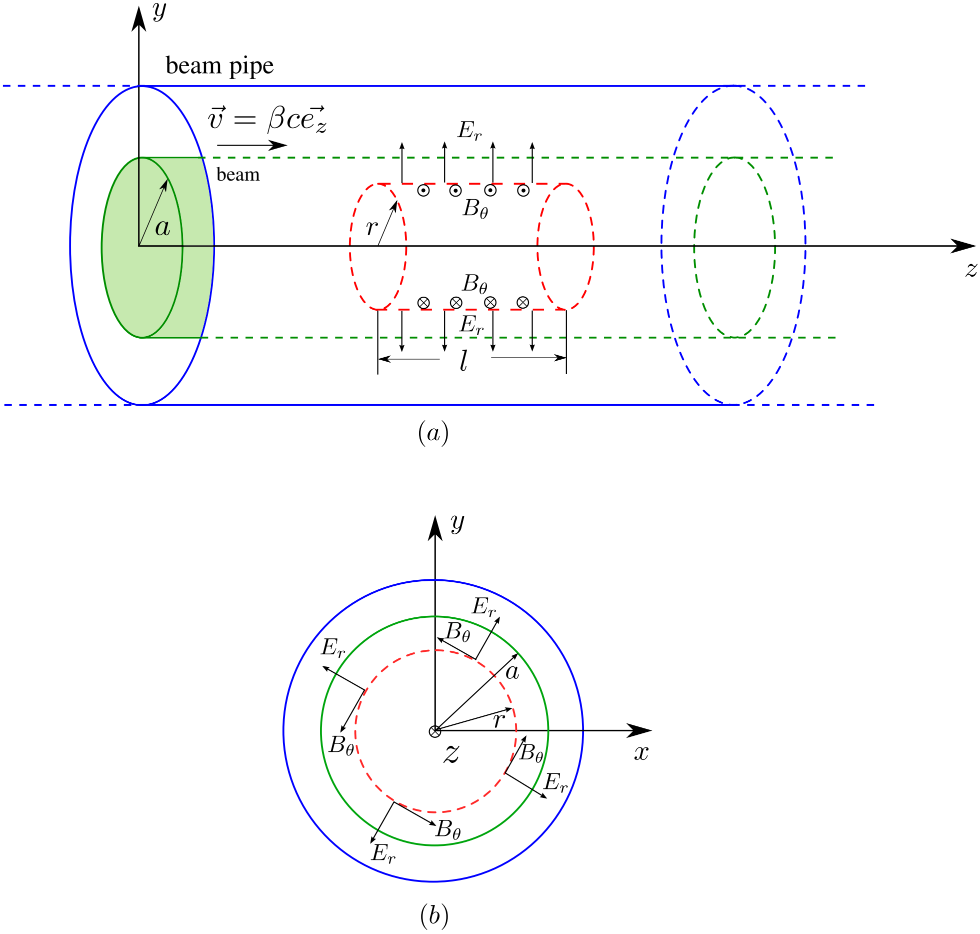

Figure 2.6.: Schematic drawing of the distribution of electromagnetic fields in the beam cylinder model. The upper plot (a) shows the electromagnetic fields on the profile of the beam cylinder; and the lower plot (b) shows the electromagnetic fields in the cross section of the beam cylinder.

Here, I is the beam current, βc the speed of beam, with c the speed of light in vacuum, ϵ_0 is the vacuum permittivity. Similarly, the magnetic field $\mathbf{B}$ can be found by Stokes' law,

$$\iint \nabla \times \mathbf{B} \cdot d\mathbf{S} = \iint \mu_0 \mathbf{J} \cdot d\mathbf{S} = \oint_S \mathbf{B} ds, \tag{2.35}$$

where μ_0 is the vacuum permeability, $J = q\beta c$ is the current density with q the charge of the individual particle. With integrals over the small cylinder of radius r and length l, Eq. 2.35 yields

$$B_\vartheta = \frac{I}{2\pi\epsilon_0 c^2} \frac{r}{a^2}. \tag{2.36}$$

It can be seen that the transverse symmetry of the beam cylinder lead to the radial electric field E_r and azimuthal magnetic field B_ϑ. The Lorentz force from beam self field acting on a particle can be found from Eq. 2.34 and Eq. 2.36

$$F_r = qE_r - q\beta c B_\vartheta = \frac{qI}{2\pi\epsilon_0 \beta c \gamma^2} \frac{r}{a^2}, \tag{2.37}$$

which is linear and radial. The first part qE_r denotes the repulsive electrostatic force, which is independent with beam velocity, and the second part $-q\beta c B_\vartheta$ denotes the magnetic force, which is attractive and increasing with beam velocity. The overall effect of the two parts is repulsive but decrease with beam velocity, with a cancellation factor $1/\gamma^2$. In the limit case of a beam traveling at the speed of light c, the cancellation factor becomes zero and the two parts become equal and cancel each other. Replacing r by the transverse coordinates x, y results in the horizontal and vertical force.

In the following we derive the equation of motion for a charged particle with space charge. For simplicity, we take the x-direction (the case in y-direction can be obtained in a similar way). The space charge force in x-direction has the form:

$$F_x = \frac{qIx}{2\pi\epsilon_0 c\beta\gamma^2 a^2}. \tag{2.38}$$

Taking the arc length s in the curvilinear coordinate as the independent variable instead of time t, we have from Eq. 2.38

$$x'' = \frac{d^2x}{ds^2} = \frac{1}{\beta^2c^2}\frac{d^2x}{dt^2} = \frac{\ddot{x}}{\beta^2c^2} = \frac{1}{\beta^2c^2}\frac{F_x}{m_0\gamma} = \frac{2r_0 I}{ea^2\beta^3\gamma^3 c}x, \tag{2.39}$$

where $r_0 = q^2/(4\pi\epsilon_0 m_0 c^2)$ is the classical particle radius with m_0 the rest mass of the particle. In the presence of space charge, the Hill equation of Eq. 2.7 is modified to

$$x'' + [\kappa_{x0}(s) - \Delta\kappa_x(s)]x = 0, \tag{2.40}$$

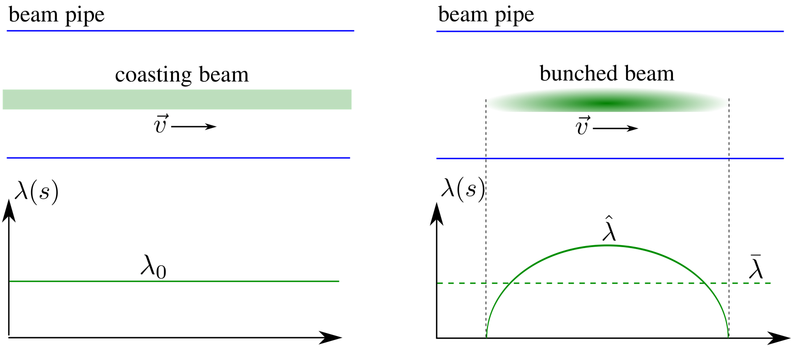

Figure 2.7.: Comparison between the particle distribution (upper plot) and the line charge density (lower plot) of a coasting beam and a bunched beam.

where $\Delta\kappa_x = 2r_0 I/(qa^2\beta^3\gamma^3 c)$ is the space charge defocusing term, indicating that the space charge forces weaken the external focusing forces. Usually, since the beam radius a varies as beam traveling in accelerators[9], the space charge force F_x and space charge defocusing term $\Delta\kappa_x$ are also functions of s.

One of the most important consequence of the space charge effect is the space-charge tune shift ΔQ_{sc}: since the space charge leads to defocusing of beams in transverse plane[10], particles in a beam will experience a space-charge-depressed tune Q_{sc} with $Q_{\mathrm{sc}} = Q_0 - \Delta Q_{\mathrm{sc}}$, in which Q_0 is the *bare* betatron tune without space charge. In other words, the frequency of transverse betatron oscillation of a particle is depressed due to the space charge effect. The space-charge tune shift (in x-direction) can be obtained by the combination of Eq. 2.12 and Eq. 2.40

$$\Delta Q_{\mathrm{sc},x} = \frac{1}{4\pi}\int_0^{2\pi R} \Delta\kappa_x(s)\beta_x(s)ds = -\frac{1}{4\pi}\frac{2r_0 I}{q\beta^3\gamma^3 c}\int_0^{2\pi R}\frac{\beta_x(s)}{a^2}ds. \tag{2.41}$$

Here, a is the transverse beam size, and $\beta_x(s)$ is the beta function. Several conclusions can be drawn from Eq. 2.41: (1). The space-charge tune shift is proportional to beam intensity; (2). For electron synchrotrons, in which $1/\gamma^3 \approx 0$, the space-charge tune shift and space charge effect can be neglected; (3). When beam intensity and energy is given, the space-charge tune shift is inversely proportional to the transverse beam size.

The theory of space charge discussed so far is for coasting beams. For the case of bunched beams, Eq. 2.34, Eq. 2.36 and Eq. 2.40 still hold, provided that the beam is

---

[9] In alternating gradient channles in accelerators, the radius of the travelling beam is a function of s because the focusing forces is function of s.

[10] The focusing forces of quadrupole magnets felt by a charged particle are partly cancelled by the defocusing forces of space charge, leading to an effective focusing strength acted on the particle.

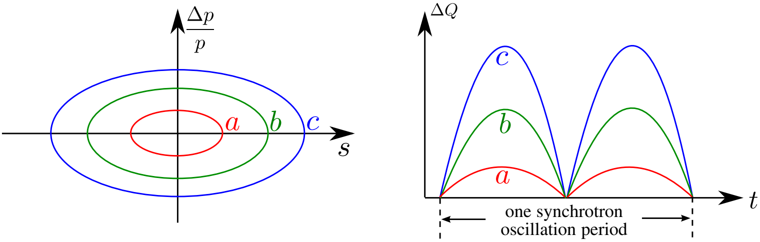

Figure 2.8.: Schematic drawing of the synchrotron motion of particles with various amplitudes in the longitudinal phase space and the corresponding space-charge tune shifts.

axisymmetric. The major difference between a coasting beam and a bunched beam is that there exists a space-charge tune spread in a bunched beam, instead of a space-charge tune shift.

In a coasting beam, the line charge density can be seen as uniform, while in a bunched beam the line charge density has a non-constant distribution with a maximum value at the beam center because of longitudinal synchrotron motion (see Fig. 2.7). In bunched beams, each particle performs synchrotron oscillations, changing its longitudinal position periodically. Fig. 2.8 shows three particles a, b, and c with increasing synchrotron amplitudes: particle a stays closest to the beam center and experiences the strongest space charge effect. Therefore, particle a has the largest space-charge tune shift and smallest tune shift variations during synchrotron oscillation. Particle c with the largest amplitude, oscillates within a wide longitudinal range and experiences large variations in tune shift. Generally, in bunched beams, each individual particle has various space-charge tune shifts, which forms the space-charge tune spread.

2.4.2 Longitudinal Space Charge

The treatment of longitudinal space charge within beams is based on the concept of longitudinal impedance(see, for example in Ref. [57]). It is different from the treatment of transverse space charge discussed above. As can be seen later, the longitudinal space charge is from the drop voltage induced by the longitudinal variation of beam density.

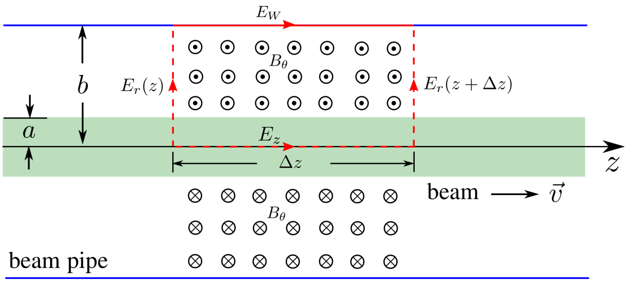

Figure 2.9.: Schematic drawing of electromagnetic field distribution for a coasting beam with a beam pipe. E_W and E_s are caused by impedance. The red dashed rectangular loop is the path integral of Faraday's law.

For a coasting beam with round cross section traveling inside a round beam pipe, the electromagnetic fields distributed inside the beam and outside the beam can be written as

$$E_r = \begin{cases} \dfrac{q\lambda r}{2\pi\epsilon_0 a^2} & \text{if } r \le a, \\[2em] \dfrac{q\lambda}{2\pi\epsilon_0 r} & \text{if } r > a, \end{cases} \qquad \text{and} \qquad B_\vartheta = \begin{cases} \dfrac{\mu_0 q\lambda\beta c r}{2\pi\epsilon_0 a^2} & \text{if } r \le a, \\[2em] \dfrac{\mu_0 q\lambda\beta c}{2\pi r} & \text{if } r > a, \end{cases} \tag{2.42}$$

where $\lambda = I/(q\beta c)$ is the line charge density. As shown in Fig. 2.9, the electric field E_r is in radial direction and the magnetic field B_ϑ is azimuthal and perpendicular to the page.

In coasting beams, the line charge density λ is constant. Now we consider a small perturbation on λ, $\lambda(s) = \lambda_0 + \frac{\partial\lambda(s)}{\partial s}$ with $\frac{\partial\lambda(s)}{\partial s} \ll \lambda_0$. The perturbation generates a longitudinal electric filed E_z inside the beam. According to Faraday's law

$$\oint \vec{E}\cdot d\vec{l} = -\frac{\partial}{\partial t}\int \vec{B}\cdot d\vec{S}, \tag{2.43}$$

where $d\vec{S}$ is the surface integral. Integrating along the loop marked with the red dashed line in Fig. 2.9, we obtain

$$\oint \vec{E}\cdot d\vec{l} = E_z\Delta z + \int_0^b E_r(z+\Delta z)dr + E_W(-\Delta z) + \int_b^0 E_r(z)dr, \tag{2.44}$$

where

$$\int_b^0 E_r(z)dr = \int_b^a E_r(z)dr + \int_a^0 E_r(z)dr = \frac{q g_0 \lambda(s)}{4\pi\epsilon_0}, \tag{2.45}$$

with the *geometry factor* $g_0 = 1 + 2\ln b/a$. Substituting the above equation to Eq. 2.44, we obtain

$$\oint \vec{E} \cdot d\vec{l} = (E_z - E_W)\Delta z + \frac{q g_0}{4\pi\epsilon_0}[\lambda(z+\Delta z) - \lambda(z)]. \tag{2.46}$$

Similarly, the surface integral of magnetic field becomes

$$\int \vec{B} \cdot d\vec{S} = \Big[\int_0^a \frac{\mu_0 q \lambda(s)\beta c r}{2\pi a^2} dr + \int_a^b \frac{\mu_0 q \lambda \beta c}{2\pi r} dr\Big]\Delta z = \frac{\mu_0 q \lambda(s) g_0 \beta c}{4\pi}, \tag{2.47}$$

and its time derivative is

$$-\frac{d}{dt}\int \vec{B} \cdot d\vec{S} = -\Delta s \frac{\mu_0 q \beta c g_0}{4\pi}\frac{\partial \lambda}{\partial t}. \tag{2.48}$$

Combining Eqs. 2.43, 2.46, and 2.48, the longitudinal electric field inside the beam has the form

$$E_z = E_W + \frac{q g_0}{4\pi\epsilon_0 \gamma^2 \beta c}\frac{\partial \lambda}{\partial s}, \tag{2.49}$$

where the factor $1/\gamma^2$ arises from the partial cancellation between the electric and magnetic fields. E_W represents the beam-pipe-induced electric field. By integrating of E_z along the circumference of accelerator, the total voltage after one turn induced by E_z on the beam takes the form

$$\Delta U_{\rm sc} = -q\beta c R \frac{\partial \lambda}{\partial s}\Big[\frac{g_0 Z_0}{2\beta\gamma^2} - \omega_0 L\Big], \tag{2.50}$$

where $Z_0 = 1/\epsilon_0 c \approx 377\Omega$ is the vacuum impedance and L is the inductance of the beam pipe. E_z in Eq. 2.49 is the longitudinal space charge field, and $\Delta U_{\rm sc}$ in Eq. 2.50 is the corresponding longitudinal space charge voltage.

3 Fundamentals of Intense Beam Dynamics

Charged particle beams, in which the electromagnetic fields (or *self field*) generated by the charged particles plays a significant role on the beam dynamics, refers as intense beams. As an intense beam travelling in an accelerator, the motion of the beam is influenced by both the space charge and the external focusing forces of the accelerator. In an intense beam, the self fields change both of the velocity and position of particles, which are presented as space charge in the previous chapter. It results in variation of charge density and particle distribution of the beam. On the other hand, the charge density and particle distribution are the sources of electromagnetic fields, which, together with external forces of accelerator elements, determine the self field and the motion of particles. Thus a *self-consistent* system forms between the self field and particle distribution (charge density) inside the beam. One deals with a closed loop in which the motion of the particle distribution and self fields interrelate and change each other.

In an intense beam travelling in an accelerator, the Coulomb interaction among the charged particles has an "immediate" collisional effect to the neighbor particles and a long range effect on the whole beam. For the physics of plasma point of view, where charged-particle beams can be seen as non-neutral plasmas [58], the Debye length for most practical beams for most practical beams is much larger that the average distance between two neighbor particles, and the collisional effect is rather small and can be neglected [54]. A widely-accepted method to solve the self-consistency problem of such collisionless-particle system is the Vlasov model [59], in which the Vlasov equation set, is combined with Liouville's theorm and Maxwell equation set to describe the beam dynamics in a self-consistent way. The time-independent solutions of Vlasov-Maxwell equation set define the *equilibrium* states of a particle distribution. To solve the self-consistent system based on the Vlasov model requires a truly theoretical model in which the particle distribution follows the closed loop. Up to now, the only known particle distribution that follows the closed loop self-consistently in alternating-gradient focusing accelerators is the Kapchinsky-Vladimirsky distribution or K-V distribution, discovered in 1959 [11].

As intense beams in accelerators can be seen as non-neutral plasmas in which collisions between particles can be neglected, one can introduce a "space charge potential" to characterize the smoothed effect of space charge acting over the whole beam. From this point of view, the beam as a whole exhibit a *collective* behavior under the combined influence of external focusing of the accelerator and self field of the beam. To compare the collective behaviors of beams with different particle distributions, the concept of equivalent beam and rms envelope equation was estabilished [12, 13] based on the comparison of the second moments of different particle distributions. The appraoch of rms envelope equation provides the information of particle motion in the statistical sense, and allows one to investigate the beam collective motion self-consistently in an rms sense. For an intense beam cycling in a synchrotron, the length of the beam usually is much larger than its transverse width. Therefore, analogy to the treatment of spac charge, beam motion can be seperated into transverse motion and longitudainl motion.

This chapter is organized as follows. We firstly introduce the K-V distribution in a self-consistent manner in Section 3.1. The envelope model for transverse beam motion are estabilished in Section 3.2. Section 3.3 discusses the beam envelope instabilities. In Section 3.4, we briefly discuss the longitudinal beam dynamics based on the longitudianl envelope equation.

3.1 The Kapchinsky-Vladimirsky (K-V) Distribution

The beam with the K-V particle distribution is named as K-V beam. In K-V beams, particles are random-uniformly distributed on the surface of a hyper-ellipsoid in the 4-dimensional phase space, with its elliptical projection in the 2-dimensional phase space. One major property of the K-V distribution is that it creates linear space charge forces inside the beam. In the following we will briefly give a self-consistent description of K-V beams.

We first consider a coasting K-V beam, which has an elliptical cross section and a uniform distribution in both x and y. This beam model has a sharp boundary with a constant beam density ϱ inside the beam, and $\varrho = 0$ outside the beam, as shown in Fig. 3.1. The ellipse describing the boundary of the beam obeys the equation

$$\frac{x^2}{X^2} + \frac{y^2}{Y^2} = 1, \tag{3.1}$$

and the density is

$$\varrho = \frac{I}{\pi v X Y} \tag{3.2}$$

within the boundary, and $\varrho = 0$ beyond the boundary. The electric and magnetic fields for such a distribution can be obtained according to the Gauss's law and the Stokes's law[1]

$$E_x = \frac{I}{\pi\epsilon_0\beta c}\frac{x}{X(X+Y)}, \qquad E_y = \frac{I}{\pi\epsilon_0\beta c}\frac{y}{Y(X+Y)}, \tag{3.3}$$

and

$$B_x = \frac{\mu_0 I}{\pi}\frac{y}{Y(X+Y)}, \qquad B_y = \frac{\mu_0 I}{\pi}\frac{x}{X(X+Y)}, \tag{3.4}$$

---

[1] see Eq. 2.33 and Eq. 2.35 in Chapter 2.

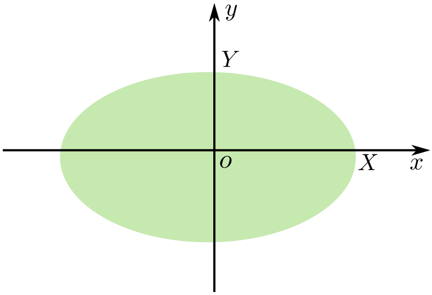

Figure 3.1.: Schematic drawing of the cross section of a K-V beam, on which particles distribute random-uniformly on the ellipse with the semi-major axis X and the major semi-axis Y.

where I is the beam current, βc is the speed of beam with c the speed of light, ϵ_0 and μ_0 are respectively the vacuum permittivity and vacuum permeability. It can be seen in Eqs. 3.3 that the electromagnetic fields $E_{x,y}$ and $B_{x,y}$ a particle feels are in proportion to the transverse position (x, y) of the particle. In the beam center, $E_{x,y} = B_{x,y} = 0$.

The linear space charge forces in x and y can be obtained by $F_x = q(E_x + vB_y)$ and $F_y = q(E_y + vB_x)$ from Eqs. 3.3 and Eqs. 3.4. In the presence of the linear space charge, the equations of transverse motion for a single particle of Eq. 2.8 in Chapter 2 is modified and takes the form[2]:

$$x'' + \kappa_x x = 0, \qquad y'' + \kappa_y y = 0, \tag{3.5}$$

with

$$\kappa_x = \kappa_{x0} - \frac{2K_{\text{sc}}}{X(X+Y)}, \qquad \kappa_y = \kappa_{y0} - \frac{2K_{\text{sc}}}{Y(X+Y)}. \tag{3.6}$$

Here, $\kappa_{x0,y0}$ are the external focusing strengths[3], $\kappa_{x,y}$ are the space-charge depressed external focusing strengths, $K_{\text{sc}} = 2N_L r_c/(\beta^2\gamma^3)$ is the space charge *perveance*, with N_L the number of particles per length, r_c the classical particle radius, β and γ the relativistic factors. Comparing Eqs. 3.5 with Eq. 2.8 indicates that the external focusing forces acted

---

[2] Here, Eqs. 3.5 are for K-V beams. The space-charge-modified Hill equation of Eq. 2.40 in Chapter 2 is for a more general coasting beam, independent of particle distributions.

[3] In the following, for brevity, we combine the subscripts in the same class of physical quantities. For example, κ_{x0} and κ_{y0} are written as $\kappa_{x0,y0}$.

on particles are depressed by the space charge. Eqs. 3.5 can be solved using a similar treatment of Eq. 2.8

$$\begin{aligned} x(s) &= \sqrt{\beta_x \epsilon_x} \cos[k_x(s) + \varphi_x], \\ y(s) &= \sqrt{\beta_y \epsilon_y} \cos[k_y(s) + \varphi_y], \end{aligned} \tag{3.7}$$

in which $\beta_{x,y}$ and $k_{x,y}$ denote respectively the space-charge-modified betatron functions and the space-charge-modified phase advance in x and y.

It can be seen from Eqs. 3.5 and Eqs. 3.7 that the transverse emittances $\epsilon_{x,y}$ of a single particle are independent of the presence of space charge forces, and keep constant during the particle travelling in the accelerator. In analogy to the case in the absence of space charge in subsection 2.1.3, the beam emittance in the presence of space charge can be defined by the maximum single particle emittance $\hat{\epsilon}_{x,y} = \epsilon_{x,y,max}$. Since both external focusing and space charge defocusing forces acted on particles in a K-V beam are linear, the beam emittance is constant during the beam transported in the accelerator.

Since a particle distribution function with invariants as its variables is a time-independent solution of Vlasov equation. One of such particle distributions can be chosen as K-V distribution, with its distribution function (see, for example, in Ref. [54])

$$f = f_0 \delta(\frac{\epsilon_x}{\hat{\epsilon}_x} + \frac{\epsilon_y}{\hat{\epsilon}_y} - 1), \tag{3.8}$$

in which $\epsilon_{x,y}$ and $\hat{\epsilon}_{x,y}$ are invariant variables, $f_0 = I/(\pi^2 q\beta c \hat{\epsilon}_x \hat{\epsilon}_y)$ is the normalization coefficient, and $\delta(x)$ is the Dirac delta function, with its definition,

$$\delta(x) = 0 \ \text{ for } \ x \neq 0, \ \text{and} \ \int_{-\infty}^{\infty} \delta(x) dx = 1. \tag{3.9}$$

The charge density can be obtained by the integral of the distribution function of Eq. 3.8,

$$\varrho = q f_0 \int_{-\infty}^{\infty} \int_{-\infty}^{\infty} \delta(\frac{\epsilon_x}{\hat{\epsilon}_x} + \frac{\epsilon_y}{\hat{\epsilon}_y} - 1) dx' dy' = q f_0 \pi \sqrt{\frac{\epsilon_x \epsilon_y}{\beta_x \beta_y}}. \tag{3.10}$$

By solving the possion equation with respect to the charge density ϱ

$$\nabla^2 \varphi = -\frac{\varrho}{\epsilon_0}, \tag{3.11}$$

we can obtain the electric potential distribution inside beam

$$\varphi(x, y) = -\frac{\varrho}{4\epsilon_0} \left[x^2 + y^2 - \frac{X - Y}{X + Y}(x^2 - y^2)\right]. \tag{3.12}$$

The self-consistency of K-V distribution can be shown as follows. K-V beams generating electromagnetic field in Eq. 3.3 and Eq. 3.4, results in space-charge-modified linear equation of motion of Eqs. 3.7 with linear space charge forces and invariant emittances. On the other hand, the distribution function in Eq. 3.8, which is based on the invariant emittances, can generate the electric potential in Eq. 3.12, from which Eq. 3.3 can be obtained. In conclusion, for beams with K-V distribution the charge density and the electric and magnetic fields are associated in a self-consistent way.

3.2 Envelope Descriptions of Beam Motion

The K-V beam model described above allows one to investigate beam behavior with space charge in a self-consistent manner. However, for realistic beams the particle distribution is close to a Gaussian distribution due to thermal equilibrium inside the beam. Besides, there are sereral other distributions that are commonly used in computer simulations, for instance, the *waterbag distribution*[4]. For both Gaussian and waterbag distribution, the space charge forces are nonlinear and the distribution evolves under the combined influence of external focusing and nonlinear space charge. The two distributions are not self-consistent in the alternating focusing channels in accelerators[5]. In order to characterize and compare beam dynamics with various particle distributions, Lapostolle [12] and Sacherer [13] introduced the rms beam envelope equations.

3.2.1 Second Moments of Beams

Before we introduce the rms envelope equations, we will first discuss briefly some relevant definitions of second moments of beams. For a beam with the normalized particle distribution function $f(x,x',y,y')$, the second moment in x-direction can be obtained by

$$\langle x^2\rangle = \int x^2 f(x,x',y,y')dxdydx'dy', \tag{3.13}$$

with

$$\int f(x,x',y,y')dxdx'dydy' = 1. \tag{3.14}$$

Here, x, x', y and y' are transverse coordinates of particles in the phase space. The rms beam size (in x) is defined as the square root of the second moment of x,

$$\sigma_x = \sqrt{\langle x^2\rangle}, \tag{3.15}$$

---

[4] The waterbag distribution is characterized with particles distributing random-uniformly inside the hypersphere in four-dimensional phase space. For more details see Ref.[54].

[5] The two distributions can be shown to be self-consistent for constant focusing system based on the Vlasov-Maxwell approach. For more details see Ref.[54].

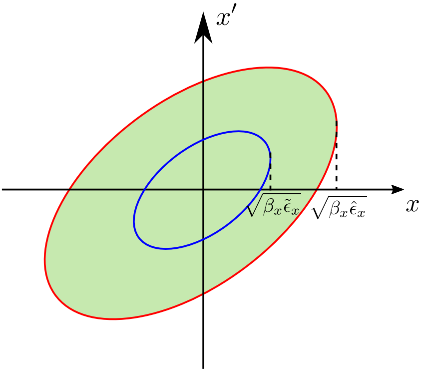

Figure 3.2.: The emittance $\hat{\epsilon}_x$ and the rms emittance $\tilde{\epsilon}_x$ of a K-V distribution.

and similar for σ_y. The rms beam sizes $\sigma_{x,y}$ characterize the motion of the beam in an rms sense. The rms beam emittance (in x) is defined as

$$\tilde{\epsilon}_x = \sqrt{\langle x^2 \rangle \langle x^2 \rangle - \langle x x' \rangle^2} \tag{3.16}$$

and similar for y-direction. Here, $\langle x^2 \rangle$ and $\langle x^2 \rangle$ are respectively the second moments of x and x'. $\langle x x' \rangle$ is defined by

$$\langle x x' \rangle = \int x x' f(x, x', y, y') dx dy dx' dy', \tag{3.17}$$

which characterizes corelation between x and x'. In Chapter 2, the beam emittance $\hat{\epsilon}_z$ defined by the maximum single particle emittance (see Eq. 2.17) represents the largest ellipse in the phase space (Fig. 2.2), and the quantity $\sqrt{\beta_{0,z} \hat{\epsilon}_z}$ represents the beam width. Similarly, the rms emittance defines a concentration ellipse with its area satisfying $\tilde{\epsilon}_z^2 = \overline{(\hat{\epsilon}_z)}^2$, and the relation between the rms beam size and the rms emittances is

$$\sigma_z = \sqrt{\beta_{0,z} \tilde{\epsilon}_z}. \tag{3.18}$$

Here, z denotes x or y. Here $\beta_{0,z}$ is the beta function defined in Eqs. 2.9. Eq. 3.18 shows that for a given emittance, the beam size is in proportion to beta function. The beta function is a essentail characteristic for accelerator design.

The relation between the beam emittances, beam sizes and the their corresponding rms quantities depend on the specific particle distribution. For instance, in a K-V distribution as shown in Fig. 3.2, the area of rms emittance is one quarter of the area of beam emittance, and the rms beam size is half of the beam size.

3.2.2 RMS Envelope Equations

Based on the second moments $\sigma_{x,y}$ and $\tilde{\epsilon}_{x,y}$ defined above, and along with the equation of single particle motion in Eq. 2.40, the rms envelope equation can be derived and takes the form[6],

$$\begin{aligned} \sigma_x'' + \kappa_{0,x}(s)\sigma_x - \frac{K_{\rm sc}}{2(\sigma_x+\sigma_y)} - \frac{\tilde{\epsilon}_x^2}{\sigma_x^3} = 0, \\ \sigma_y'' + \kappa_{0,y}(s)\sigma_y - \frac{K_{\rm sc}}{2(\sigma_x+\sigma_y)} - \frac{\tilde{\epsilon}_y^2}{\sigma_y^3} = 0. \end{aligned} \tag{3.19}$$

Here $\sigma_{x,y}$ are the transverse rms beam sizes, $\tilde{\epsilon}_{x,y}$ are the rms beam emittances. $K_{\rm sc}$ is the space-charge perveance defined in Eqs. 3.6. The two equations describe the envelope motion in x and y direction respectively, and are coupled with each other due to space charge. Compared to the equation of motion in Eq. 2.40, which governs the motion of single particle, the equations of motion in Eq. 3.19 describe the beam *collective* motion (or coherent motion) under the external focusing force and space charge. Two beams having the same rms transverse beam sizes and rms transverse emittances are *rms equivalent beams*. If travelling in identical focusing channels, equivalent beams have the same dynamical behavior, which can be described by the rms envelope equations.

3.2.3 Matched Beams

Most modern accelerators, which are designed based on the principle of alternating gradient focusing [7], are composed of various accelerator elements (i.e., multipole magnets and rf cavities) for beam focusing and acceleration. In other words, the external focusing coefficients $\kappa_{0,x}$ and $\kappa_{0,y}$ in Eqs. 3.19 are functions of the longitudinal variable s. The corresponding rms envelope equations of Eqs. 3.19 are nonlinear differential equations with variable coefficients. For a set of initial conditions, i.e., rms beam sizes and their derivatives, $\sigma_x(0)$, $\sigma_x'(0)$, $\sigma_y(0)$ and $\sigma_y'(0)$, the solution functions $\sigma_x(s), \sigma_x'(s), \sigma_y(s), \sigma_y'(s)$ can be found from Eq. 3.19 numerically. For a well-designed ideal accelerator, there exists a unique set of initial condition $\sigma_{x0}(0)$, $\sigma_{x0}'(0)$, $\sigma_{y0}(0)$ and $\sigma_{y0}'(0)$, after the beam travelling in one periodic structure with length L, the solutions of the rms envelope equations $\sigma_{x0}(L), \sigma_{x0}'(L), \sigma_{y0}(L), \sigma_{y0}'(L)$ satisfy:

$$\begin{aligned} \sigma_{x0}(L) = \sigma_{x0}(0), \quad \sigma_{x0}'(L) = \sigma_{x0}'(0), \\ \sigma_{y0}(L) = \sigma_{y0}(0), \quad \sigma_{y0}'(L) = \sigma_{y0}'(0). \end{aligned} \tag{3.20}$$

---

[6] The detailed derivation of the rms envelope equation are presented in Appendix A.

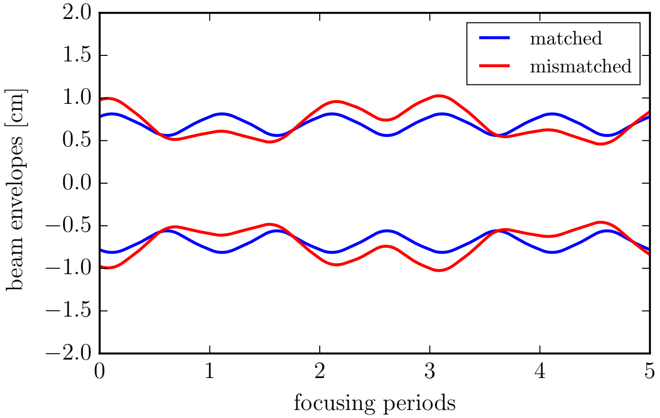

Figure 3.3.: An example of numerical solutions of Eqs. 3.19. The rms envelopes of the matched beam and a mismatched beam in five alternating gradient focusing periods.

Here we use the subscript ‘0’ after x and y to denote the matched case. The solution satisfying Eq. 3.20 is called *matched solution*, and the beam in such case is called matched beam. For a matched beam, after transported one periodic structure, the second moments of the beam are equal to the initial values[7]. Since the envelope equations describe the beam motion under the lattice structure and the space charge effect. The beam satisfying Eqs. 3.20 is matched to both the lattice and space charge.

The envelope equations in Eqs. 3.19 can be solved numerically. Using a numerical iterative solution method (the shooting method for instance [60]), the matched sloution can be found. Fig. 3.3 illustrates an example of a mathced beam and a mismatched beam in five peroidic cells of the SIS-18 lattice. More details about the numerical algorithm will be discussed in the next chapter.

3.2.4 Space-Charge Modified Twiss Parameters

The Twiss parameters $\beta_{0,z}$, $\alpha_{0,z}$, and $\gamma_{0,z}$ defined in Section 2.1.2 are basic characteristics of an accelerator, and are dependent on the configuration of the accelerator, for example, the external focusing strengths of multipole magnets, and specific sequence of accelerator elements. In the presence of space charge in a high-intensity beam travelling in an accelerator, the external focusing strengths are depressed due to defocusing space charge. To characterize the effective focusing acted on the beam, the concept of space-

---

[7] It is worth pointing out that while the second moments of the beam recover to the initial values, for each inidividual particle, the coordinates x and x' are different from the initial values.

charge-modified Twiss parameters is introduced, based on the matched solutions of the rms envelope equations. For example, similar to the Eq. 3.18, the space-charge-modified beta function β_z is defined as

$$\beta_z = \frac{{\sigma_{z0}}^2}{\tilde{\epsilon}_z}. \tag{3.21}$$

Here, z denotes x or y. The other two Twiss parameters can be obtained by $\alpha_z = -(\beta_z)'/2$ and $\gamma_z = (1+\alpha_z^2)/\beta_z$. The space-charge-modified Twiss parameters, which are dependent on both accelerator configurations and the beam properties, characterize the interaction between the beam envelope motion and the space charge within the beam in a self-consistent way. Equivalent beams travelling in identical accelerator channels have the identical space-charge-modified Twiss parameters.

Analogy to the definition for the phase advance of the motion of a single particle in Eq. 2.10, the space-charge-modified phase advance for a high-intensity beam can be defined as

$$k_z(s) = \int_0^s \frac{d\tilde{s}}{\beta_z(\tilde{s})} = \tilde{\epsilon}_z \int_0^s \frac{d\tilde{s}}{\sigma_{z0}^2}. \tag{3.22}$$

Clearly, the space-charge depressed phase advance is decreasing with space charge increasing. It plays a key role in the analysis of beam instability, which will be discussed in the following.

3.2.5 Smooth Approximation

When the variation of the transverse beam size during one focusing period is much smaller than the average transverse beam size, the alternating focusing structure can be approximated by a constant focusing structure, with the periodic focusing forces $\kappa_{0,x}(s)$ and $\kappa_{0,y}(s)$ replaced by their average constant values $\bar{\kappa}_{0,x}$ and $\bar{\kappa}_{0,y}$. The equations of envelope become

$$\begin{aligned} \bar{\sigma}_x'' + \bar{\kappa}_{0,x}\bar{\sigma}_x - \frac{K_{sc}}{2(\bar{\sigma}_x+\bar{\sigma}_y)} - \frac{\tilde{\epsilon}_x^2}{\bar{\sigma}_x^3} &= 0, \\ \bar{\sigma}_y'' + \bar{\kappa}_{0,y}\bar{\sigma}_y - \frac{K_{sc}}{2(\bar{\sigma}_x+\bar{\sigma}_y)} - \frac{\tilde{\epsilon}_y^2}{\bar{\sigma}_y^3} &= 0. \end{aligned} \tag{3.23}$$

This is usually called the smooth approximation in literatures [61]. For a constant focusing structure, the transverse rms beam sizes of a matched beam are constant. It means that the matched solution of Eqs. 3.23 can be solved from the corresponding algebraic equations

$$\begin{aligned} \bar{\kappa}_{0,x}\bar{\sigma}_{x0} - \frac{K_{sc}}{2(\bar{\sigma}_{x0}+\bar{\sigma}_{y0})} - \frac{\tilde{\epsilon}_x^2}{\bar{\sigma}_{x0}^3} &= 0, \\ \bar{\kappa}_{0,y}\bar{\sigma}_{y0} - \frac{K_{sc}}{2(\bar{\sigma}_{x0}+\bar{\sigma}_{y0})} - \frac{\tilde{\epsilon}_y^2}{\bar{\sigma}_{y0}^3} &= 0. \end{aligned} \tag{3.24}$$

One of the most significant advantages of the smooth approximation is that the matched solution of Eqs. 3.23 $\bar{\sigma}_{x0}$ and $\bar{\sigma}_{y0}$, which can be seen as the approximated matched solution of Eqs. 3.19, can be found easily by solving Eqs. 3.24.

3.3 Beam Envelope Instabilities

The matched solutions of beam envelope equations are of essential important in accelerator design and research, since they represent the maximum beam intensity that can be transported in an accelerator channel. In practice, however, an ideal matched beam is difficult to achieve, since there are always exist magnet imperfections, misalignment, ion sources errors and so on. Beams in realistic cases perform envelope mismatch oscillations around the matched solutions, as shown in Fig. 3.3. The amplitudes of the mismatch oscillations are usually much smaller than the average rms beam size, which allow a good beam travelling in accelerators. Sometimes for a beam with sufficient beam in certain accelerator configurations, the beam mismatch oscillations lead to the instability of the beam. In this subsection we perform to analyze the properties of mismatch oscillation and introduce the well-known envelope instability [17].

3.3.1 Mismatch Oscillations

Let us start with slightly mismatched rms envelopes σ_x, σ_y with small perturbations ξ, ζ

$$\begin{aligned} \sigma_x &= \sigma_{x0} + \xi, \\ \sigma_y &= \sigma_{y0} + \zeta, \end{aligned} \tag{3.25}$$

where σ_{x0} and σ_{y0} are the matched solutions of Eq. 3.19. Substituting Eq. 3.25 into Eq. 3.19 and neglecting the higher order terms, we obtain the perturbation equations

$$\begin{aligned} \xi'' + \kappa_{0,x}\xi + \frac{K_{sc}}{2(\sigma_{x0}+\sigma_{y0})^2}(\xi+\zeta) + \frac{3\epsilon_x^2}{\sigma_{x0}^4}\xi &= 0, \\ \zeta'' + \kappa_{0,y}\zeta + \frac{K_{sc}}{2(\sigma_{x0}+\sigma_{y0})^2}(\xi+\zeta) + \frac{3\tilde{\epsilon}_y^2}{\sigma_{y0}^4}\zeta &= 0, \end{aligned} \tag{3.26}$$

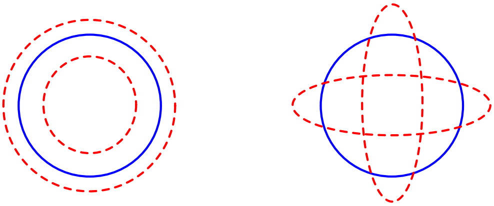

(a) Breathing oscillation (b) Quadrupolar oscillation

Figure 3.4.: Schematic drawing of the oscillations of the two eigenmodes.

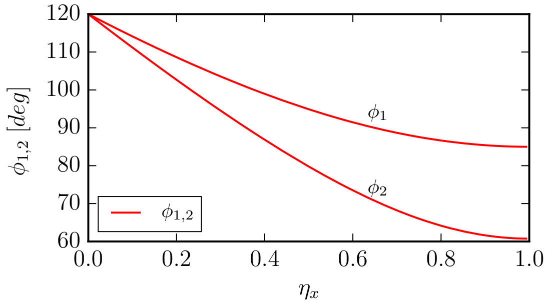

Figure 3.5.: Round beam case,$k_{0,x} = k_{0,y} = k_0 = 60°$: Phase shifts $\varphi_{1,2}$ of the fundamental mismatch oscillation versus tune depression in x.

which is a coupled differential equation system with its coefficients being functions of the matched beam sizes (σ_{x0} and σ_{y0}). Two *envelope modes* in Eqs. 3.26 can be decoupled to characterize the mismatch oscillations. To show the properties of the envelope modes, for simplity here we take an example of mismatch oscillation of a round beam with $\sigma_{x0} = \sigma_{y0}$, and $\tilde{\epsilon}_x = \tilde{\epsilon}_y$ travelling in a symmetric constant focusing channel. The phase shifts of the two envelope modes are[8]

$$\varphi_1 = \sqrt{k_{0,z}^2 + 3k_z^2}, \qquad \varphi_2 = \sqrt{2k_{0,z}^2 + 2k_z^2}. \tag{3.27}$$

Here $k_{0,z}$ and k_z is the phase advance without and with space charge, respectively. φ_1 and φ_2 represents the phase shifts of the two modes, i.e., the well-known quadrupolar mode and the breathing mode[9]. The mismatch oscillations characterized by the two envelope modes are schematiclly shown in Fig. 3.4. The blue solid line denotes the transverse cross section of a matched round beam, and the red dashed lines are the mismatch oscillations.

---

[8] For details of the derivation see Appendix B.

[9] In many literatures, the two modes are also named as “fast mode” and “slow mode”.

(a) Mismatch oscillation (b) Instability

Figure 3.6.: Mechanical analogy of mismatch oscillation and instability.

Since the phase shifts of the two envelope modes in Eq. 3.27 are functions of space-charge-modified phase advance, they are dependent on beam intensity. With higher space charge, the phase shifts are decreasing. Fig. 3.5 illustrates an example of the evolution of the two phase shifts as functions of beam intensity. Here, we introduce the *tune depression* η_z $(0 \le \eta_z \le 1)$ to represent the beam intensity, defined by the ratio of the the space-charge phase advance shift to the phase advance without space charge,

$$\eta_z \equiv \frac{k_{0,z} - k_z}{k_{0,z}} = \frac{\Delta k_z}{k_{0,z}}. \tag{3.28}$$

Clearly, $\eta_x = 0$ represents the limit of zero beam current, while $\eta_x \to 1$ is for the strong space charge approaching to the space charge limit. As can be seen in the plot, with beam current increasing, the phase shifts of the two modes decrease from $2k_0$, and approaching to $\sqrt{2}k_0$ and k_0 in the space charge limit, which is in agreement with Eq. 3.27.

3.3.2 Envelope Instabilities

For a beam experiencing focusing forces periodically in accelerators, in some cases, the mismatch enveloep oscillation of the beam triggers the envelope instability (For a mechanical analogy see Fig. 3.6), characterized by a resonance between the two envelope modes, or between envelope modes and the periodic structure. The envelope instability is a beam collective effect, and can be investigated with the stability analysis by integrating Eqs. 3.26 over one periodic focusing structure (from m to $m+1$)

$$\boldsymbol{\tau}_{m+1} = M\boldsymbol{\tau}_m, \tag{3.29}$$

where M is the map for the perturbation vector $\boldsymbol{\tau} = (\xi, \xi', \zeta, \zeta')$ over one periodic cell. As $\{\sigma_x, \sigma'_x, \sigma_y, \sigma'_y\}$ in Eqs. 3.19 follow a Hamiltonian [62], the four eigenvalues of M: $\lambda_i = |\lambda_i|e^{i\varphi_i}$ $(i = 1, 2, \ldots, 4)$ exist only as reciprocal or as conjugate in two pairs: $\{\lambda_1, \lambda_1^*\}$, $\{\lambda_2, \lambda_2^*\}$. Moreover, taking each oscillation mode in the absence of space charge as reference, we can select a suitable set of phase shifts $\{\varphi_1, \varphi_2\}$ with corresponding moduli $\{|\lambda_1|, |\lambda_2|\}$ representing the two envelope modes to characterize the beam oscillation system without loss of generality.

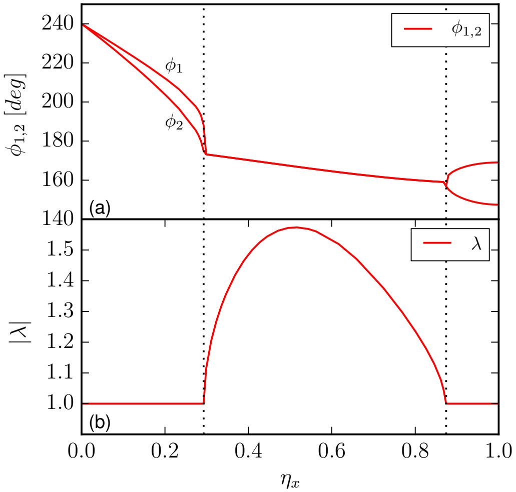

Figure 3.7.: $k_0 = 120°$ case. Upper: Phase shifts φ_1 and φ_2 versus tune depression; Lower: Growth factor $|\lambda|$ versus tune depression. (The region between the dashed line denotes the stop band of the envelope instability.

The eignevalues with their moduli equal to unity indicate the fact that after travelling through one periodic cell, the amplitude of mismatch oscillation of the beam remains constant. In comparison, one of the moduli larger than unity indicates that the amplitude of mismatch oscillation will accumulate and amplify after each periodic cell. For detailed analysis of the movement of the four eigenvalues under different beam intensity see Appendix C.

Struckmeier et al. [17] shows that for beams of sufficiently high current, the envelope instabilities will occur in a peridic structure with phase advance larger than 90°, characterized with one of two moduli larger than unity. The envelope instabilities can be classified as follows,

1. One or both eigenvalue pairs lie on the real axis, $k_1 + k_2 = 180°$;
2. The phase shift of the modes satisfies $k_1 = k_2$ or $k_1 + k_2 = 360°$.

The first case is called *parametric resonance*, characterized by the resonance between the focusing structure and the fundamental modes. The second case is *confluent resonance*, in which the two fundamental modes are confluent.

The envelope instabilities must be distinguished from the fourth-order single particle resonance [26], which is driven by the octopolar terms in space charge potential. Both of the envelope instabilities and single particle resonance are driven by space charge and have the overlapping stop bands of larger than 90°. The difference between them is: The former is a collective effect, which are characterized by resonance of the modes

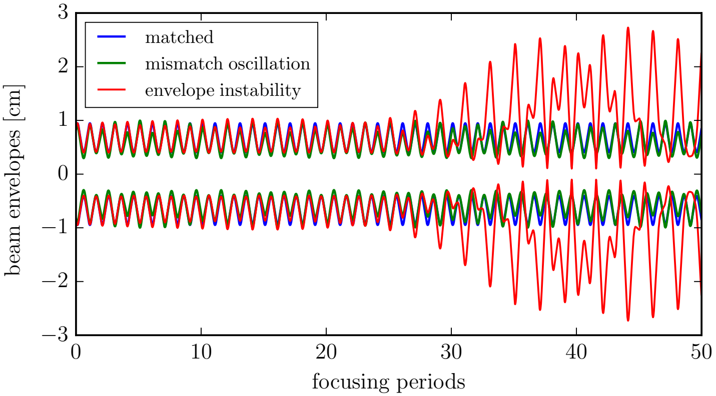

Figure 3.8.: The evolution of the beam rms envelope with mached, envelope mismatch oscillation, and envelope instability.

in the beam. The later, however, is a single particle effect, in which individual particles are trapped in the four characteristic resonant islands. In chapter 7, the mechanism difference between them will be further discussed.

3.4 Introduction to Longitudinal Beam Dynamics

The envelope model introduced above is developed for the transverse beam dynamics. In the following we briefly introduce the equation of longitudinal beam envelope to describe the longitudinal dynamics.

3.4.1 Parabolic Distribution

The self-consistent K-V model introduced in Section 3.1 provides the foundation for the envelope descriptions of transverse intense beam motion. In the longitudinal plane, the *parabolic distribution* developed by Neuffer [63] generates linear longitudinal space charge forces, which is a self-consistent distribution for longitudinal motion. In a parabolic beam, the line density of a parabolic distributin are uniformly distributed along the beam. Fig. 3.9 gives the longidudinal section of a parabolic beam. Here, s is the direction of the beam travelling along the accelerator, and x is the transverse coordinate. The elliptical contour of the parabolic distribution in Fig. 3.9 satisfies

$$\frac{x^2}{x_m^2} + \frac{s^2}{l_m^2} = 1, \tag{3.30}$$

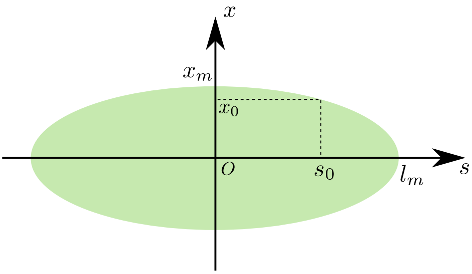

Figure 3.9.: Schematic drawing of the parabolic distribution, on which particles distribute random-uniformly on the ellipse with the semi-major axis l_m and the semi-minor axis x_m.

and similar for the case in the $y-s$ plane,

$$\frac{y^2}{y_m^2}+\frac{s^2}{l_m^2}=1. \tag{3.31}$$

The line charge density at the position $s=s_0$ can be calculated by the area of the ellliptical cross section

$$\lambda_{s0}=\varrho_0\pi x_0 y_0=\varrho_0 x_m y_m(1-\frac{s_0^2}{l_m^2}), \tag{3.32}$$

in which $\varrho_0=$ is the uniform volume charge density, with Q is the total charge of the beam. The line density at the beam center $s=0$ is

$$\lambda_0=\frac{3Q}{4l_m} \tag{3.33}$$

Neuffer [63] showed that the parabolic distribution generates the longitudinal space charge forces insdie the beam, based which one can derive the longitudinal envelope equation.

3.4.2 Longitudinal Envelope Equations

The linearized equations of synchrotron motion for a single particle of Eq. 2.28 takes the form

$$\frac{d^2\varphi}{dt^2}=\frac{hq\eta V\cos\varphi_s}{2\pi E}\varphi, \tag{3.34}$$

where φ and φ_s are the phase of the single particle and the synchronous particle. q and $E = \gamma m_0 c^2$ are the charge and the energy of the particle. h is the harmonic number, and η the slip factor. V is the rf voltage. With the relation $d\varphi/dt = \beta c d\varphi/ds$ and $d\varphi = Rdz$, (Here z is the longitudinal coordinate and R is the average radius of the synchrotron), for a beam with parabolic distribution, the longitudinal envelope equations can be derived[10] from Eq. 3.34

$$z_m'' + \kappa_{z0} z_m - \frac{K_L}{z_m^2} - \frac{\varepsilon_L^2}{z_m^3} = 0, \tag{3.35}$$

in which, z_m is the half length of the parabolic beam, and κ_{z0} represents the linearized external rf focusing strength given by

$$\kappa_{z0} = qV \cos\varphi_s h\eta/(2\pi R^2 \gamma \beta^2 m_0 c^2). \tag{3.36}$$

The linearized external focusing gradient modified by longitudinal space charge is $\kappa_z = \kappa_{z0} - K_L/z_m^3$, with the longitudinal perveance $K_L = 3gNZ^2 r_p/(2\beta^2\gamma^5 A)$; the geometry factor $g = 0.5 + 2\ln(R_p/R_b)$ (R_p and R_b are the radii of the beam pipe and the beam, respectively); N the number of particles in the bunch; r_p the classical proton radius and η the slip factor. ε_L is the longitudinal emittance, defined as

$$\varepsilon_L = |\eta| z_m \delta_0, \tag{3.37}$$

in which δ_0 is the momentum spread at the center of the bunch. Physically, ε_L denotes the area in longitudinal phase space, which is constant without acceleration.

---

[10] For more details of derivation, see Ref. [54]

4 Numerical Calculation and PIC Simulation

In previous chapters, we have introduced the fundamentals of intense beam dynamics, including the dynamics of single particle and beam envelope motion. In the presence of both external focusing and smoothed effect of the self field, an intense beam as a whole performs *coherent* behaviors described by the motion of its rms envelope, and it is unrealistic and unnecessary to calculate the Lorenz force acted on each particle in the beam. Before we further investigate the motion of intense beams, in this chapter we shall pay specific attention to two main approaches adopted in the following chapters: the numerical calculation and particle-in-cell simulation. Firstly, section 4.1 introduces the method of numerical calculation. The scheme of simulation with space charge and the relevant simulation code is briefly introduced in section 4.2. In section 4.3, comparison of results of a few examples will be presented to show the benchmarking of the two methods.

4.1 Numerical Calculation

The rms envelope approach and the concept of equivalent beams form the foundation of the theory of beam dynamics with space charge. The solutions of matched beam motion can be obtained from the envelope equations of Eq. 3.19, and beam stability can be analyzed by calculating the envelope modes from the mismatched oscillations of Eq. 3.26. In the general case, coefficients of the envelope equations representing external focusing forces are piecewise functions of position s according to the principle of alternating gradient focusing. Mathematically, to obtain the analytical solution of the differential equations with variable coefficients is formidable, and the only possible solution for most cases is the numerical one.

In the work of this thesis, the matched solutions and envelope modes are numerically calculated via a envelope solver code “pyKV”[1], written by Prof. Oliver Boine-Frankenheim, and further developed by the author. The code is written in Python [64] and consists of two script files, one (named as “pyLine”) is used to input the lattice parameters from output files of MAD-X [53]. Another file “pyEnvelope” is for solving the envelope equations as the initial parameters from the file “pyLine”. In the numerical calculation, the iterative scheme and shooting method in the Python-based package

---

[1] For instance, the envelope plots of Fig. 3.3 and Fig. 3.8, and the envelope modes in Fig. 3.5 and Fig. 3.7 are all calculated from the numerical code.

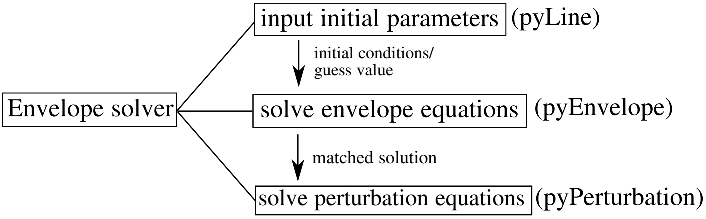

Figure 4.1.: Structure of the envelope solver code.

Numpy [65] and Scipy [66] are employed to find the matched solutions. The perturbative calculation can be achieved in the third script file “pyPerturbation”, in which, Newton’s method in matrix form is used to solve the envelope oscillation equations with the matched solutions from “pyEnvelope” as the coefficients. The structure of the envelope solver is shown in Fig 4.1.

4.2 PIC Simulaton

Another widely-used approach to study the beam dynamics is the simulation programs of particle-tracking. Various simulation programs are developed in many famous accelerator laboratories. In these programs, thousands of macro particles representing numerous charged particles in real beams, are tracked based on accurate calculation of the equations of motion of each macro particle in both of electromagnetic fields of each accelerator components and the self field of the beam. The detailed information of their motion (coordinates, speed, energy) are recorded and output. With the advantage of precise controlling and flexible adjustment to beam parameters and nearly zero cost, simulation programs are powerful tools and widely used for the design, commission and operation of accelerators.

4.2.1 Computational Model of Space Charge

For the simulation of intense beams, accurate calculation of space charge is of essential importance. The well-accepted computational model for treatment of space charge is the scheme of particle-in-cell (PIC for short) [67, 68]. As shown in Fig. 4.2, for each time cycle, the distribution of particles in a beam is interpolated onto a grid, with the charge assigned to grid nodes (Weighting). Then, the potential and the corresponding interpolated electromagnetic fields is obtained from the solution of the Poisson equation (Integration). The electromagnetic forces, combined with external forces, are acted on particles and the particle distribution is updated from the results of the combined forces.

In principle, the calculation of space charge is a three dimensional (3-D) problem, where a 3-D grid is required for weighting the 3-D particle distribution. This is the case for linacs, where the transverse and longitudinal sizes of the bunch are comparable.

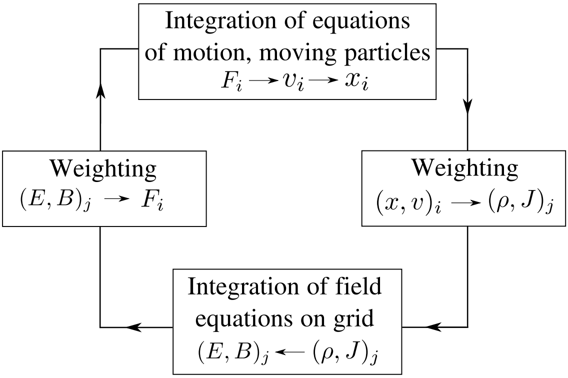

Figure 4.2.: A typical cycle of PIC in a particle simulation program. The particle are numbered as i, the grid indices are j. (Figure from Ref. [68])

However, for circular accelerators, where the longitudinal bunch size is much larger than transverse size, an alternative method of “2.5-D space charge model” is widely used. In the 2.5-D scheme, the 3-D particle distribution is interpolated onto a set of 2-D grids transversely and a set of slices longitudinally. Transverse space charge is calculated from PIC scheme solving the 2-D Poisson equations, and longitudinal space charge are evaluated based on the fluctuations of the linear charge density of the beam. For the case of coasting beams, where longitudinal fluctuations is absent, transverse beam profile is independent on the longitudinal position. This allows us to reduce the calculation of transverse space charge fields to a 2D problem. For the case of long bunched beams, however, the longitudinal fluctuation in line density (longitudinal space charge), and the problem of long bunched beams is 2.5-D. In the 2.5-D PIC simulation, the number of grid points for 2-D transverse space charge is chosen to be sufficiently large to reduce the grid dependent noise [69], and the number of slices for 1-D longitudinal space charge are checked by obtaining a smooth longitudinal space charge force.

4.2.2 PyORBIT

In the work of this thesis, the simulation code PyORBIT [70] is used to perform particle tracking with space charge. pyORBIT is a modern implementation of the original ORBIT (Objective Ring Beam Injection and Tracking) [71] that was developed at Oak Ridge National Laboratory to improve the Spallation Neutron Source accelerator ring design and to study proton beam dynamics in the presence of collective effects.

In pyORBIT, macro particles are contained in bunches and can interact with each other via self fields (space charge) or through the electromagnetic fields induced in the accelerator elements (impedances). At present, PyORBIT has two space charge models for linacs and one for rings: For linacs there are two alternative methods in pyORBIT:

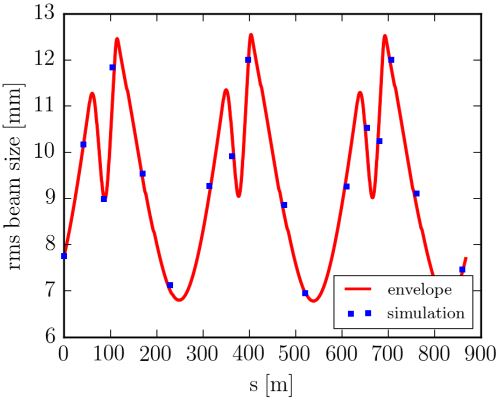

Figure 4.3.: Comparison of rms beam size for three periodic cell between simulations and envelope equation.

3-D uniformly charged ellipsoid field and a 3-D FFT Poisson solver. For circular accelerators, the 2.5-D PIC scheme based on the convolution method [67] is employed in pyORBIT.

4.3 Benchmarking and Comparison

In order to show the correctness and effectiveness of the two approaches of the numerical envelope calculation and PIC simulations, in this section we give three examples, each of which has the results from the two methods.

In the first example, we calculate the transverse rms size of a beam transported in periodic cells of the SIS-100 synchrotron. Both effects of space charge and dispersion are considered[2]. As shown in Fig. 4.3, the solid line represents the rms beam size calculated from envelope approach, and the dotted line represents the rms beam size at the entrance of each element obtained from PIC simulation. It is shown that the two resluts are in good agreement.

The second example is the benchmarking of space charge calculation. Fig.4.4 shows the space charge forces acted on each macro particle inside a K-V beam, calculated by the PIC solver in the code pyORBIT, compared with the theoretical results by using the formula of the space charge perveance in Eq. 3.6. It can be seen that for K-V beams, the distribution of space charge forces obtained from PIC solver is linear and agrees well with the theory.

In the third example, we show space-charge tune spread in a beam with Gaussian distribution, truncated at 3σ (here σ is the standard deviation.). The bare tune $Q_{0,x} =$

---

[2] For details of intense motion with dispersion see chapter 6

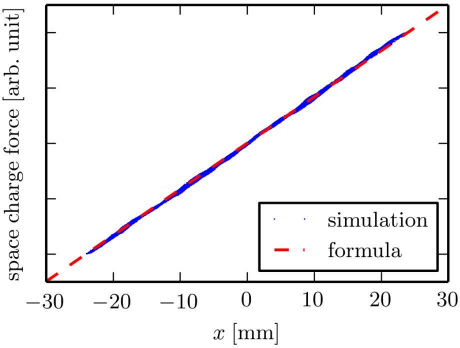

Figure 4.4.: Comparison of the transverse space charge forces in a K-V beam calculated from pyORBIT and theoretical formula.

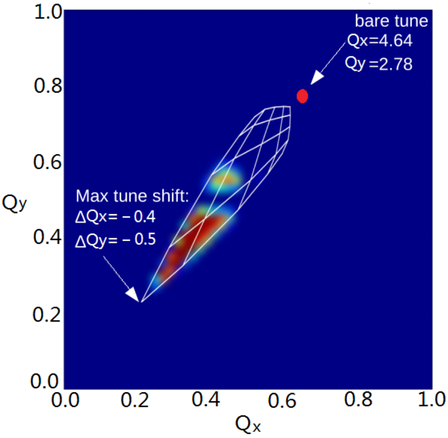

Figure 4.5.: Comparison of the space-charge tune spread in a Gaussian beam calculated from pyORBIT and theoretical formula.

4.64, $Q_{0,y} = 2.78$, as shown in Fig. 4.5. The diamond in write line represents the tune spread from a theoretical formula [72], the color area, which fills the write line, denotes the distribution of space-charge depressed tune for the Gaussian beam, obtained from pyORBIT. It can be seen that the color area mainly fills at the lower half part of the diamond. This is because the edge particles, which has small tune spread, has been cut off in the truncated Gaussian distribution.

5 Complete Set of Second-Moment Instabilities

The envelope equations introduced in Chapter 3 are based on the second moments of beams. The corresponding envelope modes, which characterize the beam envelope oscillations and envelope instabilities, are also well-known as the "second order *even* modes". Besides the even modes, there exists second order *odd* modes[1]. Different from the even modes, which are led by the mismatched oscillations of rms beam sizes, the odd modes are caused by the coupling effects between the two transverse directions (x and y), either from self rotation of the beam, or external skew strength, e.g., skew quadruple or solenoid. Analogy to the fact that the second order even modes can trigger the envelope instability, the second order odd modes can trigger the "tilting instability", characterized with the resonant emittance exchange by space charge coupling [73, 74, 75]. Furthermore, in periodic focusing channel with sufficiently different phase advances, the "sum envelolpe instability" can be excited by either the second order even modes, or the odd modes [22, 76].

In this chapter, we will present the complete set of second-moment instabilities driven by the second order even and odd modes and their sum effects. This is achieved by employing a unified equation set of second-moment oscillations derived from the "Chernin equations" [2].

This chapter is organized as follows. In section 5.1, we first extract the second-moment oscillation equations without external skew strength from Chernin equations. This is followed by calculating the frequencies of second order odd modes and showing the "tilting instability"in a constant focusing structure in section 5.2; furthermore a comparison with the results derived from Vlasov-Maxwell equation in Ref. [1], as well as a Fourier analysis of noise spectra from a 2-D PIC simulation. Finally, in section 5.3 we explore the theoretical mechanism of sum envelope instabilities, including both the coupled even mode sum instability and the odd mode sum instability. Full stop bands are calculated and compared with PIC simulation results including particle evolution in real space.

For clarity, in the following we assume x and y are the transverse degrees in horizontal and vertical direction, respectively; s the longitudinal coordinate; and $k_{0,x,y}$, $k_{x,y}$ are the phase advances per focusing cell without and with space charge, respectively. φ_1 and φ_2 ($\varphi_1 > \varphi_2$) denote the phase shifts of the second order even modes (i.e., the two envelope modes), while ψ_1, ψ_2 ($\psi_1 > \psi_2$) are the phase shifts of the two second order odd modes, respectively.

---

[1] The second order modes are also known as "skew modes".

[2] Written as "Chernin equations" in the following, for more details see Ref. [5].

5.1 Second-Moment Oscillations

We first consider a lattice including an external skew focusing force. Following Chernin, the evolution of second moments of the beam can be written in matrix form [5]

$$\boldsymbol{\Sigma' = M\Sigma + (M\Sigma)^T}, \tag{5.1}$$

with

$$M = \begin{pmatrix} 0 & 1 & 0 & 0 \\ -\kappa_x(s) & 0 & -q_{xy}(s) & 0 \\ 0 & 0 & 0 & 1 \\ -q_{xy}(s) & 0 & -\kappa_y(s) & 0 \end{pmatrix}. \tag{5.2}$$

Here, " $'$ " denotes the derivative with respect to s, the superscript "T" means the transposed matrix, Σ represents the 4×4 matrix of the second moments, with elements Σ_{ij} defined by $\Sigma_{ij} \equiv \langle v_i v_j \rangle - \langle v_i \rangle \langle v_j \rangle$, where the averages are taken over the phase space variables and the subscripts i, j run from 1 to 4 representing x, x', y, y'. $\kappa_x = \kappa_{x0} - \Delta\kappa_x$, $\kappa_y = \kappa_{y0} - \Delta\kappa_y$ and $q_{xy} = q_{xy,0} - \Delta q_{xy}$, with $\kappa_{x0} = (1/B\varrho)(\partial B_y/\partial x)$, $\kappa_{y0} = -(1/B\varrho)(\partial B_x/\partial y)$ the external focusing gradients and $q_{xy0} = (1/B\varrho)(\partial B_x/\partial x)$ the external linear coupling, ($B\varrho$ is the magnetic rigidity) and $\Delta\kappa_x$, $\Delta\kappa_y$ and Δq_{xy} the space-charge induced shifts, defined by

$$\begin{gathered} \Delta\kappa_x = \frac{K_{\text{sc}}}{2} \frac{S_y}{S_0(S_x + S_y)}, \qquad \Delta\kappa_y = \frac{K_{\text{sc}}}{2} \frac{S_x}{S_0(S_x + S_y)}, \\ \Delta q_{xy} = \frac{K_{\text{sc}}}{2} \frac{\Sigma_{13}}{S_0(S_x + S_y)}, \end{gathered} \tag{5.3}$$

using

$$\begin{gathered} S_0 = \sqrt{\Sigma_{11}\Sigma_{33} - \Sigma_{13}^2}, \\ S_x = \Sigma_{11} + S_0, \qquad S_y = \Sigma_{33} + S_0. \end{gathered} \tag{5.4}$$

Here K_{sc} is the space charge perveance parameter defined in Eqs. 3.6. Clearly, Σ_{13}, Σ_{14}, Σ_{23} and Σ_{24} denote the coupling moments between x and y. Eq. 5.1 can be written in a concise form [77]

$$\boldsymbol{\Sigma' = G(\Sigma(s), s)}. \tag{5.5}$$

For a lattice with constant focusing and coupling, Eq. 5.5 can be readily solved with a given initial generalized emittance [78]. For a lattice with alternating-gradient focusing, matched solutions $\Sigma_0(s)$ can be obtained numerically from Eq. 5.5 with periodic conditions $\Sigma_0(s) = \Sigma_0(s + L)$, where L is the periodicity.

Now let us assume a slightly mismatched case, where the second moments can be written as $\Sigma(s) = \Sigma_0(s) + \Sigma_p(s)$[3]. After Taylor expanding and keeping only first order terms we have from Eq. 5.5

$$\boldsymbol{\Sigma}' = (\boldsymbol{\Sigma}_0 + \boldsymbol{\Sigma}_p)' = \boldsymbol{G}(\boldsymbol{\Sigma}_0) + \boldsymbol{J}(\boldsymbol{\Sigma}_p), \tag{5.6}$$

which can be divided into two parts

$$\boldsymbol{\Sigma}_0{}' = \boldsymbol{G}(\boldsymbol{\Sigma}_0), \qquad \boldsymbol{\Sigma}_p' = \boldsymbol{J}(\boldsymbol{\Sigma}_0)\boldsymbol{\Sigma}_p. \tag{5.7}$$

Here **J** represents the Jacobian matrix of **G** with elements $J_{k,l} = \partial G_k(\Sigma_l)/\partial \Sigma_l$, with k, l run from 1 to 10 along the possible combinations of the second order moments Σ_{ij}.

After several steps of derivations[4], the complete set of second-moment oscillation can be written as two parts, with the first part

$$\begin{aligned}
\Sigma_{11}^{p}{}' &= 2\Sigma_{12}^{p},\\
\Sigma_{12}^{p}{}' &= \Big(\frac{\partial G_2}{\partial \Sigma_{11}}\Big)_0\Sigma_{11}^{p} + \Big(\frac{\partial G_2}{\partial \Sigma_{12}}\Big)_0\Sigma_{12}^{p} + \Big(\frac{\partial G_2}{\partial \Sigma_{33}}\Big)_0\Sigma_{33}^{p},\\
\Sigma_{33}^{p}{}' &= 2\Sigma_{34}^{p},\\
\Sigma_{34}^{p}{}' &= \Big(\frac{\partial G_8}{\partial \Sigma_{11}}\Big)_0\Sigma_{11}^{p} + \Big(\frac{\partial G_8}{\partial \Sigma_{33}}\Big)_0\Sigma_{33}^{p} + \Big(\frac{\partial G_8}{\partial \Sigma_{34}}\Big)_0\Sigma_{34}^{p},
\end{aligned} \tag{5.8}$$

which are recognized as envelope oscillations, and the second part

$$\begin{aligned}
\Sigma_{13}^{p}{}' &= \Sigma_{14}^{p} + \Sigma_{23}^{p},\\
\Sigma_{14}^{p}{}' &= \Big(\frac{\partial G_4}{\partial \Sigma_{13}}\Big)_0\Sigma_{13}^{p} + \Sigma_{24}^{p},\\
\Sigma_{23}^{p}{}' &= \Big(\frac{\partial G_5}{\partial \Sigma_{13}}\Big)_0\Sigma_{13}^{p} + \Sigma_{24}^{p},\\
\Sigma_{24}^{p}{}' &= \Big(\frac{\partial G_6}{\partial \Sigma_{13}}\Big)_0\Sigma_{13}^{p} + \Big(\frac{\partial G_6}{\partial \Sigma_{14}}\Big)_0\Sigma_{14}^{p} + \Big(\frac{\partial G_6}{\partial \Sigma_{23}}\Big)_0\Sigma_{23}^{p}.
\end{aligned} \tag{5.9}$$

which is for the equations of second order odd modes. Here the cofficients in Eqs. 5.8 and Eqs. 5.9 are partial derivatives of the Jacobian matrix **G** with respect to the second moments[5]. With matched solutions of the second moments of beams from Eq. 5.1, the abvoe two equations are used to calcualte the second order modes.

---

[3] The subscript “0” and “p” denotes respectively the matched solution and a small perturbation of the matched solution.

[4] For mathmatical details see Appendix D.

[5] Appendix G lists each value of the derivatives for the case without external skew focusing forces.

5.2 Tilting Instability in Constant Focusing

In this section, we will investigate the instability induced by the odd modes for intense beams transported in a constant focusing channel[6], by using the set of oscillation equations in Eq. 5.8 and Eq. 5.9. For constant focusing Eqs. 5.9 take the form

$$\begin{aligned}\frac{\mathrm{d}^2}{\mathrm{d}s^2}\Sigma^p_{13} &= a_1\Sigma^p_{13} + a_2\Sigma^p_{24},\\ \frac{\mathrm{d}^2}{\mathrm{d}s^2}\Sigma^p_{24} &= a_3\Sigma^p_{13} + a_4\Sigma^p_{24},\end{aligned} \tag{5.10}$$

with the coefficients

$$\begin{aligned}a_1 &= \Big[\frac{\partial q_{xy}}{\partial \Sigma_{13}}(\Sigma_{11}+\Sigma_{33}) - (k_x + k_y)\Big]_0,\\ a_2 &= 2,\\ a_3 &= \Big[-\frac{\partial q_{xy}}{\partial \Sigma_{13}}(k_x\Sigma_{11} + k_y\Sigma_{33}) + 2k_xk_y\Big]_0,\\ a_4 &= -(k_x + k_y)_0.\end{aligned} \tag{5.11}$$

The two odd modes with the corresponding phase shifts $\psi_{1,2}$ can be readily decoupled and obtained from Eq. 5.10. For a round beam under a symmetric constant focusing with $k_{0,x} = k_{0,y} = k_0$, the results of odd modes $\psi_{1,2}$ calculated numerically from Eq. 5.10, along with the even ones $\varphi_{1,2}$ from Eq. 5.8, are shown in Fig. 5.1 for different beam currents in units of the space charge tune depression $\eta_x \equiv (k_{0,x} - k_x)/k_{0,x}$. It can be seen that due to the axial symmetry the fast branch of the odd modes ψ_1 is always identical with the slow branch of the even mode, while the slow odd mode ψ_2 is zero (not shown in the plot). This is in agreement with the results obtained from Vlasov equation for the round beam case in Ref. [1].

The tilting instability is induced by a sufficiently large asymmetry of the transverse focusing, where the transverse beam shape becomes elliptical, the slow branch of the odd modes become nonzero. An example with $k_{0,x} = 60^\circ$ and $k_{0,y} = 66.7^\circ$ and $\epsilon_x/\epsilon_y = 2$ is shown in Fig. 5.2. It is seen that the slow odd mode ψ_2 is close to $k_y - k_x$ for increasing beam current up to the point, where both become zero. In this region the slow odd mode is called a "difference mode". To the right side of this point in Fig. 5.2, $(\psi_2)^2$ becomes negative, hence unstable, and the imaginary part is shown. This "tilting instability" is discussed in detail further below. For the fast odd mode $\psi_1 \geq k_x + k_y$, hence this mode can be called "sum mode".

PIC simulations using PyORBIT [70] are performed to compare with results from this analytical framework. To this end 50 000 macro particles are tracked over 1000 periodic FODO cells, and a Fourier analysis is employed on the coupling moment $\langle xy\rangle$ at various

---

[6] It can be shown that for constant focusing, the even modes are always stable, see Ref. [1].

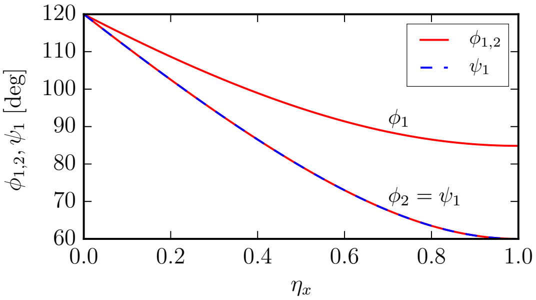

Figure 5.1.: Round beam case, $k_{0,x} = k_{0,y} = k_0 = 60°$: Phase shifts $\varphi_{1,2}$,ψ_1 versus tune depression in x in a constant focusing channel.

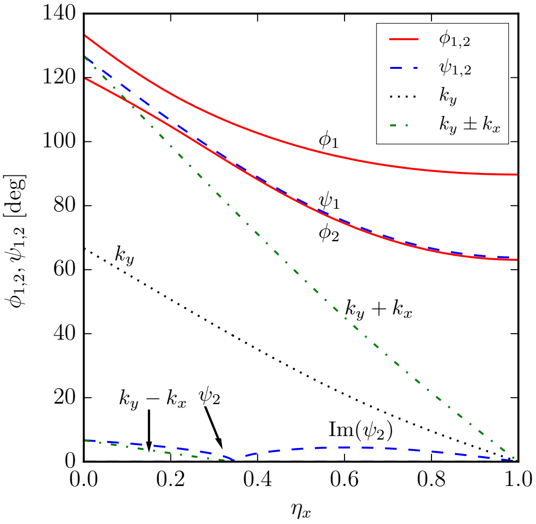

Figure 5.2.: Elliptical beam case, $k_{0,x} = 60°$, $k_{0,y} = 66.7°$ and $\epsilon_x / \epsilon_y = 2$: Phase shifts of coherent even modes $\varphi_{1,2}$ and odd modes $\psi_{1,2}$ versus tune depression in x in a constant focusing channel.

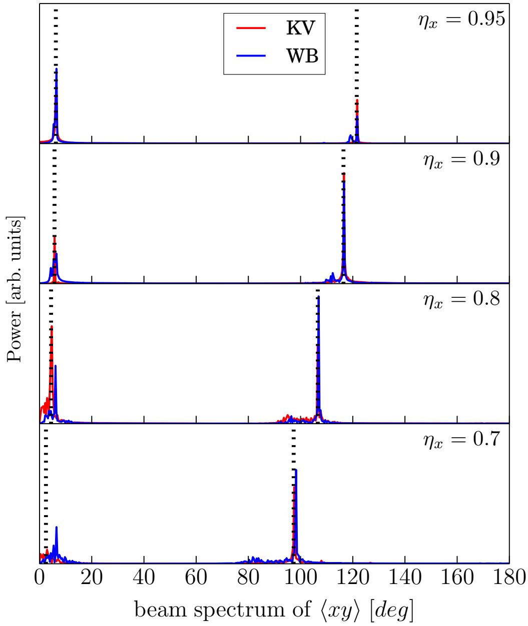

Figure 5.3.: Elliptical beam case, $k_{0,x} = 60°$, $k_{0,y} = 66.7°$: Beam spectrum of $\langle xy \rangle$ from PIC simulation of KV distribution (red solid) and waterbag (WB) distribution (blue solid), compared with the analytical results (dotted black lines) of phase shifts of second order odd sum and difference modes $\psi_{1,2}$, for different values of η_x in a constant focusing channel.

beam intensities in terms of η_x. As shown in Fig. 5.3, the beam spectra of $\langle xy \rangle$ for a K-V and a waterbag distribution agree well with the results of the second order odd mode phase advances $\psi_{1,2}$ in Fig. 5.2 obtained from the theoretical approach of Eq. 5.10.

Note the minor bump to the l.h.s. of the sum mode, which has a downwards shift from ψ_1 increasing roughly linearly with space charge. This might be associated with single particle tunes and numerical noise of the PIC code.

An interesting property of the second order odd modes shown in Ref. [1] is found for $\epsilon_x \neq \epsilon_y$ and sufficiently large anisotropy. With an external focusing stronger in y than in x (or vice versa), but reverted due to space charge, the beam is subject to the tilting instability with periodical exchange of emittances as indicated above in Fig. 5.2. In this case the solution of Eq. 5.9 shows that the squared phase shift of the difference mode becomes negative, $(\psi_2)^2 < 0$, indicating instability. As an example, Fig. 5.4 illustrates the imaginary part of ψ_2 for constant $k_y/k_{0,y} = 0.8$ and $\varepsilon_x/\varepsilon_y = 2$, as a function of the betatron tune ratio, hence the stop band of the tilting instability. We find that the

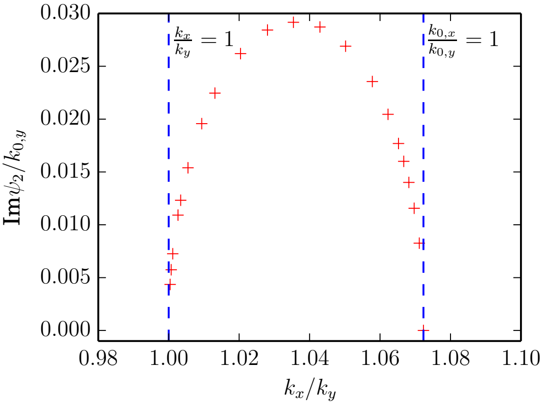

Figure 5.4.: Growth rate of difference odd mode (normalized) for constant $k_y/k_{0,y} = 0.8$ and $\varepsilon_x/\varepsilon_y = 2$ as a function of the betatron tune ratio, indicating the tilting instability in a constant focusing channel.

values of growth rates as well as the width of the stop band are in excellent agreement with the curve of the second order odd mode in Fig. 4 in Ref. [24], which is based on the linearized Vlasov-Poisson approach - thus confirming the equivalence of these two models. Note that following Ref. [24] the tilting instability is accompanied by a - usually - dominant fourth order resonance in an adjacent stop band, which is the well-known Montague instability (see also Ref. [75]).

5.3 Sum Envelope Instabilities in Periodic Focusing

In chapter 4 we introduced the well-known envelope instability in periodic focusing induced by the unstable second order even modes. In this section, we will show that besides the envelope instability, the “sum envelope beam instability” exists in a periodic, unsymmetrical focusing channel, which is a coupling effect between x and y plane. Analogous to the mechanism of the well-known envelope instability, the sum envelope beam instability is a resonant phenomenon of the second order modes, and can be classified into two essentially distinct modes [22]

- *Coupled even mode sum instability.* Based on space charge coupling between even envelope modes and their parametric resonance with the lattice, the stop band of coupled even modes is theoretically illustrated in Figs. 1, 2 of Ref. [22].

- *Skew (odd) mode sum instability.* This instability is based on parametric resonance of the odd sum mode as shown by the PIC simulation in Fig. 3 of Ref. [22].

In the following, we explore the theoretical mechanisms of both modes by using the formalism of Eqs. 5.9. Similar to the treatment of the usual envelope instabilities [4, 17],

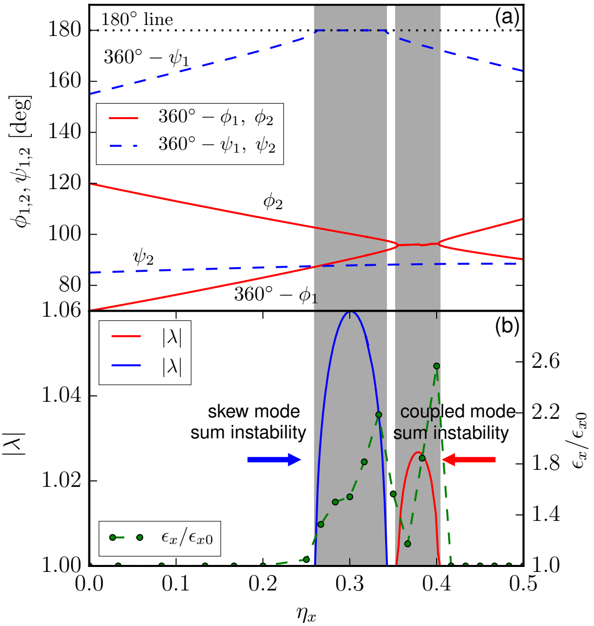

Figure 5.5.: Perturbation theory results for both types of sum envelope instabilities in a periodic focusing system. Upper plot (a): Phase shifts of $\varphi_{1,2}$, $\psi_{1,2}$ verses tune depression in x; Lower plot (b): Corresponding growth factors per lattice period (continuous lines), and comparison with final emittance growth factors (dashed lines, normalized to initial values) for PIC simulation of same cases.

the four eigenvalues can be calculated by integrating Eqs. 5.8 and Eqs. 5.9: $\zeta_{m+1} = M\zeta_m$, where M is the map for the perturbation vector $\zeta = (\Sigma_{11}^p, \Sigma_{12}^p, \Sigma_{33}^p, \Sigma_{34}^p, \Sigma_{13}^p, \Sigma_{14}^p, \Sigma_{23}^p, \Sigma_{24}^p)$ over one periodic cell. The eight eigenvalues of M, $\lambda_i = |\lambda_i| e^{i\varphi_i} (i = 1, 2, ...8)$, exist only as reciprocal or as conjugate. One of the moduli larger than unity can be used as growth factor per lattice period of the sum envelope instabilities.

The example in Fig. 5.5 shows the second order even and odd modes as a function of beam intensity in an unsymmetrical FODO lattice with $k_{0,x} = 60°$ and $k_{0,y} = 145°$. For convenience of plotting, in Fig. 5.5(a) the curves of $360° - \psi_1$ and $360° - \varphi_1$ are plotted instead of ψ_1 and φ_1. In the region $k_x = 44.2°$ to $39.6°$ (corresponding to $\eta_x = 0.737$ to 0.66) one branch of the odd mode is locked to 180°, with the corresponding eigenvalue larger than unity, indicating the *skew mode sum instability*. It is characterized by the parametric resonance between the focusing structure and the odd sum mode branch ψ_1. Further increasing the beam current, φ_2 and $360° - \varphi_1$ (the curves in red color)

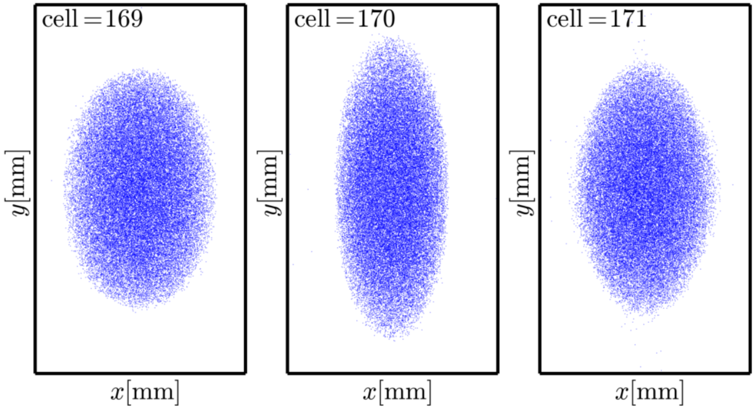

Figure 5.6.: Real space distributions for three consecutive cells at early stage of coupled even mode sum instability with initial $\eta_x = 0.6$.

become confluent, i.e., $\varphi_1 + \varphi_2 = 360°$, which means the two even modes are coupled and the *coupled mode sum instability* is excited. Note that the width of the stop band of the skew mode sum instability is wider than the one of the coupled mode sum instability, and both stop bands are only separated by a thin gap.

The theory of second-moment oscilltion results abover provide no information on rms emittance growth. This requires PIC simulation with results shown by the dashed (green) lines in Fig. 5.5(b). The simulation results show ϵ_x/ϵ_{x0} after 500 focusing periods, at which time the emittance growth caused by the instability is already saturated. The initial particle distribution is chosen as rms-matched transverse waterbag. Two "sawtooth" like emittance growth phenomena are observed, with a width that agrees well with the stop bands obtained from perturbation theory stop bands. The shape of a "sawtooth" is caused by the self-detuning process, which is a remarkable feature of the second order coherent instabilities [20, 4]. Note that the saturated PIC emittance growth factor for the coupled mode sum instability is larger than that of the skew mode sum instability, whereas the mode amplitude growth factor (per period) of the latter exceeds that of the former. Figs. 5.6 and 5.7 show the PIC simulation results in real space projections at three consecutive periods at early stages of the two modes of instability. In the case of the coupled even mode sum instability the beam shows a coupled modulation of envelopes in x and y. In contrast, the beam performs skew "swinging" in real space as a characteristic of the skew mode sum instability.

Fig. 5.8 shows the change of phase shifts of the second order even and odd modes (in solid and dashed lines, respectively), with fixed $k_{0,y} = 145°$ and varying $k_{0,x} = 40°, 50°, 60°$ and $70°$. The curves of $360° - \psi_1$ and $360° - \varphi_1$ are plotted instead of ψ_1 and φ_1. Two main properties can be observed and discussed as follows: Firstly, with $k_{0,x}$ increasing from 40° to 70°, the sum instability starts to appear (in the case of

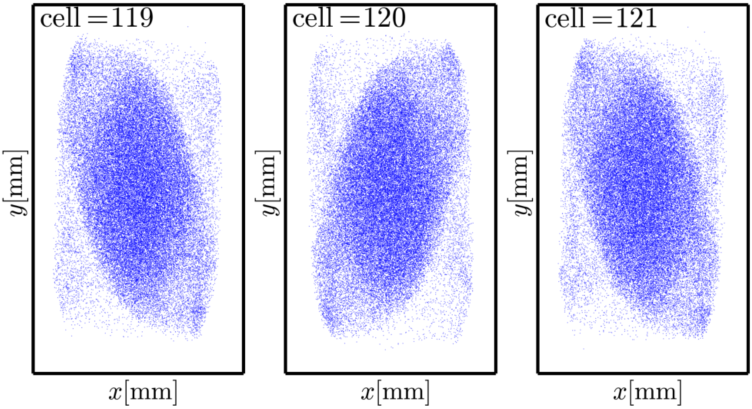

Figure 5.7.: Real space distribution for three representative consecutive cells at early stage of skew mode sum instability with initial $\eta_x = 0.67$.

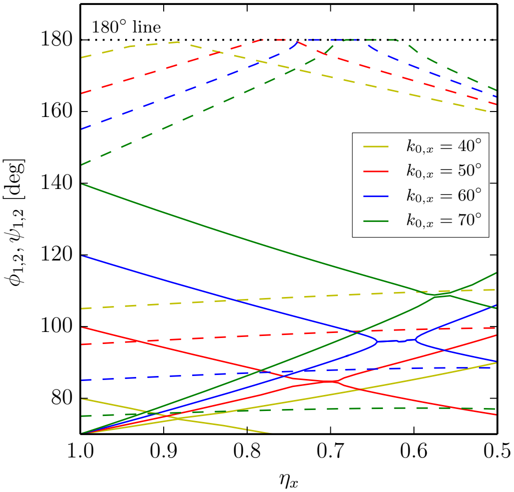

Figure 5.8.: Phase shifts of $\varphi_{1,2}$, $\psi_{1,2}$ verses tune depression in x with fixed $k_{0,y} = 145°$ and varying $k_{0,x} = 40°$ (yellow), $50°$ (red), $60°$ (blue) and $70°$ (green).

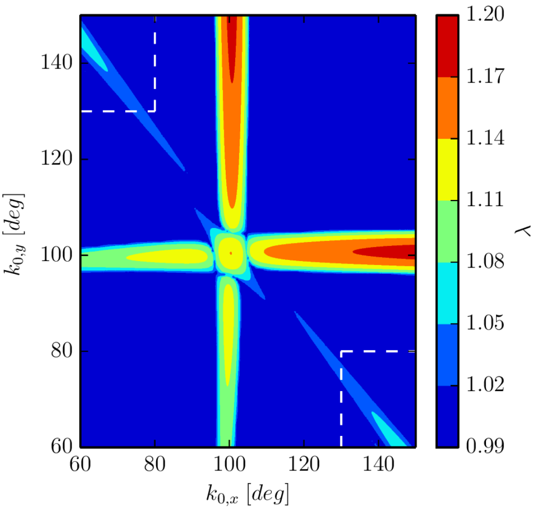

Figure 5.9.: Tune diagram as scan of growth factor λ obtained from perturbation matrix.

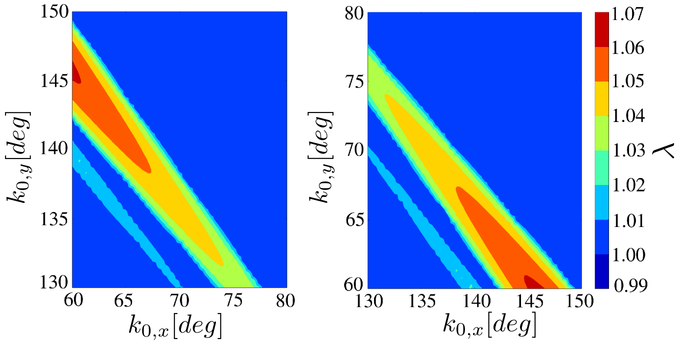

Figure 5.10.: Enlarged scans of the two opposite corner zones in Fig. 5.9.

$k_{0,x} = 50°$) and then becomes enhanced (in the case of $k_{0,x} = 60°$); finally it becomes very weak ($k_{0,x} = 70°$). Secondly, with $k_{0,x}$ getting larger, the stop band moves towards the direction of stronger space charge.

In order to present an overview on the appearance of the two kinds of sum envelope instabilities, with the corresponding two stop bands, a tune diagram of perturbation theory eigenvalues λ is worked out by scanning $k_{0,x}$ and $k_{0,y}$ from 60° to 150° based on integrating Eqs. 5.8 and Eqs. 5.9, as shown in Fig. 5.9. Enlargements of the two diagonal blocks in Fig. 5.9 within the region of $k_{0,x}, k_{0,y}$ from 130° to 150° and 60° to 80° (marked by white dashed lines in Fig. 5.9) are shown in Fig. 5.10. The horizontal and vertical stop bands mark the 90° even mode envelope instabilities, and the diagonal with negative slope denotes the stop band of the coupled even mode sum envelope instability: The narrow one is representing the coupled even mode sum instability, and the broader one the skew mode sum instability.

6 Space-Charge Dominated Beam Dynamics in Synchrotrons

As introduced in Chapter 1, the effect of dispersion is one of the most important characteristic for the motion of charged particles in a beam travelling in a synchrotron. The aim of this chapter is dedicated to a detailed study of space-chagre dominated beam dynamics in synchrotrons, where the dispersion and space charge have a combined effect on the beam. The envelope theory introduced in chapter 3 is generalized to the case in which the role of dispersion is fully taken into for matched beam motion and mismatch oscillations. In the presence of space charge and dispersion, the mismatch oscillation could lead to the dispersion-induced instability [4], characterized by the coherent dispersion mode, which will be discussed in detail.

The chapter is organized as follows. We introduced the generalized envelope equations including dispersion in section 6.1, as well as some relevant concepts. The beam dynamics in matched and mismatched cases in the presence of both space charge and dispersion are discussed respectively in section 6.2 and 6.3. In section 6.4, the beam instabilities with space charge and dispersion, including the dispersion-induced instability and the dispersion-modified envelope instability are shown by both numerical approach and PIC simulations.

6.1 The Generalized Envelope Equations

6.1.1 Space-Charge Modified Dispersion

Consider a coasting beam transported in a periodic focusing channel with dipoles[1]. For simplicity, here we ignore any imperfection of the periodic channel and any nonlinear effect due to external focusing, as well as all the chromatic terms. The Hamiltonian of such a system can be expressed as

$$H = \frac{1}{2}(p_x^2 + p_y^2) + \frac{\kappa_{x0}(s)}{2}x^2 + \frac{\kappa_{y0}(s)}{2}y^2 + \frac{m^2c^4}{E_0^2}\delta^2 - \frac{x}{\varrho(s)}\delta + V_{\mathrm{sc}}(x,y,s), \tag{6.1}$$

where s is the longitudinal coordinate; $\kappa_{x0}(s), \kappa_{y0}(s)$ denote the focusing gradients; $\varrho(s)$ the radius of curvature; $\delta = (p - p_0)/p_0$ the fractional momentum deviation from the design momentum p_0 with E_0 being the corresponding energy and V_{sc} the space charge

---

[1] This focusing channel can be seen as a periodic cell in a synchrotron.

potential. Following the framework in Ref. [29, 2] (written as "V-R and L-O theory" in the following), with a series of derivation of coordiante transformation and second moment distribution, the space-charge-modified dispersion function can be obtained[2]

$$\frac{\mathrm{d}^2 D_x}{\mathrm{d}s^2} + \left[\kappa_{x0}(s) - \frac{K_{\mathrm{sc}}}{2X(X+Y)}\right] D_x = \frac{1}{\varrho(s)}, \tag{6.2}$$

with the corresponding rms envelope equations in the presence of both dispersion and space charge:

$$\frac{\mathrm{d}^2 \sigma_x}{\mathrm{d}s^2} + \left[\kappa_{x0}(s) - \frac{K_{\mathrm{sc}}}{2X(X+Y)}\right] \sigma_x - \frac{\varepsilon_{dx}^2}{\sigma_x^3} = 0, \tag{6.3a}$$

$$\frac{\mathrm{d}^2 \sigma_y}{\mathrm{d}s^2} + \left[\kappa_{y0}(s) - \frac{K_{\mathrm{sc}}}{2Y(X+Y)}\right] \sigma_y - \frac{\varepsilon_{dy}^2}{\sigma_y^3} = 0. \tag{6.3b}$$

Here, the second moments X and Y are the total transverse rms beam size including dispersion; σ_x and σ_y are the betatron beam size with the relation

$$X = \sqrt{\sigma_x^2 + \sigma_\delta^2 D_x^2}, \quad Y = \sigma_y, \tag{6.4}$$

where σ_δ is the rms momentum spread. It can be seen that in the presence of disperion[3], the rms transverse beam size $X(s)$ contains two independent contributions: *dispersion* beam size $\sigma_\delta D_x(s)$ and the *betatron* beam size $\sigma_x(s)$. The ε_{dx} is the generalized emittance introduced in V-R and L-O theory, and are invariant[4] with dispersion.

Some main features of the generalized envelope equation including dispersion of Eq. 6.2 and Eqs. 6.3 are discussed as following.

1. Compared to the two dimensional envelope equations in Eq. 3.19, the generalized envelope equations is three dimensional. The beam motion in the horizonal and vertical plane are coupled with space charge. Moreover, in the horizontal plane, the beam motion can be divided into the motion of σ_x and the motion of dispersion D_x.

2. It can be seen from Eq. 6.4 that the dispersion can enlarge the transverse beam size and thus weaken the space charge. With a given beam intensity, the space charge is in inverse proportion to the dispersion. Fig. 6.1 shows the variation in space charge (in unit of space-charge depression), with the variation of dispersion (represented by rms momentum spread). Both η_x and η_y are decreasing as σ_δ

---

[2] For details of the derivation, see Appendix E.

[3] Here, we assume a horizontal dispersion, and thus $Y = \sigma_y$ in vertical direction

[4] The invariance of the generalized emittances are under the assumption of the beam with symmetrical elliptical transverse shape, which is approximately valid for general cases.

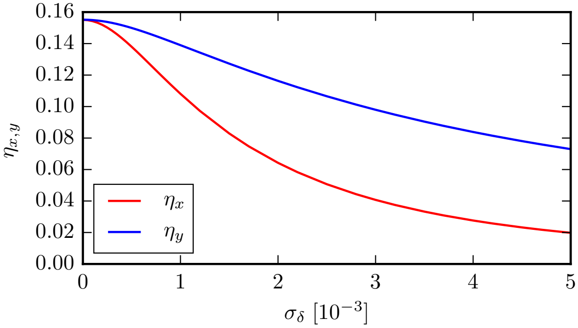

Figure 6.1.: An example of the space-charge depression $\eta_{x,y}$ as the functions of rms momentum spread σ_δ for a fixed beam intensity.

increasing. The correlation between space charge and dispersion will be further discussed in subsection 6.2.2.

3. Analogy to the mathcing of the rms beam sizes $\sigma_{x,y}$ as discussed in section 3.2, a set of matched solution $\{\sigma_{x0}, \sigma_{y0}, D_{x0}\}$ can be found from Eq. 6.2 and Eqs. 6.3. The space-charge-modified dispersion is dependent on space charge and thus on the rms betatron beam size σ_x and σ_y, and the matched solution defines the unique space-charge-modified dispersion. This problem of dispersion matching will be analyzed in detail in subsection 6.3.1.

4. The space-charge-modified dispersion defined in Eq. 6.2 must be distinguished with the concept of dispersion of Eq. 2.22 derived from the single particle dynamics in Chapter 2: The former is the quantity which characterize the effect of dispersion on the motion of an intense beam, while the latter is a parameter for accelerators, and depends on the configaration of the accelerator.

6.1.2 Dispersion Ratio

Since the total rms transverse beam size $X(s)$ contains two independent contributions: dispersion beam size $\sigma_\delta D_x(s)$ and betatron beam size $\sigma_x(s)$, it is convenient to introduce a "dispersion ratio" $\cos\vartheta$, and the corresponding "betatron ratio" $\sin\vartheta$ to estimate the extent of the beam motion being affected by space-charge-modified dispersion, defined by

$$\cos\vartheta = \sigma_\delta D_x(s)/X(s) \tag{6.5}$$

and

$$\sin\vartheta = \sigma_x(s)/X(s), \tag{6.6}$$

respectively, and $0 < \vartheta < \pi/2$. Clearly, a larger dispersion ratio means larger dispersion effect. The concept of dispersion ratio defined here will be employed to analyze the dispersion properties in the next section.

6.2 Matched Beam Motion

In this section and next section, we will discuss the beam motion, including matched and mismatched, in the presence of both dispersion and space charge, which is the case for intense beams travelling in circular accelerators. This section deals with the matched beam motion, based on the 3-D beam envelope model in Eq. 6.2 and Eqs. 6.3. Some main characteristic of the beam dynamics will be shown by analyzing a beam transported in constant focusing channel[5]. In the next section the mismatched motion is described by performing perturbation on the 3-D beam envelope model.

6.2.1 Constant Focusing with Dispersion

Let us start with a solenoid with its length L inside a dipole with the radius of curvature ϱ_0. Such a transporting channel can be seen as a Constant Focusing system with Dispersion (CFD) and can be used as good smooth approximation [54] of a realistic Alternating Gradient focusing periodic structure with Dispersion (AGD) in circular machines. Clearly, for the CFD case, both of external focusing force and dispersion function are constant. For simplicity, here we further introduce the “symmetrical CFD" with assuming that the external focusing force is axisymmetric in x and y: $\kappa_{x0}(s) = \kappa_{y0}(s) = \kappa_0$. Note that the focusing contribution from the dipole is already included in κ_0. Under these assumptions, for the matched case, envelope equations of Eq. 6.2 and Eqs. 6.3 take the algebraic form

$$\begin{gathered} \kappa_x D_{x0} = \frac{1}{\varrho_0}, \\ \kappa_x \sigma_{x0} = \frac{\varepsilon_{dx}^2}{\sigma_{x0}^3}, \qquad \kappa_y \sigma_{y0} = \frac{\varepsilon_{dy}^2}{\sigma_{y0}^3}, \end{gathered} \tag{6.7}$$

in which

$$\kappa_x = \kappa_0 - \frac{K_{\mathrm{sc}}}{2X_0(X_0+Y_0)}, \qquad \kappa_y = \kappa_0 - \frac{K_{\mathrm{sc}}}{2Y_0(X_0+Y_0)} \tag{6.8}$$

are respectively the space charge depressed external focusing force in x and y with $X_0 = \sqrt{\sigma_{x0}^2 + D_x^2\sigma_\delta^2}$ and $Y_0 = \sigma_{y0}$. The subscript “0” represents the matched case. For a given ε_{dx} and ε_{dy}, the matched solution $\{\sigma_{x0}, \sigma_{y0}, D_{x0}\}$ can be readily solved. Note that while in the symmetric CFD case $\kappa_{x0} = \kappa_{y0} = \kappa_0$, we have $\kappa_x \neq \kappa_y$ since $X_0 \neq Y_0$ because of

---

[5] See the method of “smooth approximation” in Chapter 3

dispersion. One can easily find the beta functions β_0, $\beta_{x,y}$, dispersion functions D_0, D_{x0}, and the tune Q_0, $Q_{x,y}$, in both cases without and with space charge effect, respectively:

$$\begin{aligned} \beta_0 &= \frac{L}{\kappa_0}, \quad \beta_{x,y} = \frac{L}{\kappa_{x,y}}, \\ D_0 &= \frac{1}{\varrho_0 \kappa_0}, \quad D_{x0} = \frac{1}{\varrho_0 \kappa_x}, \\ k_0 &= \sqrt{\kappa_0} L, \quad k_{x,y} = \sqrt{\kappa_{x,y}} L, \\ Q_0 &= \frac{k_0}{2\pi}, \quad Q_{x,y} = \frac{k_{x,y}}{2\pi}. \end{aligned} \tag{6.9}$$

In the matched case, both of the total emittance and generalized emittance in Eq. F.8 are constant and has the simple relation:

$$\varepsilon_{dx} = \varepsilon_x \sin\vartheta, \tag{6.10}$$

in which $\sin\vartheta$ is the betatron ratio introduced in Eq. 6.6.

6.2.2 Dispersion Properties

In the following we use the “dispersion ratio" defined in Eq. 6.5 to show space-charge-modified dispersion properties, by using an example of symmetric CFD with the main parameters listed in Table 6.1, which are typical for SIS-18 at GSI. Space charge tune depressions $\eta_{x,y} \equiv (k_{0,x,y} - k_{x,y})/k_{0,x,y}$, the ratio of matched betatron rms beam size σ_{x0}/σ_{y0}, the matched total rms beam size X_0/Y_0 and betatron ratio $\sin\vartheta$ are numerical calculated and plotted with increasing beam intensity for two representative cases: $\kappa_0 = 60°$ and $\kappa_0 = 90°$, as shown in Fig. 6.2.

Two main properties of the influence of the dispersion on beam coherent motion are discussed as follows. Firstly, in the left plot of Fig. 6.2, with beam current increasing, η_y increases much faster than η_x since the dispersion effect breaks the symmetric property of the symmetrical CFD structure and weakens the space charge force in x (the solid lines $\eta_y > \eta_x$). Consequently, betatron beam size σ_x is much focused and smaller than σ_y (the dashed lines $\sigma_{x0}/\sigma_{y0} < 1$), and in the space charge limit ($\eta_x \to 1$), σ_{x0}/σ_{y0} tends to zero. Secondly, in the right plot in Fig. 6.2, with beam current increasing, the dispersion ratio $\sin\vartheta$ only decreases while the total rms beam size ratio X_0/Y_0 increases first and then decreases. Compared with the curve of σ_{x0}/σ_{y0} (dashed line in the top plot) and with the correlation $X_0^2 = \sigma_{x0}^2 + \sigma_\delta^2 D_{x0}^2$, $Y_0^2 = \sigma_{y0}^2$, it is found that X/Y increases due to the dispersion contribution $\sigma_\delta D_{x0}$. With beam current increasing, what the beam experiences can be divided into two stages: in the first stage, the space-charge-modified dispersion D_{x0} increases much faster than σ_{y0}, leading to $X_0 > Y_0$ and increased X/Y; In the second stage, with beam current continuing to increase, X_0/Y_0 starts to decrease since σ_{y0} increases faster due to a stronger space charge in y. The first stage can be

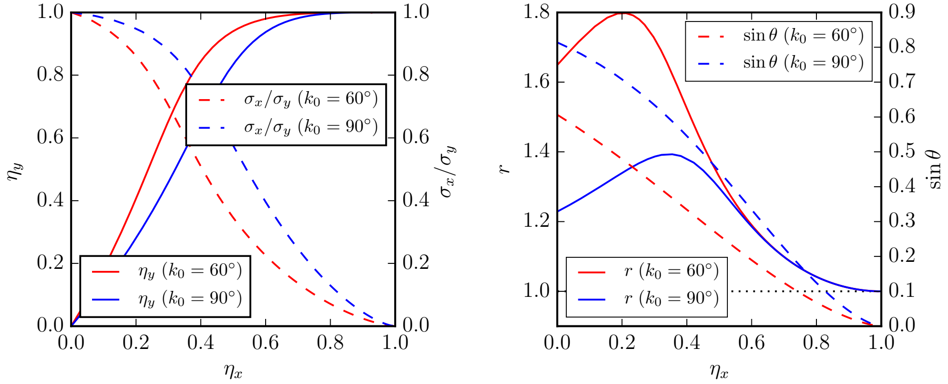

Figure 6.2.: Left plot: tune depression in y (solid line) and betatron beam size ratio σ_{x0}/σ_{y0} (dashed line) versus beam current (in the unit of η_x). Right plot: total beam size ratio X_0/Y_0 (solid line) and dispersion ratio (dashed line) versus beam current (in the unit of η_x).

named "dispersion dominated stage", characterized by the fast increase of space-charge-modified dispersion; the second stage can be named "space charge dominated stage", where X_0 and Y_0 tend to be equal in the extreme limit of space charge.

Table 6.1.: Main parameters of the example CFD

Parameters [unit]	Symbols	Values
Length of the CFD [m]	L	18.0
Radius of curvature [m]	ϱ_0	10.0
Generalized emittance on x [mm mrad]	ε_{dy}	10.0
Generalized emittance on y [mm mrad]	ε_{dy}	10.0
rms momentum spread	σ_δ	0.002

6.2.3 Scaling Law of Dispersion Shift

The extend of the effect of space charge acted on dispersion functions ("dispersion shift") can be evaluated by using the CFD case. In particular, a scaling law can be derived: performing Taylor expansion of D_x around the matched solution D_{x0} in Eq. 6.7, keeping only the linear term, we find

$$\Delta D_x \approx -\frac{\Delta\kappa_x}{\kappa_x^2 \varrho_0}, \tag{6.11}$$

where $\Delta\kappa_x = \kappa_x - \kappa_0$ is the space-charge shift of focusing gradient, and $\Delta D_x = D_x - D_{x0}$ is the space-charge shift of dispersion. Similarly, from Eq. 6.9 the linearized formula of space-charge shift of phase advance reads

$$\Delta k_x \approx \frac{\Delta\kappa_x L^2}{2k_x}. \tag{6.12}$$

The space charge modified dispersion as a function of Δk_x can be obtained with the combination of Eq. 6.11 and Eq. 6.12:

$$\Delta D_x = -\frac{2k_x \Delta k_x}{L^2 \varrho_0 \kappa_x^2}, \tag{6.13}$$

or

$$\Delta D_x = -\frac{8\pi^2 Q_x \Delta Q_x}{L^2 \varrho_0 \kappa_x^2}. \tag{6.14}$$

Here Q_x and ΔQ_x is the tune and tune shift in x with space charge, respectively. It can be seen from Eq. 6.13 and Eq. 6.14 that dispersion function will increase under the effect of space charge, i.e., $\Delta D_x > 0$. The minus symbol “-" in Eq. 6.13 and Eq. 6.14 denotes the dispersion shift has an inverse correlation with the tune shift ΔQ_x. The effectiveness of the two equations will be shown in the next section.

6.2.4 Alternating Gradient Focusing with Dispersion

For a more realistic case, we consider an example alternating gradient focusing channel with dispersion (AGD), with periodic $\kappa_{x0}(s)$, $\kappa_{y0}(s)$ and $\varrho(s)$. Specifically, we compose an example FODO lattice with dipoles formed by the sequence: $\{\frac{1}{2}$QF B QD B $\frac{1}{2}$QF$\}$ [50], in which QF and QD denote focusing and defocusing quadrupoles, respectively, O the drift and B the dipole acting along x. The main parameters of the example FODO listed in Table 6.2. For simplicity we chose $k_{0,x} = k_{0,y} = k_0$. The matched solution set $\{\sigma_{x0}, \sigma'_{x0}, \sigma_{y0}, \sigma'_{y0}, D_{x0}, D'_{x0}\}$ and the space-charge-modified betatron functions $\beta_x = \sigma_{x0}^2/\varepsilon_{dx}$ can be obtained numerically using shooting method from Eqs. 6.3 and Eq. 6.2. The results are present in Fig. 6.3 and Fig. 6.4 in varying beam intensity in terms of η_x. It can be seen from Fig. 6.3 that for a fixed beam intensity, the betatron function behaves differently with and without dispersion: betatron functions in x almost keeps

Table 6.2.: Main parameters of the example AGD

Parameters [unit]	Symbols	Values
Length of the AGD [m]	L	18.0
Length of QF [m]	l_f	4.0
Length of QD [m]	l_d	4.0
Length of dipoles [m]	l_B	2.618
Length of drift [m]	l_o	1.191
Radius of curvature [m]	ϱ_0	10.0
Generalized emittance on x [mm mrad]	ε_{dx}	10.0
Generalized emittance on y [mm mrad]	ε_{dy}	10.0
rms momentum spread	σ_δ	0.002

unchanged, but changes dramatically in y, since the dispersion breaks the symmetric property.

Fig.3 presents the results of space-charge-modified dispersion for AGD using Eq. 6.2, compared with the results for CFD using Eq. 6.7 and the approximated results using scaling law of Eq. 6.14. It can be seen that results from scaling law (dashed line in Fig. 6.4) is equal approximately to the average value of the dispersion functions in AGD (dotted line in Fig. 6.4) within in the range of moderate space charge ($\eta \leq 0.2$).

6.2.5 RMS-Matched Distribution

The generalized envelope equation of Eq. 6.2 and Eq. 6.3 based on the invariant generalized emittance ε_{dx} and ε_{dy} are often employed to investigate beam dynamics with space charge and dispersion [33, 34]. In PIC simulations of beam dynamics in circular accelerators, the effect of dispersion complicates the beam behavior and the dispersion tends to be difficult to be separated [34]. In this subsection, we introduce a method on how to generate the transverse particle distribution, which is matched to both Space Charge and Dispersion in the rms sense (called "SCD distribution"), and can be used in PIC simulations for a bent lattice. A major advantage of the SCD distribution is that the generalized rms emittance ε_{dx}, ε_{dy} are invariant, and σ_x and $\sigma_\delta D_x$ can be detected separately from the total beam size X in the simulation.

The SCD distribution can be generated in three steps as follows. At first, the particle distribution (e.g. waterbag, Gaussian or KV) rms-matched to the space charge modified lattice functions can be obtained from Eqs. 6.3 under the assumption of zero momentum spread. Secondly, space-charge-modified dispersion function and its derivate D_x, D'_x can be obtained from Eq. 6.2. Finally, in order to match the dispersion, coordinate transformation is performed for each macro-particle used in simulation: $x = \bar{x} + \delta D_x$ and $x' = \bar{x}' + \delta D'_x$, Here $\bar{x}$ and $\bar{x}'$ are the individual macro-particle coordinates *before* transformation, and x and x' are the ones *after* transformation; δ represents the cor-

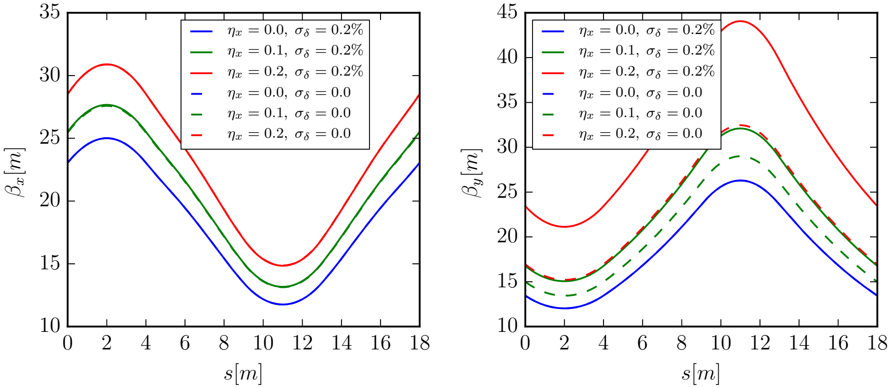

Figure 6.3.: Space-charge-modified betatron functions in x (left plot) and y (right plot) with (solid line) and without (dashed line) dispersion effect in one AGD periodic cell, for $\eta_x = 0.0, 0.1, 0.2$.

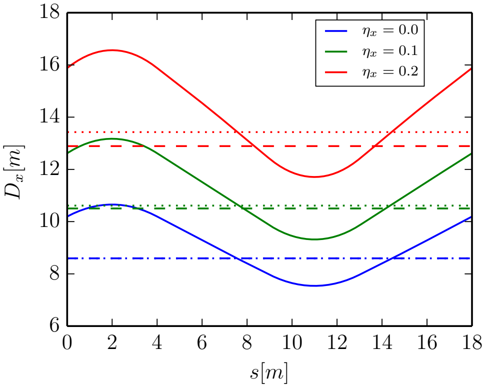

Figure 6.4.: Space-charge-modified dispersion functions in one AGD periodic cell (solid line) with varying beam current ($\eta_x = 0.0, 0.1, 0.2.$), compared with the dispersion in CFD case (dotted line) and the approximated dispersion evaluated from the scaling law (dashed line).

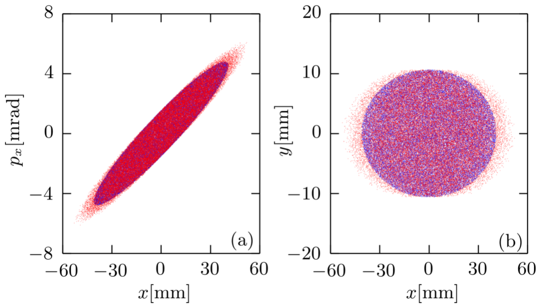

Figure 6.5.: An example of the SCD distribution (red) in $x - x'$ phase space (a) and $x - y$ real space (b), generated from a KV distribution (blue) by coordinate transformation. $\varepsilon_{dx} = 10.0$ mm mrad, $\sigma_\delta = 1.0 \times 10^{-3}$.

responding individual fractional momentum deviation of each macro-particle. In the above process, the coordinates $\bar{x}, \bar{x}'$ of all macro-particles form the betatron beam size $\sigma_x = \sqrt{\langle \bar{x} \rangle^2}$ and the generalized rms emittance $\varepsilon_x = \sqrt{\langle \bar{x}^2 \rangle \langle \bar{x}'^2 \rangle - \langle \bar{x}\bar{x}' \rangle^2}$ in x and can be tracked in the simulation. For the cases with moderate space charge, ε_{dx} stays constant in the simulation. The coordinates x, x' form the total rms beam size X and the total rms emittance ε_x. Since the effect of dispersion is assumed acted only in x, in y no coordinate transformation is needed.

It is worth pointing out that the SCD distribution is dependent on the momentum spread distribution, and thus is not strictly self-consistent with space charge, since the space charge force becomes nonlinear during the process of coordinate transformation. Nevertheless, the relation in Eq. F.4 indicates that the distribution generated by the above procedure is *rms*-matched to the external focusing force, the space charge and the dispersion. As long as the space charge is moderate, which is typical in most circular machines [4], the total rms beam size X and Y will not be dramatically influenced by the nonlinear space charge force, indicating that the generalized rms emittance ε_{dx} and ε_{dy} stays constant.

6.3 Mismatched Beam Motion

6.3.1 Dispersion Matching

As introduced in section 1, for a matched beam characterized with $\{\sigma_{x0}, \sigma_{y0}, D_{x0}\}$, the total matched rms beam size $X_0(s)$ consists of two independent parts: betatron beam size $\sigma_{x0}(s)$ and dispersion beam size $\sigma_\delta D_{x0}(s)$ satisfying the relation

$$X_0^2 = \sigma_{x0}^2 + \sigma_\delta^2 D_{x0}^2, \tag{6.15}$$

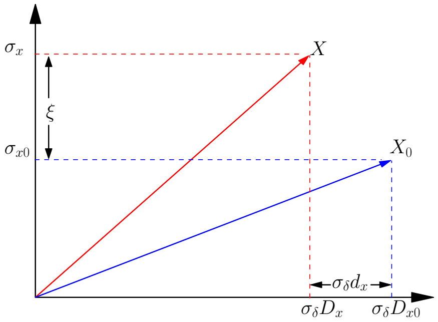

Figure 6.6.: The orthogonal decomposition of total rms beam size as a 2-D vector for matched and mismatched cases.

X_0 can be plotted as a vector $\overrightarrow{X_0}$ in a Cartesian coordinate plane, with its two orthogonal component $\sigma_{x0}(s)$ and $\sigma_\delta D_{x0}(s)$, as schematically shown in Fig. 6.6.

Consider a mismatched case $\{\sigma_x, \sigma_y, D_x\}$ with the deviations $\{\xi, \zeta, d_x\}$ from the matched case: $\sigma_x = \sigma_{x0} + \xi, \sigma_y = \sigma_{y0} + \zeta$ and $D_x = D_{x0} + d_x$, it can be also plotted as a 2D vector $\overrightarrow{X}$, with the components of σ_x and $\sigma_\delta D_x$, as shown in Fig, 6.6. In the presence of space charge and dispersion, the beam matching condition is satisfied only with the condition that both of the betatron component σ_x and dispersion component D_x are matched to the lattice and the space charge. Mismatched oscillation can be described by the oscillation of $\overrightarrow{X}$ around $\overrightarrow{X_0}$. In the absence of space charge, the oscillation only performs along the direction of σ_x-axis. In the presence of both space charge and dispersion, the oscillation performs along the directions both of the σ_x-axis and $\sigma_\delta D_x$-axis.

6.3.2 Generalized Envelope Oscillations

In realistic mismatched case, $\{\sigma_x, \sigma_y, D_x\}$ is slightly deviated from the matched solution $\{\xi, \zeta, d_x\}$, generated by small perturbations: $\sigma_x = \sigma_{x0} + \xi, \sigma_y = \sigma_{y0} + \eta$ and $D_x = D_{x0} + d_x$ which could be due to magnetic errors or misalignment of lattice elements. After Taylor expanding of $\{\sigma_x, \sigma_y, D_x\}$ in terms of $\{\sigma_{x0}, \sigma_{y0}, D_{x0}\}$ and neglecting the higher order terms, noting that the horizontal beam width: $X = X_0 + \xi\sigma_{x0}/X_0 + \sigma_\delta^2 D_{x0} d_x / X_0$, we can obtain from Eq. 6.2 and Eq. 6.3 the oscillation equations of envelope oscillation [4]

$$\begin{aligned} \xi'' + a_0\xi + a_1\eta + a_2 d_x &= 0, \\ \eta'' + a_1\xi + a_3\eta + a_4 d_x &= 0, \\ d_x'' + \frac{a_2}{\sigma_\delta^2}\xi + \frac{a_4}{\sigma_\delta^2}\eta + a_5 d_x &= 0, \end{aligned} \tag{6.16}$$

with the coefficients

$$\begin{aligned} a_0 &= \kappa_{x0} - \frac{K_{\mathrm{sc}}}{2X(X+Y)} + \frac{K_{\mathrm{sc}}\sigma_x^2(2X+Y)}{2X^3(X+Y)^2} + \frac{3\varepsilon_{dx}^2}{\sigma_x^4}, \quad a_1 = \frac{K_{\mathrm{sc}}\sigma_x}{2X(X+Y)^2}, \\ a_2 &= \frac{K_{\mathrm{sc}}\sigma_\delta^2 D_x \sigma_x (2X+Y)}{2X^3(X+Y)^2}, \qquad a_3 = \kappa_{y0} + \frac{K_{\mathrm{sc}}}{2(X+Y)^2} + \frac{3\varepsilon_{dy}^2}{\sigma_y^4}, \\ a_4 &= \frac{K_{\mathrm{sc}}\sigma_\delta^2 D_x}{2X(X+Y)^2}, \qquad a_5 = \kappa_{x0} - \frac{K_{\mathrm{sc}}}{2X(X+Y)} + \frac{K_{\mathrm{sc}}\sigma_\delta^2 D_x^2(2X+Y)}{2X^3(X+Y)^2}. \end{aligned} \tag{6.17}$$

In the expressions of a_0 to a_5, we use X, σ_x, σ_y and D_x to represent their corresponding matched quantities and neglect the subscript “0” for the sake of brevity. Eqs. 6.16, recognized as a set of second order differential equations with variable coefficients, behaves like three coupled harmonic oscillators and can be decoupled to three fundamental modes with oscillation frequencies $\{\omega_i\}$ and the corresponding phase shift $\{\varphi_i = 2\pi\omega_i\}$ $(i = 1, 2, 3)$. For AGD case, based on matched solutions from Eq. 6.2 and Eqs. 6.3, the three fundamental modes can be obtained numerically. For CFD with $\kappa_{x0} = \kappa_{y0} = \kappa_0$, three decoupled fundamental modes can be obtained analytically for both limits of zero beam current and space charge, which can provide useful physical insight: In the limit of zero beam current, Eqs. 6.16 becomes decoupled and the phase shifts of three fundamental modes are:

$$\varphi_1 = \varphi_2 = 2k_0, \quad \varphi_3 = k_0. \tag{6.18}$$

Here k_0 is the phase advance in the absence of space charge. On the other hand, for strong space charge, approaching the space charge limit, we can obtain the three fundamental modes in the space charge limit:

$$\varphi_1 = \sqrt{2}k_0, \quad \varphi_2 = k_0, \quad \varphi_3 = 0. \tag{6.19}$$

In both limits in Eq. 6.18 and Eq. 6.19 , φ_1 and φ_2 are the phase shifs of the two envelope modes and have the identical form as in the case without dispersion[6]. Furthermore, the additional mode, whose phase shift φ_3 tends to zero in the space charge limit, will be identified as the “dispersion mode” because of its relation to dispersion. This mode behaves differently than the two other modes, as will be shown in the following section.

6.3.3 Dispersion Mode

Needless to say, the mode φ_3 described above is related to dispersion effect. For a further investigation, now let us consider the AGD case. We use the example AGD with parameter specified in Table 6.2 and choose $k_0 = 60°$. Phase shifts of three fundamental

---

[6] For more details about the envelope modes, see section 3.3 in chapter 3.

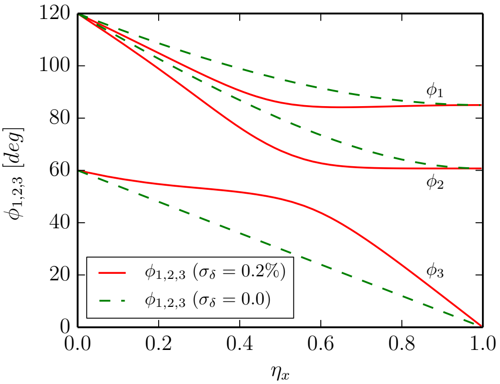

Figure 6.7.: $k_0 = 60°$ case: Phase shifts φ_1, φ_2 and φ_3 versus tune depression η_x with (solid line) and without (dashed line) dispersion.

modes by solving the envelope oscillation set of Eq. 6.16 are present in Fig. 6.7. As can be seen in the figure, both of the cases with and without momentum spread (dispersion effect) have the same limit of zero beam current and space charge, which is in agreement with the analysis results in Eq. 6.18 and Eq. 6.19 for the CFD case. The fast and slow mode φ_1 and φ_2 decrease faster in the presence of dispersion than in the case without dispersion. This is because dispersion lead to larger beam intensity under the same tune depression in x, compared with the case of no dispersion. Furthermore, with zero momentum spread (i.e. without dispersion), the motion equation of d_x in Eqs. 6.16 has the identical form as the transverse motion of single particle (see dashed line in Fig. 6.7). With non-zero momentum spread, the motion of d_x is coupled to the other two modes because of space charge (see solid line in Fig. 6.7).

PIC simulation are performed to show the dispersion mode in a more visible way. To this end, 50 000 particles are tracked after 1000 periodic cells and Fourier analysis are performed on the second moments $\langle x^2 \rangle$ and $\langle y^2 \rangle$ to obtain the beam spectrum. As shown in Fig. 6.8, three modes can be observed in the beam spectrum, and in good agreement with the results from numerical envelope approach of Eq. 6.16. The two modes $\varphi_1 = 83.2°$ and $\varphi_2 = 94.6°$ are the phase shift of the slow mode and fast mode, respectively. The third one $\varphi_3 = 52.7°$ characterizes the dispersion mode.

6.4 Instabilities with Dispersion

As discussed in chapter 3, one of the envelope modes could resonate with the periodic lattice structure and lead to the parametric resonance, or the two modes could resonate with each other and lead to the 90° envelope instability [17, 76]. In the following we will show that in the presence of dispersion, the usual 90° envelope instability also

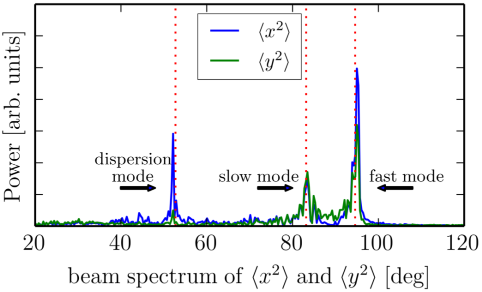

Figure 6.8.: Beam spectrum of $\langle x^2 \rangle$ (blue) and $\langle y^2 \rangle$ (green) in the presence of dispersion and space charge from PIC simulation, compared with the results of fast mode, slow mode and dispersion mode calculated from envelope oscillation equation (dashed red line) of the example AGD with $k_0 = 60^\circ$

exists, with its stopbands slightly shifted, compared with the case without dispersion. Moreover, in the presence of dispersion, the identified dispersion mode could also resonate with other two envelope modes under certain beam current intensity in periodic lattice, and can induce the recently discovered dispersion-induced instability [4].

Analogy to the treatment introduced in chater 3, the stability analysis in the presence of dispersion can be performed by integrating Eqs. 6.16 over one periodic focusing cell (from m to $m+1$)

$$\zeta_{m+1} = M\zeta_m, \tag{6.20}$$

where M is the map for the perturbation vector $\zeta = (\xi, \xi', \eta, \eta', d_x, d_x')$ over one cell. As $\{\sigma_x, \sigma_x', \sigma_y, \sigma_y', D_x, D_x'\}$ in Eq. 6.2 and Eqs. 6.3 follow the Hamiltonian of Eq. F.1, the six eigenvalues of M: $\lambda_i = |\lambda_i|e^{i\varphi_i}$ $(i = 1, 2, \ldots, 6)$ exist only as reciprocal or as conjugate in three pairs: $\{\lambda_1, \lambda_1^*\}$, $\{\lambda_2, \lambda_2^*\}$, $\{\lambda_3, \lambda_3^*\}$. Moreover, taking each oscillation mode in space charge limits in Eq. 6.19 as reference, we can select a suitable set of phase shifts $\{\varphi_1, \varphi_2, \varphi_3\}$ with corresponding moduli $\{|\lambda_1|, |\lambda_2|, |\lambda_3|\}$ representing fast mode, slow mode and the dispersion mode respectively, to fully characterize the beam oscillation without loss of generality. One of the three moduli larger than unity can be used as instability growth factor. For detailed analysis of the movement of the six eigenvalues in the presence of dispersion under different beam intensity see Appendix F.

Taking the AGD lattice with parameters listed in Table 6.2 as an example with $k_{0,x} = k_{0,y} = k_0$, the numerical integration of Eq. 6.20 is performed and the results of $\{\varphi_1, \varphi_2, \varphi_3\}$ are shown in Fig. 6.9, Fig. 6.10 and Fig. 6.11 for the three representative cases of $k_0 = 90^\circ$, $k_0 = 120^\circ$ and $k_0 = 130^\circ$ respectively, compared with the corresponding case of zero momentum spread. Fig. 6.9 shows a stable case with growth factors are equal to unit (not shown here), and the three modes have a similar behavior as the case of $k_0 = 60^\circ$ in Fig. 6.7. In contrary, Fig. 6.10 and Fig. 6.11 are shown with growth

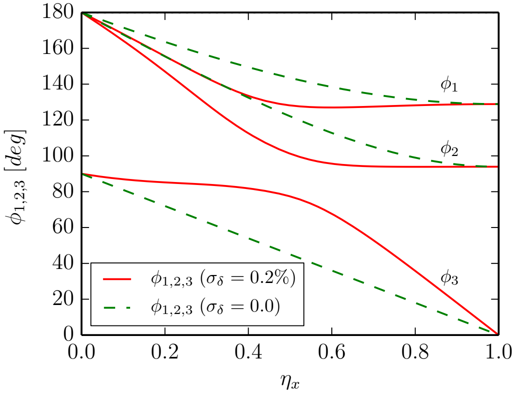

Figure 6.9.: $k_0 = 90°$ case: Phase shifts φ_1, φ_2 and φ_3 versus tune depression η_x with (solid line) and without (dashed line) dispersion.

factors larger than unit, illustrating beam instabilities, which will be mainly discussed in the following.

6.4.1 Dispersion-Modified Envelope Instability

For a more illustrative analysis of instabilities, we introduce another notation to represent the phase shift of dispersion mode: $\varphi_d = 360° - \varphi_3$. Clearly, φ_d is advanced while φ_3 reduces with the beam current increasing, as shown the solid line in Fig. 6.10. For $k_0 = 120°$ in Fig. 6.10, φ_1, φ_2 decrease and φ_d increases from 240° while φ_3 decreases from 120°. Following the curve with nonzero σ_δ (solid red line), in the region of $\eta_x = 0.233$ to 0.275 (shallow shaded area in Fig. 6.10), the corresponding growth factor regions (stop band) indicates instability, which can be identified as half-integer resonance (parametric resonance) since φ_1 reaches and is locked on the 180° line. Increasing beam current, φ_1 and φ_2 are confluent and the confluent resonance is excited (dark shaded area in Fig. 6.10). Below $\eta_x = 0.558$, the two modes are separated and the envelope instability disappears. Note that with dispersion, the parametric resonance can be observed between $\eta_x = 0.233$ to 0.275 since the dispersion effect breaks the symmetric property and the beam becomes elliptical. Consequently, φ_1 falls faster and arrives at the 180° line much earlier than φ_2. In contrary, in the absence of dispersion effect, as shown in dashed in the top plot of Fig. 6.10, parametric and confluent resonance can not be separated because of symmetric property of the matched round beam.

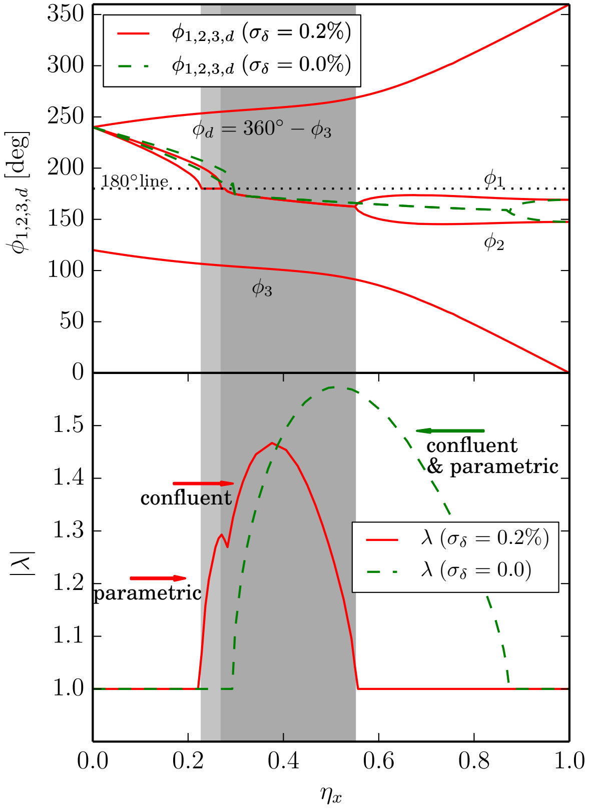

Figure 6.10.: $k_0 = 120°$ case. Upper: Phase shifts φ_1, φ_2, φ_3 and φ_d versus tune depression η_x, with (solid red) and without (green dashed) dispersion; Lower: Growth factor $|\lambda|$ versus η_x with (red) and without (green) dispersion. (Shaded area denotes the stop band of the envelope instability modified by dispersion: parametric resonance (shallow) and confluent resonance (dark)).

6.4.2 Dispersion-Induced Envelope Instability

The instability induced by dispersion is illustrated in Fig. 6.11 for $k_0 = 130°$, where dispersion mode becomes unstable. The stop band from $\eta_x = 0.092$ to 0.153 (shade area in Fig. 6.11) indicates instability (the corresponding simulation results of the emittance growth and phase space evaluation shown in Fig. 6.11 will be discussed later). Since in this region, confluence occurs between the dispersion mode φ_d and the slow mode φ_1 (solid curve in the top plot of Fig. 6.11), this instability is induced by periodic focusing and dispersion and can be related to a resonance between the two modes. For completeness, phase shifts of φ_1 and φ_2 in the absence of momentum spread are plotted for comparison in the top plot of Fig. 6.11.

A criteria for the occurrence of dispersion-induced instability can be given based on the following analyses: in Fig. 6.11, $\varphi_1^0 = 260°$, $\varphi_d^0 = 240°$ and $\varphi_d^0 < \varphi_1^0$ (here the superscript “0" denotes values in the absence of space charge). This is different from the case in Fig. 6.10, in which $\varphi_1^0 = \varphi_2^0 = \varphi_d^0 = 240°$ and no confluence occurs between φ_1 and φ_d. These analyses show that only if $\varphi_1^0 > \varphi_d^0$, e.g. $2k_0 > 360° - k_0$, or $k_0 > 120°$, φ_1 and φ_d can be confluent, and hence the dispersion-induced instability occurs. In other words, for a lattice of $k_{0,x} = k_{0,y} = k_0$, only with $k_0 > 120°$ satisfied, the dispersion-induced instability may occur within a certain beam current range. For a more physical interpretation, the extended envelope oscillation system including dispersion contains three fundamental modes. The mode of dispersion oscillation (φ_d or φ_3) behaves, to some extend, like a single particle as Eq. 6.2 lacks the emittance term, which is different from the two other modes φ_1 and φ_2. For a lattice of $k_{0,x} = k_{0,y} = k_0$ only with $k_0 > 120°$, φ_d-mode may resonate with φ_1-mode in a certain beam current range, and induce the beam instability with the periodic focusing. For completeness, it can be observed that the usual 90° envelope instability from parametric and confluent resonances exist below $\eta_x = 0.277$, which is similar to the case of $k_0 = 120°$ in Fig. 6.10.

The criteria above can be extended to a more general case. Let us consider a periodic lattice with $k_{0,x} > k_{0,y}$ (An example with $k_{0,x} = 130°$, $k_{0,y} = 120°$ is shown in Fig. 6.12). With increasing beam current the fast mode φ_1 and the slow mode φ_2 decrease from $2k_{0,x}$ and $2k_{0,y}$ respectively, while φ_d increases from $360° - k_{0,x}$. Therefore, φ_1 can be confluent with φ_d when satisfying $2k_{0,x} > 360° - k_{0,x}$, e.g.

$$k_{0,x} > 120°. \tag{6.21}$$

Therefore the dispersion-induced envelope instability can be named “120° dispersion instability”, in contrast to the usual envelope instability related to $k_{0,x,y} > 90°$.

Two main properties of the 120° dispersion instability are briefly demonstrated in following. Firstly, in the general case for $k_{0,x} \neq k_{0,y}$, as shown in Fig. 6.12 with $k_{0,x} = 130°, k_{0,y} = 120°$ as an example, although φ_2 intersects with φ_d at $\eta_x = 0.0384$, no confluence between them. Confluence only occurs between φ_1 and φ_d. These observations indicate one important feature of dispersion induced instability: it occurs only within the dispersion acting plane (in the context it is in x), in which space charge effect,

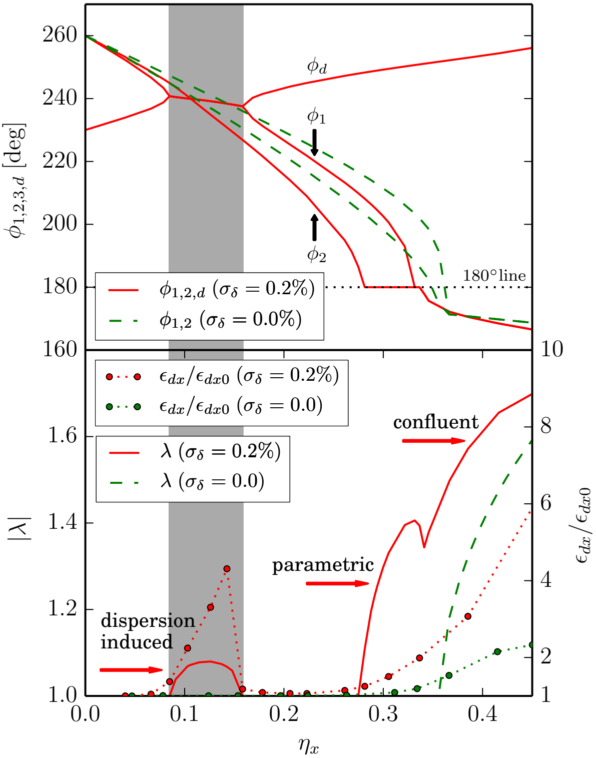

Figure 6.11.: $k_0 = 130°$ case: Upper: Phase shifts φ_1, φ_2, φ_d versus tune depression η_x, with (solid red) and without (green dashed) dispersion; Lower: Growth factor from numerical calculation and normalized emittance growth ϵ_x/ϵ_{x0} from PIC simulation versus tune depression η_x with (red) and without (green) dispersion. (Shaded area denotes the stop band of the dispersion-induced instability, characterized by the confluence of φ_1 and φ_d.

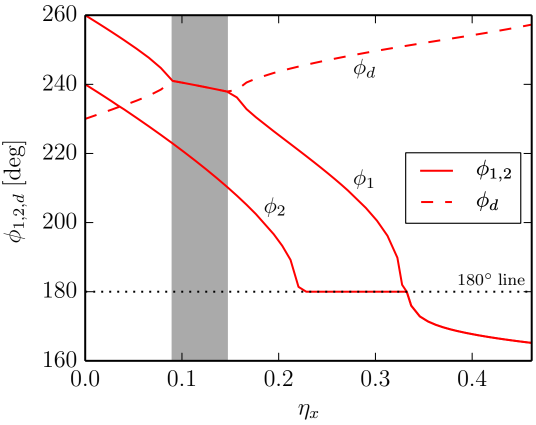

Figure 6.12.: $k_{0,x} = 130°, k_{0,y} = 120°$ case: Phase shifts of modes $\varphi_1, \varphi_2, \varphi_d$ versus tune depression η_x with dispersion effect.

external periodic force and dispersion effect have a combination effect on beam collective motion. Secondly, we use the notation φ_d defined as $\varphi_d = 360° - \varphi_3$ to illustrate the mechanism of the dispersion-induced instability. In fact, the condition $\varphi_{1,2} = \varphi_d$ is actually $\varphi_{1,2} + \varphi_3 = 360°$. Therefore, the dispersion-induced instability can be identified as a “sum parametric resonance" [22] between the envelope mode φ_1 or φ_2 and the dispersion mode φ_3.

PIC simulation have been performed using PyORBIT [70] as validation and support of above results and conclusions. The initial particle distribution is chosen as a SCD distribution generated from transverse waterbag, which is rms matched with both effects of space charge and dispersion. As shown in dotted lines in the bottom plot of Fig. 6.11, simulation results of horizontal normalized emittance growth (in unit of the initial one) ϵ_x/ϵ_{x0} is taken after 500$^{\text{th}}$ focusing periods, at which both the beam size and emittance growth caused by envelope instability have already saturated. In Fig. 6.11, emittance growth with and without dispersion are in agreement with the corresponding stop band from the envelope perturbation theory in the top plot. We point out here that for the both cases with and without dispersion in Fig. 6.11, slight emittance growth exists near $\eta = 0.31$ ($k_x = 90°$), which is due to the combined envelope instability and fourth order structure resonance. In the range of $\eta_x = 0.085$ to 0.162 in Fig. 6.11b, the emittance growth is only found with nonzero beam momentum spread, which is a clear validation of the dispersion induced instability. Simulation results of particle distribution in transverse phase space and real space are present in Fig. 6.13. As can be seen, the transverse emittance and the transverse beam size grows rapidly when the dispersion-induced instability take places. The process gets saturated within 500 periodic cells.

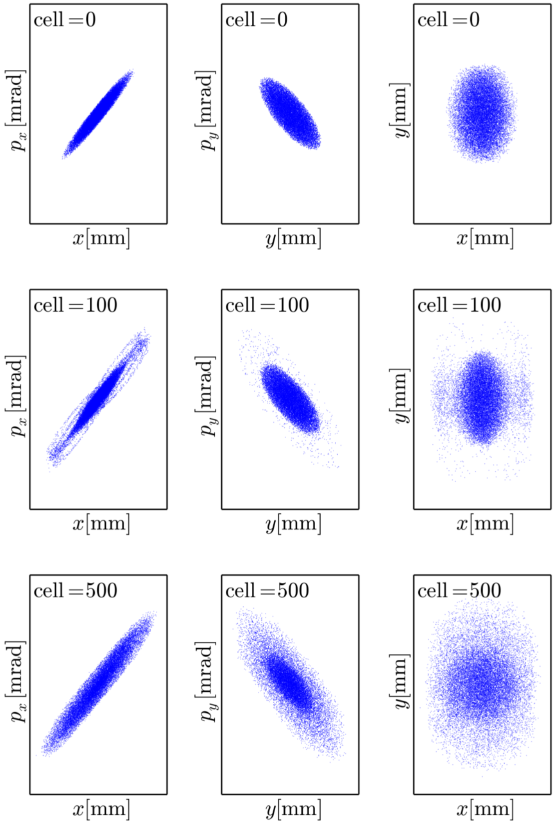

Figure 6.13.: PIC simulation results of particle distribution evolution in transverse phase space and real space for $k_0 = 130°$ and $\eta_x = 0.885$ $(k_x = 115°)$.

7 Space Charge Limitation for Bunch Compression in Synchrotrons

In this chapter, we investigate the 3-D beam behavior during bunch compression in high-current synchrotrons, with an example case in GSI SIS-18. The transverse envelope equations introduced in previous chapter are coupled with the longitudinal envelope equation. Based on the coupled longitudinal-transverse envelope equation set and also particle-in-cell (PIC) simulations, the mechanism of the coherent beam instability and the incoherent single particle resonance related to the enhanced space charge during bunch compression are analyzed in detailed.

Section 7.1 presents the theoretical model of the coupled longitudinal-transverse envelope equation set and PIC simulations of bunch compression. In section 7.2, as an application of the two approaches to describe the bunch compression in SIS-18, we solve numerically the coupled envelope equation set with a set of typical beam parameters, in comparison with PIC simulation results. At last, in section 7.3 two major space-charge limits for bunch compression in SIS-18 with phase advance crossing the resonance conditions related to 90° and 120° line are investigated. The competing mechanisms of the fourth-order resonance, envelope instability and dispersion-induced instability during bunch compression are demonstrated.

7.1 Two Approaches of Bunch Compression

The envelope approach and PIC simulations are two commonly used methods for bunch compression study. Based on the longitudinal envelope equation introduced in section 3.4, the required rf voltage for bunch rotation can be calculated [45]. The transverse space-charge tune shift during bunch compression can be obtained by solving the transverse envelope equation set [46]. This section introduces the coupled longitudinal-transverse envelope equation set, and briefly discusses several considerations for performing simulations of bunch compression. In the following we assume x and y for the horizontal and vertical directions, and z the longitudinal one; s is distance as independent variable. $k_{0,x,y}$, $k_{x,y}$ are the phase advances per focusing cell without and with space charge, respectively.

7.1.1 Coupled Longitudinal-Transverse Envelope System

Let us start with a bunched beam with parabolic distribution in the longitudinal plane, for which the space charge forces are linear in z. The corresponding longitudinal envelope equation including space charge takes the form[1]

$$z_m'' + \kappa_{z0} z_m - \frac{K_L}{z_m^2} - \frac{\varepsilon_L^2}{z_m^3} = 0. \tag{7.1}$$

Here, z_m is the half length of the bunch, and κ_{z0} is the linearized external rf focusing force defined in Eq. 3.36. V_{rf} is the rf voltage required for fast bunch compression, Zq and Am_0 the charge and the mass of the particle, h the harmonic number, η the slip factor, c the speed of light, β and γ the relativistic factors, and R the average radius of the synchrotron. The linearized external focusing gradient modified by longitudinal space charge is $\kappa_z = \kappa_{z0} - K_L/z_m^3$, with the longitudinal perveance $K_L = 3gNZ^2 r_p/(2\beta^2\gamma^5 A)$; the geometry factor $g = 0.5 + 2\ln(R_p/R_b)$ (R_p and R_b are the radii of the beam pipe and the beam, respectively); N the number of particles in the bunch; r_p the classical proton radius and η the slip factor. ε_L is the longitudinal emittance, defined as

$$\varepsilon_L = |\eta| z_m \delta_0, \tag{7.2}$$

in which δ_0 is the momentum spread at the center of the bunch $\delta_0 = \delta(z = 0)$, as shown in Fig. 7.1. Physically, ε_L denotes the area in longitudinal phase space, which is constant without acceleration. During compression, the ellipse of the longitudinal emittance rotates and becomes tilted, and the maximum momentum spread of the bunch $\tilde{\delta}$ can be express as $\delta_m^2 = \hat{\delta}^2 + \delta_0^2$. Here, $\hat{\delta}$ is the momentum spread of the particles at the edge of the bunch, and δ_0 the maximum momentum spread at the bunch center.

The rf voltage required for bunch compression can be derived by integrating Eq. 7.1 [45],

$$\int \mathrm{d}\Big(\frac{z_m'^{\,2}}{2}\Big) + \kappa_{z0} \int z_m \mathrm{d}z_m - K_L \int \frac{\mathrm{d}z_m}{z_m^2} - \varepsilon_L^2 \int \frac{\mathrm{d}z_m}{z_m^3} = 0, \tag{7.3}$$

from which we obtain a longitudinal invariance,

$$I_L = \frac{z_m'^2}{2} + \frac{\kappa_{z0}}{2} z_m^2 + \frac{K_L}{z_m} + \frac{\varepsilon_L^2}{2z_m^2}. \tag{7.4}$$

---

[1] For more details of the longitudinal envelope equations and the parabolic distribution, see section 3.4.

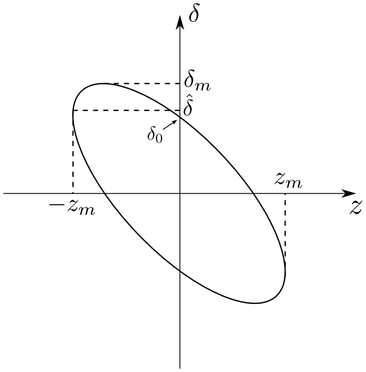

Figure 7.1.: Definition of parameters in longitudinal phase space. z denotes the longitudinal direction, and $\delta = \Delta p / p_0$ is the relative momentum deviation.

It is convenient to introduce a compression factor χ ($\chi \leq 1$), defined as

$$z_{m,f} = \chi z_{m,i}, \tag{7.5}$$

in which $z_{m,f}$ and $z_{m,i}$ denote the initial and final longitudinal envelope during bunch compression. For the ideal bunch compression with a parabolic distribution and linear longitudinal space charge force, the longitudinal emittance ε_L remains invariant, and the final momentum spread results as $\delta_{m,f}$ obeys $\delta_{m,f} = \frac{\delta_{m,i}}{\chi}$.

Substituting $z_{m,i}$, $z_{m,f}$ and $\delta_{m,i}$, $\delta_{m,f}$ into the invariant emittance of Eq. 7.3, and using the compression factor χ, we can obtain

$$\kappa_{z0} = \left(\frac{|\eta| \delta_{m,i}}{z_{m,i} \chi} \right)^2 \left[1 + \frac{2 K_L z_{m,f}}{\varepsilon_L^2 (1 + \chi)} \right]. \tag{7.6}$$

The required rf voltage for bunch compression can be derived via substituting Eq. 7.6 into Eq. 3.36,

$$V_{rf} = \left(\frac{|\eta| \delta_{m,i}}{z_{m,i} \chi} \right)^2 \left[1 + \frac{2 K_L z_{m,i} \chi}{\varepsilon_L^2 (1 + \chi)} \right] \frac{2 \pi R^2 \gamma \beta^2 A m_0 c^2}{Z q h \eta}. \tag{7.7}$$

It can be seen from Eq. 7.7 that the rf voltage for the bunch compression is a function of the initial bunch length $z_{m,i}$, momentum spread $\delta_{m,i}$ and the compression factor χ. V_{rf} is inversely proportional to the bunch compression factor χ, or the final bunch length $z_{m,f}$.

Since during bunch compression the synchrotron phase are chosen to zero, the synchrotron frequency can be written as (see, for example, in Ref. [50])

$$\omega_s = \sqrt{\frac{ZqhV_{rf}|\eta|}{2\pi R^2 A m_0 \gamma}}. \tag{7.8}$$

Since bunch compression are performed by one quarter synchrotron motion, the turns needed for compression are

$$n = \frac{1}{4}\frac{\omega_0}{\omega_s}, \tag{7.9}$$

where $\omega_0 = \beta_0 c/R$ is the revolution frequency. Note that in Eq. 7.8 and Eq. 7.9 the longitudinal space charge is ignored. For the parameters in the present study, longitudinal space charge is sufficiently small that Eq. 7.9 can be used to calculate the turns required for bunch compression.

The longitudinal envelope equation of Eq. 7.1 can be used to describe the longitudinal beam dynamics and calculate the required rf voltage in bunch compression. By including the space-charge modified dispersion, the envelope equations become a useful tool to study the transverse collective motion in synchrotrons. During bunch compression, both space charge and its effect on dispersion are increasing. Therefore, the transverse envelope equation should be coupled with the longitudinal equation to give a full description of the beam dynamics of bunch compression.

There are several considerations when applying the coupled set of equations on bunch compression. The first consideration is that even for fast bunch rotation the synchrotron frequency is much smaller than the transverse one, which means space charge is increasing “adiabatically” for the transverse motion. Therefore, it is reasonable to assume that the beam has sufficient time to remain matched to the transverse lattice during bunch compression. The second point is that the variable z_m in the longitudinal equation should be transformed to its corresponding rms quantity σ_z, in order to calculate the rms momentum spread and dispersion. For parabolic distributions the transformation is performed by $\sigma_z = \sqrt{5} z_m$. Based on above considerations, the coupled longitudinal-transverse set of equations takes the form

$$\begin{aligned}
&z_m'' + \left(\kappa_{z0} z_m - \frac{K_L}{z_m^3}\right) z_m - \frac{\varepsilon_z^2}{z_m^3} = 0,\\
&\sigma_x'' + \left[\kappa_{x0} - \frac{K_{sc}}{2X(X+Y)}\right]\sigma_x - \frac{\varepsilon_{dx}^2}{\sigma_x^3} = 0,\\
&\sigma_y'' + \left[\kappa_{y0} - \frac{K_{sc}}{2Y(X+Y)}\right]\sigma_y - \frac{\varepsilon_{dy}^2}{\sigma_y^3} = 0,\\
&D_x'' + \left[\kappa_{x0} - \frac{K_{sc}}{2X(X+Y)}\right] D_x = \frac{1}{\varrho(s)},
\end{aligned} \tag{7.10}$$

with the coupled relations

$$X = \sqrt{\sigma_x^2 + \sigma_\delta^2 D_x^2}, \quad Y = \sigma_y, \tag{7.11}$$

and

$$\sigma_\delta = \sqrt{\left(\frac{\sigma_z'}{\eta}\right)^2 + \left(\frac{\varepsilon_z}{\eta\sigma_z}\right)^2}, \quad \sigma_z = \sqrt{5}z_m. \tag{7.12}$$

Here, $\kappa_{x0,y0}$ and κ_{z0} are the linearized external focusing gradients in transverse and longitudinal plane, respectively. $\sigma_{x,y}$ denote the transverse rms betatron beam size; X and Y the transverse rms total beam size with dispersion; σ_δ the rms momentum spread; σ_z the rms half bunch length; $\varepsilon_{dx,dy}$ the generalized transverse rms emittance defined in Ref. [29], and ε_z the longitudinal rms emittance defined in Eq. 7.2.

7.1.2 PIC Simulations

A major consideration of PIC-simulation of bunch compression is the treatment of space charge. For typical parameters of bunch compression in synchrotrons, the bunch length after bunch compression is usually in the order of several meters, and much larger than the transverse beam size, which is in the order of centimeters or less. Therefore, as introduced in section 4.2, the treatment of space charge in the simulation can be split into a 1-D longitudinal calculation and a 2-D transverse calculation, which is often referred to as "2.5-D" in literature (see, for example in Ref. [70]).

Another consideration is the generation of the initial particle distribution. The longitudinal one can be chosen as parabolic, which is - at least initially - a self-consistent model. In order to compare with the envelope approach, the external longitudinal rf focusing force is chosen to be linear. In the transverse plane, the initial distribution is chosen as a Gaussian (truncated at 3σ, here σ is the standard deviation).

For bunched beams different longitudinal positions experience different transverse space charge forces, and thus different space-charge modified lattice functions. In the simulation performed here, we adopt the approximation that the initial bunched beam is transversely rms-matched with lattice functions modified by space charge at the longitudinal beam center. The beam current at the center of a parabolic bunch takes the form $I = \varrho_{L0}\beta_0 c = 3NZq\beta_0 c/(4z_m)$. Here N is the number of particles in the bunched beam and $\varrho_{L0} = 3Nq/(4z_m)$ the linear charge density at the beam center. Substituting the beam current into Eq. 7.10, the matched rms beam size can be calculated numerically.

7.2 An Example of Bunch Compression in the SIS-18

The lattice of the SIS-18 consists of 12 periodic cells formed by the sequence {QF B QD B}, in which QF and QD denote focusing and defocussing quadrupoles respectively, and B represents the dipoles. The assumed type of ion is U^{73+}. The related parameters for bunch compression are listed in Tab. 7.1 (See, Ref. [35]). The dependent quantities are shown within the bracket in Tab. 7.1. Note that we are using an idealized lattice for the SIS-18 ignoring magnet multiple and errors. Including these errors of possible beam degradation for bunch compression requires additional studies.

Table 7.1.: Main parameters for an example bunch compression in SIS-18

Parameters [unit]	Symbols	Values
Atomic mass	A	238
Charge state	Z	73
Kinetic energy [MeV/u]	E_k	295
Number of particles per bunch	N	1.0×10^{11}
Circumference [m]	L	216
Slip factor	η	-0.5
Bare tune	$Q_{0,x,y}$	4.27,3.47
Beam pipe width [mm]	$b_{x,y}$	120, 40
Initial half bunch length [m]	$z_{m,i}$	78
(Initial half bunch length [ns])	τ_i	395
Initial rms momentum spread	$\sigma_{\delta,i}$	5×10^{-4}
Final half bunch length [m]	$z_{m,f}$	6.0
(Final half bunch length [ns])	τ_f	30.0
(Ideal final rms momentum spread)	$\sigma_{m,f}$	6.4×10^{-3}
(RF voltage [kV])	V_{rf}	33.7
(Required turns)	n	77
Transverse rms emittance [mm mrad]	$\varepsilon_{x,y}$	15, 5
Phase advance of one periodic cell [deg]	$k_{0x,0y}$	128, 104

7.2.1 Simulation Results

The simulation results of the particle distributions at a fixed potion (at the entrance of QF) are recorded. Fig. 7.2 and Fig. 7.3 show the particle distributions before (the first turn) and after (the 77th turn) bunch compression. It can be seen that the bunch performs a 90° rotation during bunch compression. After compression, compared with Fig. 7.2, the vertical emittance and vertical beam size in Fig. 7.3 stay almost constant; the horizontal emittance growth and enlarged horizontal beam size is from the increasing momentum spread and dispersion during bunch compression and is proved to be reversible, as discussed later in Fig. 7.6. Here and in the following text the transverse emittances are understood as rms emittances.

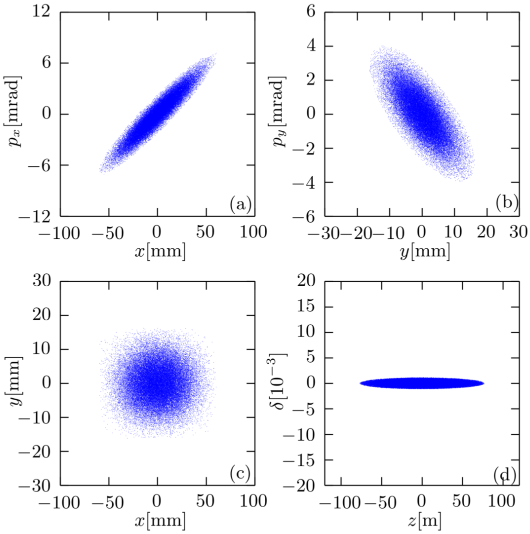

Figure 7.2.: Particle distribution in (a) x-x' phase space; (b) y-y' phase space; (c) x-y real space and (d) longitudinal z-δ phase space before bunch compression.

7.2.2 Envelope Solutions

With the initial parameters listed in Tab. 7.1, the coupled longitudinal-transverse envelope equation set in Eq. 7.10 can be solved numerically. As discussed above, since the synchrotron motion is much slower than the betatron motion during bunch compression, the transverse beam size X can be kept matched to the space-charge modified lattice and dispersion for every turn. In practice, the numerical solution is found as follows: firstly, the half bunch length z_m for each turn is calculated by the longitudinal envelope equation, from which one can obtain by Eq. 7.12 the beam current and momentum spread for each turn during bunch compression. Secondly, based on the beam current, the transverse space charge perveance as a function of turns $K_{\mathrm{sc}}(n)$ is calculated. Using the transverse envelope equation set in Eqs. 7.10 and Eq. 7.11, the evolution of the matched total rms beam sizes $X(n)$, $Y(n)$, the betatron beam sizes $\sigma_x(n)$, $\sigma_y(n)$ and the space-charge-modified dispersion $D_x(n)$ and its derivative $D_x'(n)$ (at the fixed position: the entrance of QF) during compression are obtained, which are all functions of turns.

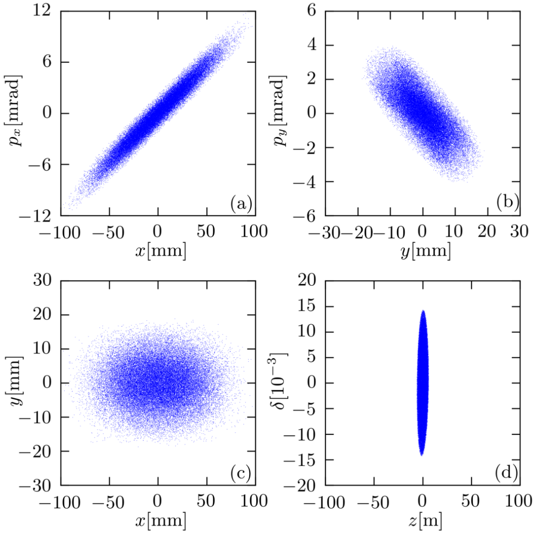

Figure 7.3.: Particle distribution in (a) x-x' phase space; (b) y-y' phase space; (c) x-y real space and (d) longitudinal z-δ phase space after bunch compression.

7.2.3 Comparison of Simulation and Envelopes

The numerical solutions of bunch length z_m are shown in Fig. 7.4 and compared with the simulation results. It can be seen that the evolution of bunch length during bunch compression from the envelope approach is almost perfect matched with the simulation results.

Fig. 7.5 shows the transverse results from the two approaches. The blue solid line and blue dotted line are the transverse rms beam size (X) and betatron rms beam size (σ_x) solved from the coupled envelope method. The red solid line and red dotted line are the transverse rms beam size and betatron rms beam size obtained from the simulation. The former can be obtained directly by the definition of the rms quantity: $X = \frac{1}{N}\left(\sum_{i=1}^{N} x_i^2\right)^{1/2}$, while the latter is obtained by $\sigma_x = \frac{1}{N}[\sum_{i=1}^{N}(x_i - \delta_i D_x)^2]^{1/2}$. Here x_i denotes the horizontal offset of the i^{th} macro particle, N the total number of macro particles in the simulation and D_x the space-charge-modified dispersion solved from the envelope approach. It can be seen from Fig. 7.5 that during bunch compression the total horizontal beam size X is increasing due to the increasing dispersion, while the betatron beam size σ_x remains constant. The results of transverse beam sizes from the envelope approach agree well with the results from PIC simulations.

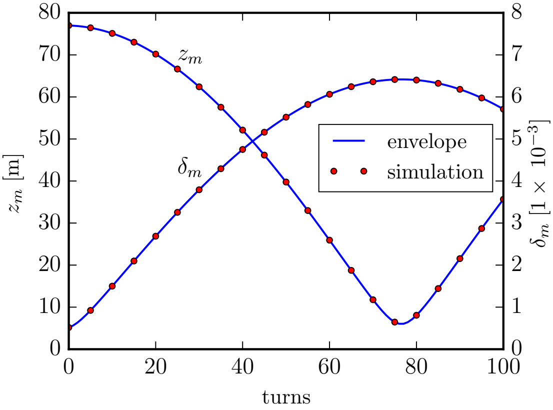

Figure 7.4.: Evolution of bunch length z_m and rms momentum spread δ_m during bunch compression obtained from simulation and envelope approach.

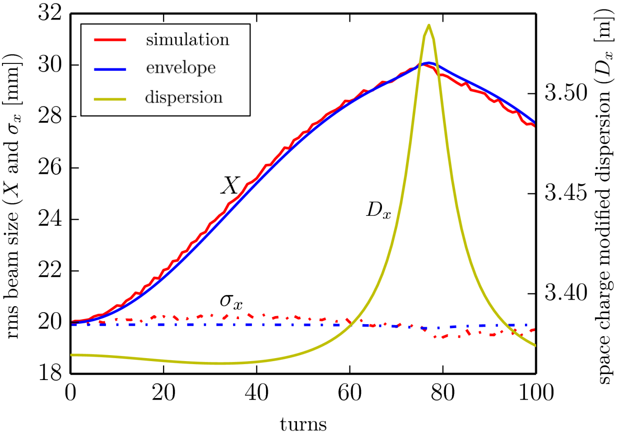

Figure 7.5.: Evolution of the total rms beam size X, the betatron beam size σ_x and the space-charge-modified dispersion D_x during bunch compression obtained from simulation and envelope approach.

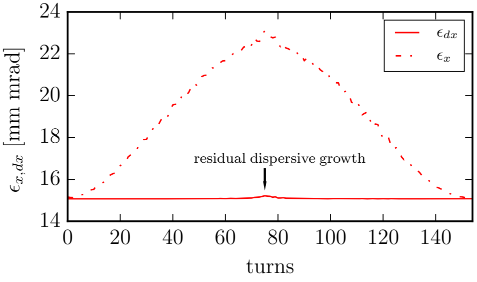

Figure 7.6.: The evolution of horizontal emittance ϵ_x and generalized horizontal emittance ϵ_{dx} during a 180° rotation in the longitudinal phase space.

The dispersive increase in ϵ_{dx} (Fig. 7.3) and in X (Fig. 7.5) are, in principle, reversible and expected to vanish in a dispersion-free section. To illustrate this point, we consider a 180° rotation, with an initial 90° compression followed by a 90° decompression. As plotted in Fig. 7.6, the horizontal emittance ϵ_x is obtained directly from simulations, while the generalized horizontal emittance ϵ_{dx} is calculated based on the coordinate transformation with $x_i - \delta_i D_x$, $x'_i - \delta_i D'_x$ [29], in which D_x and D'_x are obtained from the coupled envelope approach. It can be observed that both the horizontal emittance ϵ_x and the generalized one, ϵ_{dx}, are fully reversible after a 180° rotation. Compared to the large dispersive growth of the horizontal emittance ϵ_x, ϵ_{dx} stays almost constant during bunch compression. Only a slight growth of ϵ_{dx} is observed at the end of the compression (see the arrowhead in Fig. 7.6), where space charge reaches its maximum value. We attribute this to the fact that the space-charge modified dispersive D_x and its derivative D'_x are obtained from the coupled envelope approach with a linear space charge, and assumed to be constant for all particles. For the Gaussian beam in the simulation, however, the space charge is nonlinear and different particles have different values of space-charge modified dispersion. It can be assumed that if the space-charge modified dispersion and its derivative $D_x^{(i)}$, $D_x'^{(i)}$ are exactly known for each particle, the generalized emittance ϵ_{dx} is ideally an invariant after the coordinate transformation $x_i - \delta_i D_x^{(i)}$, $x'_i - \delta_i D_x'^{(i)}$. In other words, the fact that we use the space-charge modified dispersion from envelope (KV) model to evaluate the generalized emittance with nonlinear space charge leads to this *residual dispersive growth* of the generalized horizontal emittance, which is usually small and reversible.

7.3 Enhanced Space Charge Effects During Bunch Compression

The PIC simulation and numerical results in Fig. 7.3 and Fig. 7.5 respectively illustrate that with the parameters listed in Tab. 7.1 only dispersive emittance growth is observed, and the betatron beam size σ_x remains almost constant during the bunch compression in SIS-18.

With higher intensity - k_y getting close to 90° and beyond the case of Tab. 7.1 - can lead to the well-known envelope instability and fourth order single particle resonance. In the horizontal plane the recently discovered dispersion-induced instability could be induced when k_x is approaching and crossing 120°. In this section we have doubled beam intensity in Section **??** and reduced the horizontal phase advance in Section 7.3.2 in order to investigate these issues and their possible impact on space charge limitations during bunch compression in the SIS-18.

7.3.1 90°-related Intensity Limitation

In chapter 3, we have briefly discussed the mechanism difference between the envelope instability and the fourth order single particle resonance. As space charge increasing during bunch compression, they represent two major contributions for space charge limits in high intense beams, with the stop bands related to 90° phase advance per focusing period. In order to investigate the 90°-related intensity limitation during bunch compression, we double beam intensity (from $N = 1 \times 10^{11}$ to 2×10^{11}) in Tab. 7.1 and keep other parameters unchanged. By doing this, the vertical depressed phase advance k_y will cross the 90° line during bunch compression.

Fig. 7.10 shows as solid line the result of depressed phase advances by solving the coupled envelope equation of Eqs. 7.10 with doubled beam intensity. As can be seen, during bunch compression k_x is always above 120°, while k_y crosses the 90° line after turn 71. Particle distributions at turn 71 from PIC simulation are plotted in Fig. 7.7. One can see a clear fourfold structure in $y - p_y$ phase space, characterizing the fourth-order resonance, with the condition

$$4k_y = 360^\circ, \tag{7.13}$$

which is consistent with the numerical results in Fig. 7.10. Particle distributions in $y - p_y$ phase space at three representative turns ($68^{\text{th}}, 72^{\text{nd}}, 76^{\text{th}}$) are shown in Fig. 7.8. The formation of four islands starts at turn 68. With space charge increasing, they move away from the particle core, leading to an increasing emittance. The four islands in Fig. 7.7 and Fig. 7.8 confirm that the emittance growth during bunch compression is due to the fourth-order resonance, and no envelope instability is observed in PIC simulations.

The evolution of transverse emittances in simulation during bunch compression is shown as dashed line in Fig. 7.10. Note that the emittances start to increase at turn 68, slightly before turn 71 where $k_y = 90^\circ$. Also note that for a Gaussian beam k_y is understood as the depressed tune of an equivalent KV beam. In fact, for a *Gaussian* beam, particles have various depressed phase advances and most particles are located in the range from k_y to $\hat{k}_y$, (here $\hat{k}_y = k_{0,y} - 2\Delta k_y$ denotes the maximum depressed phase advance in a Gaussian beam) as shown schematically in Fig. 7.9. Therefore, an

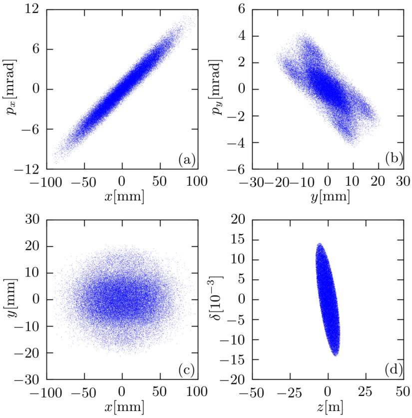

Figure 7.7.: Particle distribution in (a) x-x' phase space; (b) y-y' phase space; (c) x-y real space and (d) longitudinal z-δ phase space at turn 72 during bunch compression, with doubled beam intensity.

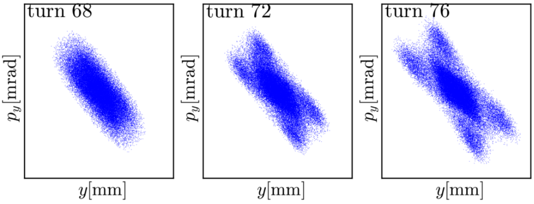

Figure 7.8.: The evolution of particle distribution in the $y - y'$ phase space at final stage of bunch compression with double beam intensity at 68^{th}, 72^{nd}, 76^{th} turns during bunch compression.

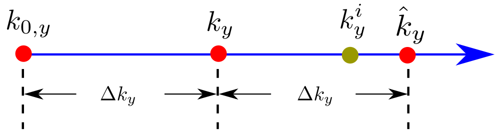

Figure 7.9.: Schematic drawing of the phase advance without space charge $k_{0,y}$, the depressed phase advance shifted by Δk_y for an equivalent KV beam k_y, the most depressed space charge $\hat{k}_y$ shifted by $2\Delta k_y$ in a Gaussian beam, and the phase advance of an individual particle, k_y^i.

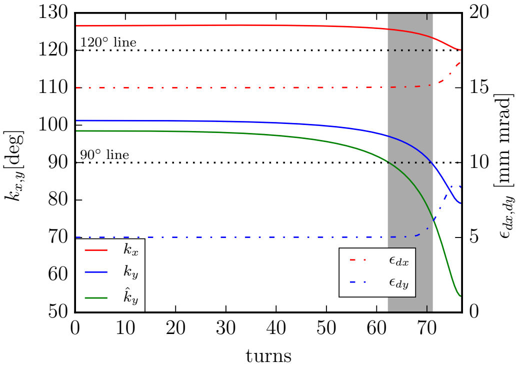

Figure 7.10.: Space-charge depressed phase advances $k_{x,y}$ (solid line) solved from the coupled envelope approach and emittance growth $\epsilon_{dx,dy}$ (dashed line) from PIC simulations during bunch compression with doubled beam intensity. (Shaded area denotes the range from $k_y = 90°$ to $\hat{k}_y = 90°$.)

individual particle (marked as i^{th}, with its phase advances k_y^i) will arrive at the 90° line before turn 71 when satisfying

$$4k_y^i = 360° \quad (k_y \geq k_y^i \geq \hat{k}_y). \tag{7.14}$$

This leads to the fourth-order resonance of the i^{th} particle and contributes to the initial emittance growth.

In order to further study the mechanism of the 90°-related intensity limitation, and distinguish the role of fourth-order resonance and envelope instability during bunch compression, we calculate the envelope modes (the fast mode φ_1, the slow mode φ_2) and dispersion mode φ_d [4] during bunch compression from the coupled envelope model, as shown in Fig. 7.11. With space charge increasing, φ_2 will drop and lock on the 180° line after turn 72 when $k_y < 90°$, indicating the occurrence of envelope

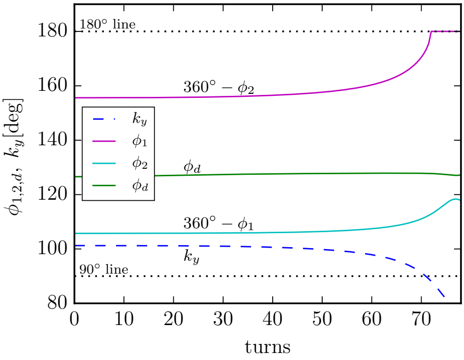

Figure 7.11.: Phase shifts of the envelope modes $\varphi_{1,2}$ and the dispersion mode φ_d numerically solved from the coupled envelope approach during bunch compression

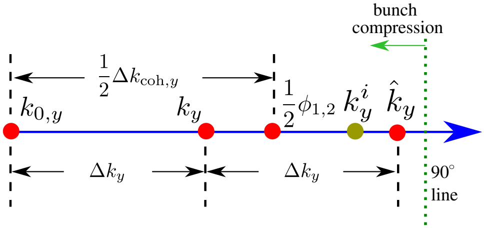

Figure 7.12.: Schematic drawing of the comparison on location of the phase advances shown in Fig. 7.9 to the phase shifts of envelope modes $\varphi_{1,2}$. Dashed line denotes the 90° phase advance line (in Fig. 7.10) during bunch compression.

instability. However, simulation results in Fig. 7.8 show that from turn 72 to turn 76 only the fourth-order resonance is observed. It is pointed out in Ref. [20] that for a well-matched Gaussian beam transported for a short distance the fourth-order resonance can dominate over the envelope instability, since the fourth-order resonance readily occurs from the beginning due to the presence of the “pseudo-octupole” in the initial density profile. In contrast, for the envelope instability, it takes more time to “amplify” the initial noise and develop the collective instability.

To illustrate this, we add in Fig. 7.9 the phase shifts of envelope modes $\varphi_{1,2}$ and the coherent space charge tune shift $\Delta k_{\mathrm{coh},y}$ obtained from envelope approach, and replot Fig. 7.9 as Fig. 7.12. The envelope instability in Fig. 7.11 can be described as

$$\varphi_2 = 2k_{0,y} - \Delta k_{\mathrm{coh},y} = \frac{1}{2}360°. \tag{7.15}$$

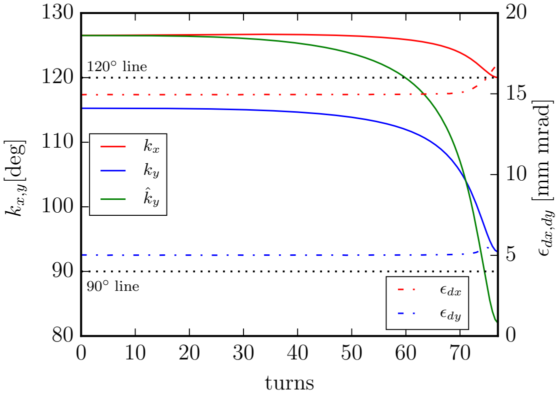

Figure 7.13.: Space-charge depressed phase advances $k_{x,y}$ (solid line) solved from the coupled envelope approach and emittance growth $\epsilon_{dx,dy}$ (dashed line) from PIC simulations during bunch compression with doubled beam intensity and $k_{0,x} = 128°$, $k_{0,y} = 118°$.

During bunch compression, with space charge increasing, all quantities except $k_{0,y}$ in Fig. 7.12 will decrease and dynamically move towards the 90° line. Clearly, the most depressed phase advance $\hat{k}_y$ will firstly arrive at the 90° line. Then particles with k_y^i in the region of $\frac{1}{2}\varphi_2 < k_y^i < \hat{k}_y$ can trigger the fourth-order resonance before $\frac{1}{2}\varphi_2$ arrives at the 90° line. The resulting emittance growth can weaken the space charge effect and prevent $\frac{1}{2}\varphi_2$ to approach the 90° line. In other words, individual particles can firstly arrive at the 90° resonance line, leading to the fourth-order resonance and prevent inducing the envelope instability.

In order to avoid the onset of the fourth-order resonance under the intensity of $N = 2 \times 10^{11}$, we adjust the vertical phase advance from $k_{0,y} = 104°$ to 118°. In Fig. 7.10 show the emittance growths from simulation and space-charge modified phase advances from the coupled envelope equations. The phase advance k_y solved from envelope approach stays above 90°, and the vertical emittance almost remains constant. From turn 74, the slight emittance growth is from those particles with $\hat{k}_y < 90°$. It is worthing pointing out that in both Fig. 7.10 and Fig. 7.13, slight increase of ϵ_{dx} (10%) can be observed. We attribute this to the same reason as observed in Fig. 7.6: the residual dispersive emittance growth. Clearly, with doubled beam intensity, the residual dispersive emittance growth (13%) is much larger compared to the one (1%) in Fig. 7.6 because of the enhanced space charge effects.

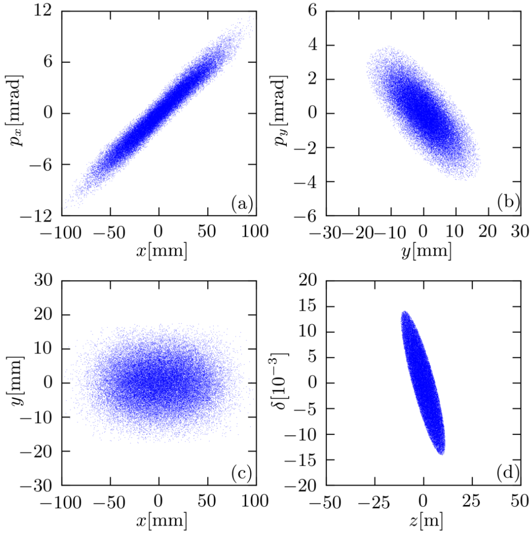

Figure 7.14.: Particle distribution in (a) x-x' phase space; (b) y-y' phase space; (c) x-y real space and (d) longitudinal z-δ phase space at 70th turn during bunch compression, with $k_{0,x} = 122°, k_{0,y} = 104°$.

7.3.2 120°-related Intensity Limitation

During bunch compression space charge as well as dispersion are increasing. With sufficiently high beam intensity and designed horizontal phase advance $k_{0,x}$ larger than 120°, as is the case for SIS-18, the combined effects of space charge and dispersion could induce the 120° dispersion instability, which is another limitation factor for bunch compression. In order to investigate this, we adjust $k_{0,x}$ from 128° to 122° in Tab. 7.1 and keep other parameters unchanged. By doing this, the horizontal phase advance k_x will cross the 120° line during bunch compression.

Particle distributions at turn 70 from PIC simulation are plotted in Fig. 7.14, which is similar to the case in Fig. 7.3, and no evident emittance growth has occurred up to this point. Fig. 7.15 shows the result of depressed phase advances by solving the coupled envelope equation of Eqs.11 with $k_{0,x} = 122°$, $k_{0,y} = 104°$. As can be seen, during bunch compression k_y is always above 90° while k_x crosses the 120° line after 70th turn.

Particle distributions in $x - p_x$ phase space at three representative turns (72nd, 74th, and 76th) are shown in Fig. 7.16, from which one can see the emittance deformation and the effect of emittance growth.

The evolution of transverse emittance in simulation during bunch compression is shown as dashed line in Fig. 7.15. Note that sharp increasing of the emittance occurs

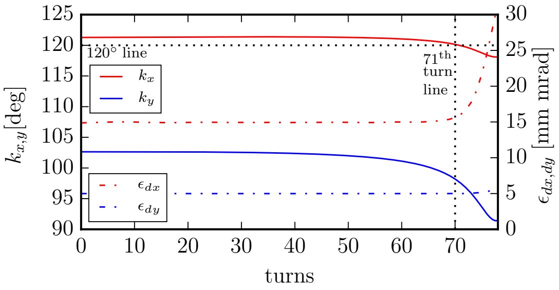

Figure 7.15.: Space-charge depressed phase advances $k_{x,y}$ (solid line) obtained from the coupled envelope approach and emittance growth $\epsilon_{dx,dy}$ (dashed line) from PIC simulations during bunch compression with $k_{0,x} = 122°$ and $k_{0,y} = 104°$.

starting from turn 72. This is different from the case when crossing the 90° resonance line in Fig. 7.10, in which emittance growth occurs much earlier than $k_y = 90°$. We attribute this difference to the reason that the emittance growth in Fig. 7.14 is from the 120° dispersion instability, which is a collective effect with,

$$\varphi_1 + \varphi_d = 360°, \tag{7.16}$$

when

$$k_{0,x} > 120° \quad \text{and} \quad k_x < 120°. \tag{7.17}$$

The emittance growth observed in Fig. 7.15 must be distinguished from the residual dispersive growth of ϵ_{dx} appeared in Fig. 7.6, Fig. 7.10 and Fig. **??**. The point is that, with the same beam intensity, the horizontal emittance growth (100%) in Fig. 7.15 is much larger than that in Fig. 7.6 (1%), Fig. 7.6 (13%) and Fig. 7.10 (13%), and can be explained only by the dispersion-induced instability. Moreover, the dispersive emittance growth is characterized by an extension of emittance along the slope of the ellipse of the emittance in the $x-x'$ plane, as shown in Fig. 7.3 and Fig. 7.14. In comparison, the evolution of particle distribution in Fig. 7.16 has no such regular extension and behaves like the emittance growth during the envelope instability (for example, see the figures in [17] and Fig.2 in [20]).

In order to further study the mechanism of 120°-related intensity limitation, we calculate the fast mode φ_1, slow mode φ_2 and dispersion mode φ_d with $k_{0,x} = 122°$, $k_{0,y} = 104°$. As shown in Fig. 7.17, with space charge increasing during bunch compression, the curve φ_d will be confluent with $360° - \varphi_1$, indicating the dispersion-instability, which is in good agreement with the sharp emittance growth at turn 71 in Fig. 7.15.

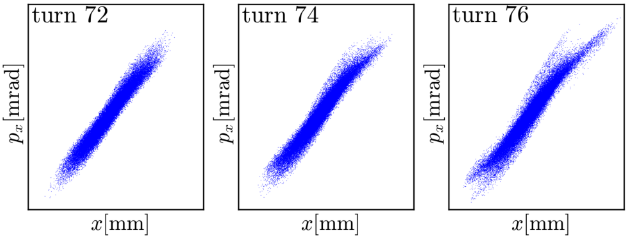

Figure 7.16.: The evolution of particle distribution in the $x - x'$ phase space at final stage of bunch compression with $k_{0,x} = 122°$, $k_{0,y} = 104°$ at 72th, 74th, 76th turns during bunch compression.

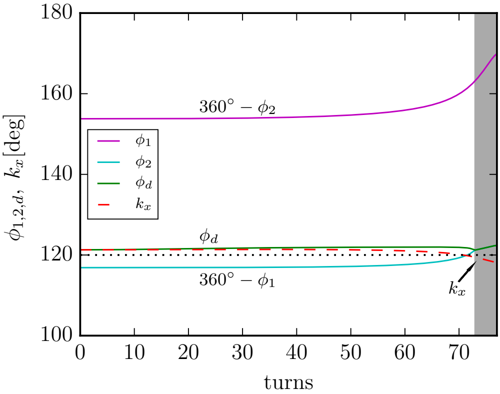

Figure 7.17.: Phase shifts of the envelope modes φ_1, φ_2 and dispersion mode φ_d numerically solved from the coupled envelope approach during bunch compression with $k_{0,x} = 122°$ and $k_{0,y} = 104°$. (Shaded area denotes the stop band of the dispersion-induced instability.)

The onset of the dispersion-induced instability is not inhibited compared with that of the envelope instability. Firstly, compared with the competition between fourth-order resonance and envelope instability related to 90°, there is no obvious single particle resonance, which exists earlier and can weaken the space charge and prevent the 120° dispersion instability. This is different from the case of the 90° envelope instability, which is suppressed by the competition with the fourth-order resonance. Secondly, the beam intensity threshold of 120° dispersion instability is much lower than that of 90° envelope instability, as can be seen in the Fig.2 in Ref. [4]. Therefore, the former instability would need less time to develop than the latter.

8 Conclusions and Outlook

8.1 Conclusions

The present work in this thesis focus on a detailed study of intense beam motion and transverse instabilities in synchrotrons, in which the role of dispersion is fully taken into beam coherent motion. By a generalized envelope equations including space-charge modified dispersion function, important properties of dispersion under the influence of space charge are discussed. Moreover, a rms-matched particle distribution with dispersion and space charge is introduced and employed in simulation in this work.

Full numerical solutions of the generalized envelope equations and the oscillation model shows that a coherent dispersion mode exists, besides the well-know slow and fast envelope modes. For phase advances larger than 120° and lattice parameters similar to modern high-intensity synchrotrons, we find that the dispersion mode is unstable and induce a novel beam instability - dispersion-induced instability. Our analysis reveals that this new instability in periodic focusing lattices is characterized by the confluence of the fast mode or slow envelope mode (i.e. the second order even mode) with the dispersion mode. PIC simulations using pyORBIT are performed to support the theory of dispersion mode and the dispersion-induced instability and shows good agreement.

Another important study in this thesis is that complete set of second order instantiates. The linearized second order moment equations derived from Chernin's equations offer a unified framework to study the stability properties of all possible second order modes, even and odd ones, in constant or periodic focusing quadrupole lattices without bending. Results are compared with earlier results on mode frequencies obtained from the linearized Vlasov-Poisson equation. Excellent agreement is found in the case of the tilting instability of odd (skew) modes in anisotropic beams and constant focusing, which confirms the equivalence of both models - on the level of second order perturbations. Comparing moment spectra from the perturbation equations with PIC spectra for KV and waterbag beams, peaks pertaining to odd modes are retrieved at similar locations. Hence this suggests that these modes also exist for more realistic beam distributions, like waterbag. In periodic focusing structures the stop bands of the parametric coupled even mode sum instability and the skew mode sum instability are obtained and found in very good agreement with PIC simulations, which completes the picture of second order coherent modes in 2d high intensity beams.

As an application, we apply the theory above to study the bunch compression in circular accelerators, where both dispersion and space charge play important roles. Taking the SIS-18 in GSI as an example, the beam dynamics during bunch compression has been investigated. In order to study the beam current limitation during bunch compression, several possible beam instabilities related to phase advance of 90° and 120° during bunch compression are discussed. Detailed simulation reveals the mechanism of the beam instability during bunch compression and give the method to avoid beam instabilities.

8.2 Outlook

We expect that the coherent dispersion mode and its instability will have implications for the choice of the working point in high intensity circular accelerators. An important application would be the experimental identification of the space charge modified dispersion mode from the transverse beam spectra: The observation of the dispersion mode could be a method to dynamically characterize the space-charge-modified dispersion. Measurements in circular accelerators could take advantage of quadrupolar pickup signals to identify the envelope modes [79, 80] and the new coherent dispersion mode, which would give a full dynamical characterization of the relevant optical functions modified by space charge. Furthermore, the identified 120° stop band could be avoided during bunch compression [45, 81, 47] in synchrotrons and might play a role in ERLs and recirculators.

The rms-matched distribution and the generalized envelope equation set including dispersion and the corresponding envelope oscillation equitations could be employed as two complementary methods to investigate beam dynamics with space charge and dispersion.

The dispersion mode introduced here could trigger further studies of confluence with other modes [1, 73, 24]. Furthermore, the role of synchrotron motion on this new instability in bunched beams deserves additional study. Future studies also might have to include the effects of external skew magnets as well as of synchrotron motion. Correlations with the recently discovered instabilities induced by the dispersion mode in bent lattices also warrant further work.

A The rms envelope equations

In the presence of space charge, the equations of transverse motion of a single particle can be written as

$$\begin{aligned} x'' + \kappa_{x0} - f_x &= 0, \\ y'' + \kappa_{y0} - f_y &= 0, \end{aligned} \tag{A.1}$$

where the space charge forces $f_{x,y} = qE_{x,y}/mc^2\gamma^3\beta^2$. Following the original work by Lapostolle and Sacherer, from Eq. A.1 we have

$$\langle xx'' \rangle + \kappa_{x0}\sigma_x^2 - \langle f_x x \rangle = 0. \tag{A.2}$$

By using the relations

$$\begin{aligned} (\sigma_x^2)'' &= 2(\sigma_x\sigma_x'' + \sigma_x'^2), \\ \langle xx' \rangle' &= \sigma_x'^2 + \langle xx'' \rangle, \end{aligned} \tag{A.3}$$

Eq. A.2 is equivalent to

$$\sigma_x\sigma_x'' + \frac{\langle xx' \rangle^2}{\sigma_x^2} - \frac{\langle x'^2 \rangle \langle x^2 \rangle}{\sigma_x^2} + \kappa_{x0}\sigma_x^2 - \langle xf_x \rangle = 0. \tag{A.4}$$

Following the definition of rms emittance in Eq. 3.16, we obtain

$$\sigma_x'' + \kappa_{x0}\sigma_x - \frac{\tilde{\epsilon}_x^2}{\sigma_x^3} - \frac{\langle xf_x \rangle}{\sigma_x} = 0. \tag{A.5}$$

Similar equations can be obtained in y-direction.

An important contribution by Sacherer is that the term $\langle x f_x \rangle$ in the above equation is independent of the type of particle distributions and has the same value as for the distributions, which has the same rms transverse beam size, i.e.,

$$\langle x f_x \rangle = \frac{K_{\mathrm{sc}}}{2} \frac{\sigma_x}{\sigma_x + \sigma_y}, \tag{A.6}$$

$$\langle x f_x \rangle + \langle y f_y \rangle = \frac{K_{\mathrm{sc}}}{2}. \tag{A.7}$$

With above relations, the rms envelope equations take the form

$$\begin{aligned} \sigma_x'' + \kappa_{x0}(s)\sigma_x - \frac{K_{sc}}{2(\sigma_x + \sigma_y)} - \frac{\tilde{\epsilon}_x^2}{\sigma_x^3} &= 0, \\ \sigma_y'' + \kappa_{y0}(s)\sigma_y - \frac{K_{sc}}{2(\sigma_x + \sigma_y)} - \frac{\tilde{\epsilon}_y^2}{\sigma_y^3} &= 0. \end{aligned} \tag{A.8}$$

B The envelope modes of mismatch oscillation

In the framework of Ref. [17], the two modes can be obtained via firstly solving numerically Eqs. 3.19, from which the matched solution used as coefficients in Eqs. 3.26, and secondly fundamental modes can be found via the method of solution matrix. In the following, we will adopt another method to solve the perturbation system in Eqs. 3.26.

For brevity, the coupled system in Eqs. 3.26 can be rewritten as

$$\begin{aligned} \xi'' + a_1\xi + a_2\zeta &= 0, \\ \zeta'' + a_3\zeta + a_2\xi &= 0, \end{aligned} \tag{B.1}$$

with the coefficients

$$\begin{aligned} a_1 &= \kappa_{x0} + \frac{K_{\mathrm{sc}}}{2(\sigma_{x0}+\sigma_{y0})^2} + \frac{3\tilde{\epsilon}_x^2}{\sigma_{x0}^4}, \\ a_2 &= \frac{K_{\mathrm{sc}}}{2(\sigma_{x0}+\sigma_{y0})^2}, \\ a_3 &= \kappa_{y0} + \frac{K_{\mathrm{sc}}}{2(\sigma_{x0}+\sigma_{y0})^2} + \frac{3\tilde{\epsilon}_y^2}{\sigma_{y0}^4}. \end{aligned} \tag{B.2}$$

We assume a set of variables (p_1, p_2) to represent the envelope oscillation in the decoupled form,

$$\begin{aligned} p_1'' + k_1 p_1 &= 0, \\ p_2'' + k_2 p_2 &= 0, \end{aligned} \tag{B.3}$$

through a coordinate rotation on the variables (ξ, ζ),

$$\begin{pmatrix} p_1 \\ p_2 \end{pmatrix} = \begin{pmatrix} \cos\vartheta & \sin\vartheta \\ -\sin\vartheta & \cos\vartheta \end{pmatrix} \begin{pmatrix} \xi \\ \zeta \end{pmatrix}. \tag{B.4}$$

Here k_1 and k_2 denote the angular frequencies of the fundamental modes, and ϑ the rotation angle. Combining Eqs. B.4 and Eqs. B.3, we have

$$\begin{aligned} \xi'' + (k_1 \sin^2\vartheta + k_2 \cos^2\vartheta)\zeta + (k_1 - k_2)\sin\vartheta\cos\vartheta\zeta = 0, \\ \zeta'' + (k_1 \sin^2\vartheta + k_2 \cos^2\vartheta)\zeta + (k_1 - k_2)\sin\vartheta\cos\vartheta\xi. \end{aligned} \tag{B.5}$$

The mode frequencies k_1, k_2 can be determined by comparing the coefficients of above equations with the coefficients in Eq. B.1:

$$\begin{aligned} k_1 \cos^2\vartheta + k_2 \sin^2\vartheta = a_1, \\ (k_1 - k_2)\sin\vartheta\cos\vartheta = a_2, \\ k_1 \sin^2\vartheta + k_2 \cos^2\vartheta = a_3. \end{aligned} \tag{B.6}$$

Here k_1, k_2 and ϑ are the unknown variables, and can be easily obtained.

For the case of a round beam with $\sigma_{x0} = \sigma_{y0}$, and $\tilde{\epsilon}_x = \tilde{\epsilon}_y$ transporting in a symmetric channel with $\kappa_{x0} = \kappa_{y0} = \kappa_0$, it can be calculated from Eqs. B.6 that $\vartheta = \pi/4$, and the fundamental modes are given in [17]

$$k_1 = \sqrt{k_0^2 + 3k^2}, \qquad k_2 = \sqrt{2k_0^2 + 2k^2}. \tag{B.7}$$

Here k_0 and k is the phase advance without and with space charge, respectively. k_1 and k_2 are well-known as breathing mode and quadrupole mode.

C The movements of eigenvalues

Fig. C.1 illustrates the movements of the four eigenvalues of the perturbation map of Eq. 3.29, for the case of a round beam travelling in an alternating gradient channel with the phase advance $k_{0,x} = k_{0,y} = 60°$. The two arrows in the upper half complex plane denotes the two envelopes, with their conjugate counterpart existing in the lower half plane. In the absence of space charge ($\eta_x = 1.0$), the two eigenvalues lie on unit circle and are overlapped. and no envelope instability occur. As beam current increasing, the phase shifts of the two modes start to move and are seperated (see the subplot with $\eta_x = 0.1$). As the beam current keeps increasing, the phase shifts of the slow mode are equal to the one of fast mode, indicating the occurrence of the envelope instability (see the subplot with $\eta_x = 0.22$). For strong space charge ($\eta_x = 0.34$), the two modes separates from each other again.

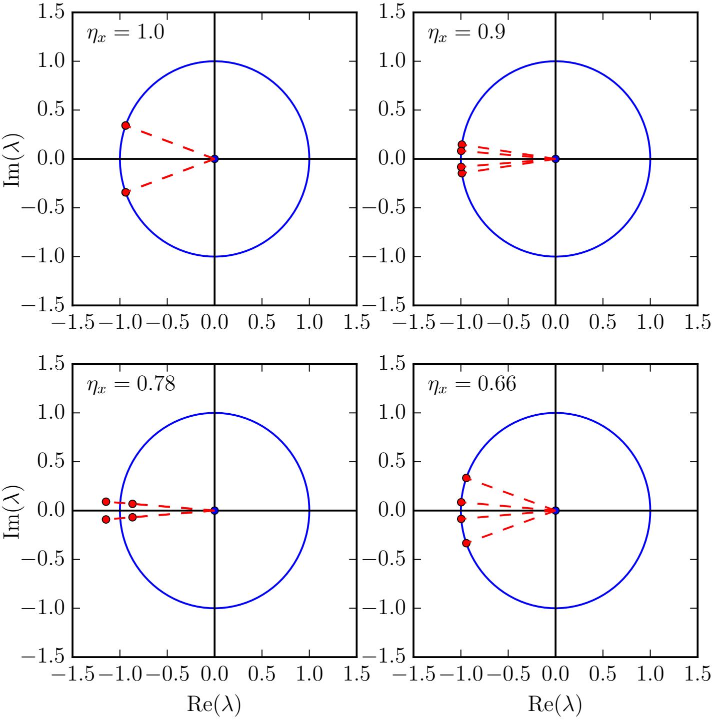

Figure C.1.: Movement of the eigenvalues λ with increasing beam intensity for $k_0 = 60°$ case in four representative cases: $\eta_x = 0.0,\ 0.1,\ 0.22,\ 0.34$.

D Equations of second-moment oscillations

For a slightly mismatched case the moments can be written as $\Sigma(s) = \Sigma_0(s) + \Sigma_p(s)$ ("p" denoting a small perturbation of the matched solution). After Taylor expanding and keeping only first order terms we have

$$\boldsymbol{\Sigma' = (\Sigma_0 + \Sigma_p)' = G(\Sigma_0) + J(\Sigma_p)}, \tag{D.1}$$

which can be seperated into two parts

$$\boldsymbol{\Sigma_0{}' = G(\Sigma_0), \qquad \Sigma_p' = J(\Sigma_0)\Sigma_p}. \tag{D.2}$$

Here J represents the Jacobian matrix of G with elements $J_{k,l} = \partial G_k(\Sigma_l)/\partial \Sigma_l$ (k, l run from 1 to 10 along the possible combinations of the second order moments Σ_{ij}.).

Next we consider a lattice without external coupling force ($q_{xy,0} = 0$). Furthermore, we note that the moments Σ_{22} and Σ_{44} can be replaced by the rms emittance with $\varepsilon_x = \sqrt{\Sigma_{11}\Sigma_{22} - \Sigma_{12}^2}$ and $\varepsilon_y = \sqrt{\Sigma_{33}\Sigma_{44} - \Sigma_{34}^2}$ [13]. With these conditions the equations of the matched moments in Eqs. D.2 can be simplified to

$$\begin{aligned}
\Sigma_{11}' &= 2\Sigma_{12} = G_1,\\
\Sigma_{12}' &= \frac{\epsilon_x^2 + \Sigma_{12}^2}{\Sigma_{11}} - k_x\Sigma_{11} = G_2,\\
\Sigma_{13}' &= \Sigma_{23} + \Sigma_{14} = G_3,\\
\Sigma_{14}' &= \Sigma_{24} - k_y\Sigma_{13} + q_{xy}\Sigma_{11} = G_4,\\
\Sigma_{23}' &= \Sigma_{24} - k_x\Sigma_{13} + q_{xy}\Sigma_{33} = G_5,\\
\Sigma_{24}' &= -k_x\Sigma_{14} - k_y\Sigma_{23} + q_{xy}(\Sigma_{12} + \Sigma_{34}) = G_6,\\
\Sigma_{33}' &= 2\Sigma_{34} = G_7,\\
\Sigma_{34}' &= \frac{\epsilon_y^2 + \Sigma_{34}^2}{\Sigma_{33}} - k_y\Sigma_{33} = G_8.
\end{aligned} \tag{D.3}$$

Here G_1 to G_8 denote the row elements of the matrix G, respectively. For the matched case we assume that the coupling moments are zero: $\Sigma_{13,0} = \Sigma_{14,0} = \Sigma_{23,0} = \Sigma_{24,0} = 0$ [82] (In Ref. [82], it is alternatively assumed that non-zero value for $\Sigma_{14,0}$ and $\Sigma_{23,0}$ with $\Sigma_{14,0} = -\Sigma_{23,0}$), and Eqs. D.2 are simplified to the envelope equations

$$\begin{aligned}
\Sigma'_{11,0} &= 2\Sigma_{12,0},\\
\Sigma'_{12,0} &= \frac{\epsilon_x^2 + \Sigma_{12,0}^2}{\Sigma_{11,0}} - k_x\Sigma_{11,0},\\
\Sigma'_{33,0} &= 2\Sigma_{34,0},\\
\Sigma'_{34,0} &= \frac{\epsilon_y^2 + \Sigma_{34,0}^2}{\Sigma_{33,0}} - k_y\Sigma_{33,0},
\end{aligned} \tag{D.4}$$

with the corresponding perturbation equations

$$\begin{aligned}
\Sigma_{11}^{p\ \prime} &= 2\Sigma_{12}^p\\
\Sigma_{12}^{p\ \prime} &= \Big(\frac{\partial G_2}{\partial \Sigma_{11}}\Big)_0\Sigma_{11}^p + \Big(\frac{\partial G_2}{\partial \Sigma_{12}}\Big)_0\Sigma_{12}^p + \Big(\frac{\partial G_2}{\partial \Sigma_{33}}\Big)_0\Sigma_{33}^p\\
\Sigma_{33}^{p\ \prime} &= 2\Sigma_{34}^p\\
\Sigma_{34}^{p\ \prime} &= \Big(\frac{\partial G_8}{\partial \Sigma_{11}}\Big)_0\Sigma_{11}^p + \Big(\frac{\partial G_8}{\partial \Sigma_{33}}\Big)_0\Sigma_{33}^p + \Big(\frac{\partial G_8}{\partial \Sigma_{34}}\Big)_0\Sigma_{34}^p
\end{aligned} \tag{D.5}$$

The two second order even modes (fast and slow modes) φ_1, φ_2 can be obtained from the above equations.

In order to calculate the odd modes, we need to derive the perturbation equations of coupling moments. Based on Eqs. D.3 we obtain

$$\begin{aligned}
\Sigma_{13}^{p\ \prime} &= \Sigma_{14}^p + \Sigma_{23}^p,\\
\Sigma_{14}^{p\ \prime} &= \Big(\frac{\partial G_4}{\partial \Sigma_{13}}\Big)_0\Sigma_{13}^p + \Sigma_{24}^p,\\
\Sigma_{23}^{p\ \prime} &= \Big(\frac{\partial G_5}{\partial \Sigma_{13}}\Big)_0\Sigma_{13}^p + \Sigma_{24}^p,\\
\Sigma_{24}^{p\ \prime} &= \Big(\frac{\partial G_6}{\partial \Sigma_{13}}\Big)_0\Sigma_{13}^p + \Big(\frac{\partial G_6}{\partial \Sigma_{14}}\Big)_0\Sigma_{14}^p + \Big(\frac{\partial G_6}{\partial \Sigma_{23}}\Big)_0\Sigma_{23}^p.
\end{aligned} \tag{D.6}$$

Note that in the matched case, $\Sigma_{13,0} = \Sigma_{14,0} = \Sigma_{23,0} = \Sigma_{24,0} = 0$, and from Eqs. 5.3 and Eqs. 5.4 we have

$$\begin{aligned} &(\frac{\partial \Delta q_{xy}}{\partial \Sigma_{11}})_0 = (\frac{\partial \Delta q_{xy}}{\partial \Sigma_{33}})_0 = 0, \\ &\frac{\partial \Delta q_{xy}}{\partial \Sigma_{13}} = \frac{K}{2} \frac{1}{S_0(S_x + S_y)}. \end{aligned} \tag{D.7}$$

The Eqs. D.7 mean that the space charge coupling term has no influence on the matched solution, but on the perturbation second order odd modes. With the matched beam moments from Eqs. D.4, the perturbations in Eqs. D.5 and Eqs. D.6 can be used to calculate the two even as well as the two odd modes.

E Partial derivatives of the Jacobian matrix

In the absence of the external skew focusing strength, the partial derivatives of the Jacobian with respect to second moments takes a simplified form, listed in the following tables.

	∂G_1	∂G_2	∂G_3	∂G_4
$\partial \Sigma_{11}$	0	$-\frac{\epsilon_x^2+\Sigma_{12}^2}{\Sigma_{11}^2} - k_x + \Sigma_{11}\frac{\partial q_{xx}}{\partial \Sigma_{11}}$	0	$\Sigma_{13}\frac{\partial q_{yy}}{\partial \Sigma_{11}}$
$\partial \Sigma_{12}$	2	$\frac{2\Sigma_{12}}{\Sigma_{11}}$	0	0
$\partial \Sigma_{13}$	0	0	0	$-k_y$
$\partial \Sigma_{14}$	0	0	1	0
$\partial \Sigma_{23}$	0	0	1	0
$\partial \Sigma_{24}$	0	0	0	1
$\partial \Sigma_{33}$	0	$\Sigma_{11}\frac{\partial q_{xx}}{\Sigma_{33}}$	0	$\Sigma_{13}\frac{\partial q_{yy}}{\partial \Sigma_{33}}$
$\partial \Sigma_{34}$	0	0	0	0

	∂G_5	∂G_6	∂G_7	∂G_8
$\partial \Sigma_{11}$	$\Sigma_{13}\frac{\partial q_{xx}}{\partial \Sigma_{11}}$	$\Sigma_{14}\frac{\partial q_{xx}}{\partial \Sigma_{11}} + \Sigma_{23}\frac{\partial q_{yy}}{\partial \Sigma_{11}}$	0	$\Sigma_{33}\frac{\partial q_{yy}}{\partial \Sigma_{11}}$
$\partial \Sigma_{12}$	0	0	0	0
$\partial \Sigma_{13}$	$-k_x$	0	0	0
$\partial \Sigma_{14}$	0	$-k_x$	0	0
$\partial \Sigma_{23}$	0	$-k_y$	0	0
$\partial \Sigma_{24}$	1	0	0	0
$\partial \Sigma_{33}$	$\Sigma_{13}\frac{\partial q_{xx}}{\partial \Sigma_{33}}$	$\Sigma_{14}\frac{\partial q_{xx}}{\partial \Sigma_{33}} + \Sigma_{23}\frac{\partial q_{yy}}{\partial \Sigma_{33}}$	0	$-\frac{\epsilon_y^2+\Sigma_{34}^2}{\Sigma_{33}^2} - k_y + \Sigma_{33}\frac{\partial q_{yy}}{\partial \Sigma_{33}}$
$\partial \Sigma_{34}$	0	0	2	$\frac{2\Sigma_{34}}{\Sigma_{33}}$

F Space-charge-modified dispersion

In the following we assume x and y are the transverse degrees in horizontal and vertical direction respectively; s the longitudinal coordinate; and $k_{0,x,y}$, $k_{x,y}$ are the phase advance per periodic focusing cell without and with space charge, respectively; the dispersion effect acts on x and there is no rf focusing or acceleration process in longitudinal direction.

Consider a coasting beam transporting in a periodic focusing channel with dipoles. For simplicity, here we ignore any imperfection of the periodic channel and any nonlinear effect due to external focusing, as well as all the chromatic terms. The Hamiltonian of such a system can be expressed as

$$H = \frac{1}{2}(p_x^2 + p_y^2) + \frac{\kappa_{x0}(s)}{2}x^2 + \frac{\kappa_{y0}(s)}{2}y^2 + \frac{m^2c^4}{E_0^2}\delta^2 - \frac{x}{\varrho(s)}\delta + V_{\text{sc}}(x,y,s), \tag{F.1}$$

where $\kappa_{x0}(s), \kappa_{y0}(s)$ denote the focusing gradients; $\varrho(s)$ the radius of curvature; $\delta = (p - p_0)/p_0$ the fractional momentum deviation from the design momentum p_0 with E_0 being the corresponding energy and V_{sc} the space charge potential. With canonical transformation introduced in the V-R and L-O frameworks [29, 2]: $x = \bar{x} + \delta D_x$, $x' = \bar{x}' + \delta D_x'$, $y = \bar{y}$, $y' = \bar{y}'$, we introduce $\bar{x}$ and $\bar{x}'$ as the betatron coordinates affected by space charge, and $D_x\delta$, $D_x'\delta$ the off-momentum coordinate affected by space charge. Here the prime " $'$ " denotes the derivative with respect to s. The coefficients D_x and D_x' will later be identified with the space-charge-modified dispersion and its derivative. The Hamiltonian in Eq. F.1 refers to the integration of the motion of *individual* particle. In order to study the *collective* (coherent) motion of the beam, we derive the second momentum distribution of $\bar{x}$ from Eq. F.1:

$$\sigma_x\sigma_x'' + \frac{\langle\bar{x}\bar{x}'\rangle^2}{{\sigma_x}^2} - \langle\bar{x}'^2\rangle + \sigma_\delta^2 D_x D_x'' + \kappa_{x0}\sigma_x^2 + \kappa_{x0}\sigma_\delta^2 D_x^2 - \langle x\frac{\partial V_{\text{sc}}}{\partial x}\rangle = \frac{D_x\sigma_\delta^2}{\varrho}, \tag{F.2}$$

and

$$\sigma_y\sigma_y'' + \frac{\langle yy'\rangle^2}{{\sigma_y}^2} - \langle y'^2\rangle + \kappa_{y0}\sigma_y^2 - \langle y\frac{\partial V_{\text{sc}}}{\partial y}\rangle = 0. \tag{F.3}$$

in which $\langle\cdot\rangle$ denotes the averaging over phase space variables, and the second moments $\sigma_x = \sqrt{\langle\bar{x}^2\rangle}$, $\sigma_x' = \langle\bar{x}\bar{x}'\rangle/\sigma_x$, $\sigma_y = \sqrt{\langle\bar{y}^2\rangle} = \sqrt{\langle y^2\rangle}$ and $\sigma_\delta = \sqrt{\langle\delta^2\rangle}$.

Following Sacherer's approach [13], i.e., $\langle x\frac{\partial V_{\rm sc}}{\partial x}\rangle$ is independent of the form of particle distribution, we have:

$$\langle x\frac{\partial V_{\rm sc}}{\partial x}\rangle = \frac{K_{\rm sc}\sigma_x^2}{2X(X+Y)} + \frac{K_{\rm sc}\sigma_\delta^2 D_x^2}{2X(X+Y)} \tag{F.4}$$

with,

$$\langle x\frac{\partial V_{\rm sc}}{\partial x}\rangle = \langle \bar{x}\frac{\partial V_{\rm sc}}{\partial x}\rangle + D_x\langle \delta\frac{\partial V_{\rm sc}}{\partial x}\rangle, \tag{F.5}$$

which is correct in good approximation if the dispersive term of Eq. F.4 is not dominant. Here $X^2 = \sigma_x^2 + \sigma_\delta^2 D_x^2$ and $Y = \sigma_y$. $K_{\rm sc}$ is the space charge perveance defined by $K_{\rm sc} = 2N_L r_c/(\beta^2\gamma^3)$, with N_L the number of particles per length, r_c the classical proton radius, β and γ the relativistic factors. Eq. F.4 indicates that in the presence of dispersion, the beam coherent motion characterized by the second moments can be expressed as a linear superposition of two aspects: the betatron motion and the dispersion motion, independent of the form of particle distribution.

The space-charge-modified dispersion function can be defined in the combination of Eq. F.1 to Eq. F.5:

$$\frac{\mathrm{d}^2 D_x}{\mathrm{d}s^2} + \left[\kappa_{x0}(s) - \frac{K_{\rm sc}}{2X(X+Y)}\right] D_x = \frac{1}{\varrho(s)}, \tag{F.6}$$

with the corresponding rms envelope equations in the presence of both dispersion and space charge:

$$\frac{\mathrm{d}^2\sigma_x}{\mathrm{d}s^2} + \left[\kappa_{x0}(s) - \frac{K_{\rm sc}}{2X(X+Y)}\right]\sigma_x - \frac{\varepsilon_{dx}^2}{\sigma_x^3} = 0, \tag{F.7a}$$

$$\frac{\mathrm{d}^2\sigma_y}{\mathrm{d}s^2} + \left[\kappa_{y0}(s) - \frac{K_{\rm sc}}{2Y(X+Y)}\right]\sigma_y - \frac{\varepsilon_{dy}^2}{\sigma_y^3} = 0, \tag{F.7b}$$

where $\varepsilon_{dx} = \sqrt{\langle \bar{x}^2\rangle\langle \bar{x}'^2\rangle - \langle \bar{x}\bar{x}'\rangle^2}$ (similar in ε_{dy}), is the generalized rms emittance introduced in V-R and L-O theory, and can be defined by

$$\epsilon_x^2 = \epsilon_{dx}^2\left(\frac{X^2}{\sigma_x^2}\right) + \sigma_\delta^2(\sigma_x D_x' - \sigma_x' D_x)^2, \tag{F.8}$$

and $\varepsilon_y = \varepsilon_{dy}$. Here ε_x and ε_y are the rms transverse emittances usually used: $\varepsilon_x = \sqrt{\langle x^2\rangle\langle p_x^2\rangle - \langle x p_x\rangle^2}$ (similar for ε_y), which are not invariant in the presence of dispersion.

G The movements of eigenvalues with dispersion

In the presence of dispersion, the movement of eigenvalues of perturbation map in Eq. 6.20 for $k_0 = 120°$ case are discussed as follows with four representative cases: $\eta_x = 0.1,\ 0.25,\ 0.35,\ 0.6$. As shown in Fig. G.1, three arrows in the upper half complex plane denotes the three modes, with their conjugate counterpart existing in the lower half plane. For weak space charge with $\eta_x = 0.1$, all three eigen values lie on unit circle and no envelope instability occur. For $\eta_x = 0.25$, the fast mode is locked on the real axis ($\varphi_1 = 180°$), indicating parametric instability take place. With beam current go on increasing, the phase shifts of the slow mode are equal to the one of fast mode and the confluent resonance take places ($\varphi_1 = \varphi_2$). For strong space charge ($\eta_x = 0.6$), the two modes separates from each other again. Note that in the case of $k_0 = 120°$ the instabilities are triggered by either the unstable fast mode or the slow mode, and the dispersion mode keeps stable.

The movement of eigenvalues in $k_0 = 130°$ case are discussed as follows with six representative cases (see Fig. G.2): $\eta_x = 0.05,\ 0.1,\ 0.15,\ 0.25,\ 0.3,\ 0.35$. Beam starts with being stable under weak space charge ($\eta_x = 0.05$). With beam current increasing, the phase shift of dispersion mode will "catch up with" the one of slow mode and overlap with each other, indicating the occurrence of 120° dispersion instability (shown in the cases of $\eta_x = 0.1$ and $\eta_x = 0.15$). When beam current keeps on increasing, the slow mode becomes larger and gets separated from the dispersion mode ($\eta_x = 0.25$), until the fast mode reaches the 180° line ($\eta_x = 0.3$) which indicates that the occurrence of the usual 90° envelope instability triggered by parametric resonance takes place. Under stronger space charge effect ($\eta_x = 0.35$), the slow mode will overlap with the fast mode, indicating occurrence of the confluence resonance.

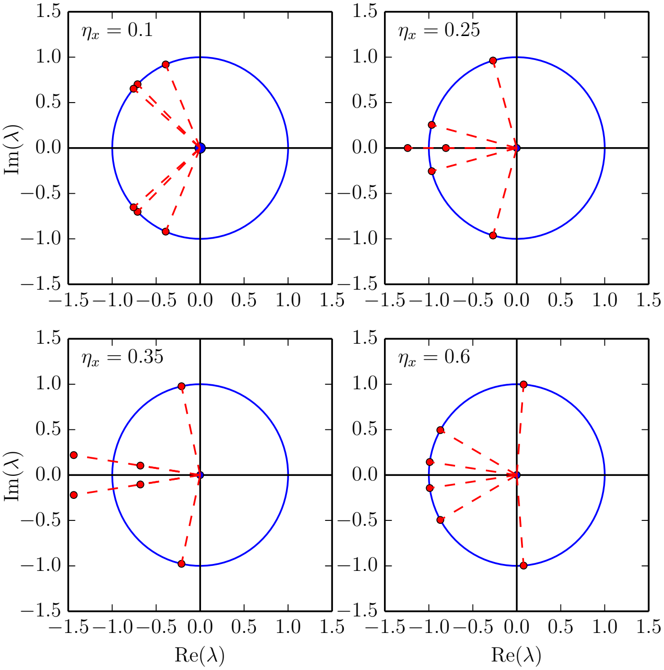

Figure G.1.: Movement of eigen value λ with increasing beam intensity for $k_0 = 120°$ case with dispersion in four representative cases: $\eta_x = 0.1,\ 0.25,\ 0.35,\ 0.6$.

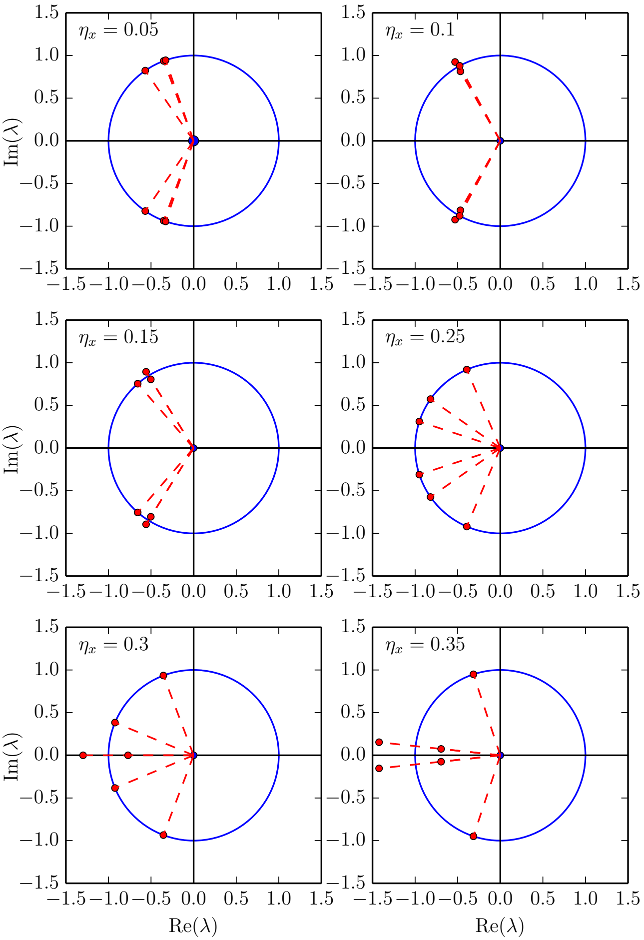

Figure G.2.: Movement of eigen value λ with increasing beam intensity for $k_0 = 130°$ case with dispersion in six representative cases: $\eta_x = 0.05,\ 0.1,\ 0.15,\ 0.25,\ 0.3,\ 0.35$.

H Lists

Acronyms

AGD	Alternative gradient focusing system with dispersion
CERN	Organisation européenne pour la recherche nucléaire
CFD	Constant gradient focusing system with dispersion
ERL	Energy recovery linac
FAIR	Facility for Antiproton and Ion Research in Europe GmbH
FFT	fast Fourier transformation
GSI	GSI Helmholtzzentrum für Schwerionenforschung GmbH
PIC	Particle In Cell
QD	Defocusing quadrupole
QF	Focusing quadrupole
rf	radio frequency
RMS	root mean square
SC	Space charge
SIS100	Schwerionensynchrotron 100 (heavy ion synchrotron)
SIS18	Schwerionensynchrotron 18 (heavy ion synchrotron)

Symbols

Term	Unit	Description
K_{sc}	1	transverse space charge perveance
m	kg	Rest mass

Term	Unit	Description
v	m/s	Particle velocity
τ	s	bunch compression time
λ	$1/m^3$	Line charge density
β	1	Relativistic velocity ($\beta = v/c_0$)
γ	1	Relativistic factor
p_0	$kg \cdot m/s$	Particle momentum
Δp	$kg \cdot m/s$	Particle momentum deviation
δ	1	Relative particle momentum deviation ($\delta = \Delta p/p_0$)
σ_δ	1	Rms value of relative particle momentum deviation
q	C	Charge of particle
$\vec{F}$	N	Force
$\vec{E}$	V/m	Electric field
$\vec{B}$	T	Magnetic flux density
t	s	Time
Z	1	Atomic number
ϱ	m	Bending radius in dipole magnets
x, y, s	m	Coordinates in the curvilinear coordinate system
σ_x, σ_y	m	Transvers rms betatron beam sizes
X, Y	m	Transvers rms total beam sizes
$\beta_0, \alpha_0, \gamma_0$	m	Lattice functions
$\epsilon_{x,y}$	m rad	Particle transverse emittances
$\tilde{\epsilon}_{x,y}$	m rad	RMS transverse emittances
ϵ_{dx}	m rad	Generalized horizontal emittances with dispersion
ϵ_L	m	Longitudinal emittance
L	m	Length of circular accelerator
$D_{0,x}$	m	Horizontal dispersion without space charge
D_x	m	Horizontal dispersion with space charge
α_c	1/m	Momentum compaction factor
γ_t	1	Relativistic factor at transition energy
η	1	Slip factor ($\eta = 1/\gamma_t^2 - 1/\gamma$)
c	m/s	Speed of light
V_{rf}	V	rf voltage
ΔU_{sc}	V	Longitudinal space charge induced voltage
h	1	Harmonic number ($h = \omega_{rf}/\omega_{rev}$)
ω_{rev}	1/s	Angular revolution frequency ($\omega_{rev} = 2\pi/T_{rev}$)
ω_s	1	Synchrotron frequency
Q_s	1	Synchrotron tune ($Q_s = \omega_s/\omega_{rev}$)
H	J	Transverse Hamiltonian
H_L	J	Longitudinal Hamiltonian

Term	**Unit**	**Description**
H_{sx}	J	Separatrix
$\kappa_{0,x}, \kappa_{0,y}$	$1/m^2$	Horizontal and vertical effective focusing strength
$k_{0,x}, k_{0,y}$	degree	Horizontal and vertical phase advance without space charge
k_x, k_y	degree	Horizontal and vertical phase advance without space charge
η_x, η_y	1	Horizontal and vertical space charge depressions
N	1	Number of particles
ξ, ζ, d_x	m	perturbations on rms beam sizes and dispersion
Σ	1	Second moments in matrix form
q_{xy0}	$1/m^2$	External linear coupling
q_{xy}	$1/m^2$	Space-charge modified external linear coupling
$\varphi_{1,2}$	degree	Phase shifts of the second order even modes (envelope modes)
$\psi_{1,2}$	degree	Phase shifts of the second order odd modes (skew modes)

List of Figures

List of Tables

Bibliography

[1] Ingo Hofmann. Stability of anisotropic beams with space charge. *Physical Review E*, 57(4), 1998. 1, 5, 51, 54, 56, 104

[2] S.Y. Lee and H. Okamoto. Space-charge dominated beams in synchrotrons. *Physical review letters*, 80(23):5133, 1998. 1, 5, 64, 115

[3] www.fair-center.eu. 1, 4, 124

[4] Y.S. Yuan, O. Boine-Frankenheim, G. Franchetti, and I. Hofmann. Dispersion-induced beam instability in circular accelerators. *Physical Review Letters*, 118(15):154801, 2017. 1, 57, 59, 63, 72, 73, 76, 95, 101

[5] D. Chernin. Evolution of rms beam envelopes in transport systems with linear xy coupling. *Part. Accel.*, 24:29–44, 1988. 2, 51, 52

[6] Yao-Shuo Yuan, Oliver Boine-Frankenheim, and Ingo Hofmann. Modeling of second order space charge driven coherent sum and difference instabilities. *Physical Review Accelerators and Beams*, 20(10):104201, 2017. 2

[7] Ernest D. Courant, M. Stanley Livingston, and Hartland S. Snyder. The strong-focusing synchroton - a new high energy accelerator. *Physical Review*, 88(5):1190, 1952. 2, 35

[8] Edwin M. McMillan. The synchrotron - a proposed high energy particle accelerator. *Physical Review*, 68(5-6):143, 1945. 2, 18

[9] Vladimir Isaakovich Veksler. A new method of acceleration of relativistic particles. *J. Phys.*, 9:153–158, 1945. 2, 18

[10] www.gsi.de. 4

[11] I.M. Kapchinskij and V.V. Vladimirskij. Limitations of proton beam current in a strong focusing linear accelerator associated with the beam space charge. In *Proceedings of the International Conference on High Energy Accelerators and Instrumentation*, page 274, 1959. 5, 29

[12] Pierre M. Lapostolle. Possible emittance increase through filamentation due to space charge in continuous beams. *IEEE Transactions on Nuclear Science*, 18(3):1101–1104, 1971. 5, 29, 33

[13] Frank J. Sacherer. Rms envelope equations with space charge. *IEEE Transactions on Nuclear Science*, 18(3):1105–1107, 1971. 5, 29, 33, 111, 116

[14] Robert L. Gluckstern. Analytic model for halo formation in high current ion linacs. *Physical review letters*, 73(9):1247, 1994. 5

[15] T.P. Wangler, K.R. Crandall, R. Ryne, and T.S. Wang. Particle-core model for transverse dynamics of beam halo. *Physical review special topics-accelerators and beams*, 1(8):084201, 1998. 5

[16] Chiping Chen and Ronald C Davidson. Nonlinear resonances and chaotic behavior in a periodically focused intense charged-particle beam. *Physical review letters*, 72(14):2195, 1994. 5

[17] J. Struckmeier, M. Reiser, and J. Klabunde. On the stability and emittance growth of different particle phase-space distributions in a long magnetic quadrupole channel. *Part. Accel.*, 15:47–65, 1984. 5, 38, 41, 57, 75, 99, 107, 108

[18] Steven M. Lund and Boris Bukh. Stability properties of the transverse envelope equations describing intense ion beam transport. *Physical Review Special Topics-Accelerators and Beams*, 7(2):024801, 2004. 5

[19] Chao Li and Ya Liang Zhao. Envelope instability and the fourth order resonance. *Physical Review Special Topics-Accelerators and Beams*, 17(12):124202, 2014. 5

[20] Ingo Hofmann and Oliver Boine-Frankenheim. Space-charge structural instabilities and resonances in high-intensity beams. *Physical review letters*, 115(20):204802, 2015. 5, 59, 96, 99

[21] Hung-Chun Chao and S.Y. Lee. Simulations of beam envelope dynamics in circular accelerators. *Physical Review Special Topics-Accelerators and Beams*, 18(2):024202, 2015. 5

[22] Oliver Boine-Frankenheim, Ingo Hofmann, and Jürgen Struckmeier. Parametric sum envelope instability of periodically focused intense beams. *Physics of Plasmas*, 23(9):090705, 2016. 5, 51, 57, 81

[23] Robert L. Gluckstern. Oscillation modes in two dimensional beams. Technical report, Univ. of Massachusetts, Amherst), 1970. 5

[24] I. Hofmann, G. Franchetti, O. Boine-Frankenheim, J. Qiang, and R.D. Ryne. Space charge resonances in two and three dimensional anisotropic beams. *Physical Review Special Topics-Accelerators and Beams*, 6(2):024202, 2003. 5, 57, 104

[25] Dong-O Jeon, Kyung Ryun Hwang, Ji-Ho Jang, Hyunchang Jin, and Hyojae Jang. Sixth-order resonance of high-intensity linear accelerators. *Physical review letters*, 114(18):184802, 2015. 5

[26] D. Jeon, L. Groening, and G. Franchetti. Fourth order resonance of a high intensity linear accelerator. *Physical Review Special Topics-Accelerators and Beams*, 12(5):054204, 2009. 5, 41

[27] L. Groening, W. Barth, W. Bayer, G. Clemente, L. Dahl, P. Forck, P. Gerhard, I. Hofmann, M.S. Kaiser, M. Maier, et al. Experimental evidence of the 90 stop band in the gsi unilac. *Physical review letters*, 102(23):234801, 2009. 5

[28] L. Groening, I. Hofmann, W. Barth, W. Bayer, G. Clemente, L. Dahl, P. Forck, P. Gerhard, M.S. Kaiser, M. Maier, et al. Experimental evidence of space charge driven emittance coupling in high intensity linear accelerators. *Physical review letters*, 103(22):224801, 2009. 5

[29] Marco Venturini and Martin Reiser. Rms envelope equations in the presence of space charge and dispersion. *Physical review letters*, 81(1):96, 1998. 5, 64, 87, 92, 115

[30] Marco Venturini and Martin Reiser. Self-consistent beam distributions with space charge and dispersion in a circular ring lattice. *Physical Review E*, 57(4):4725, 1998. 5

[31] S. Bernal, B. Beaudoin, T. Koeth, and P.G. O'Shea. Smooth approximation model of dispersion with strong space charge for continuous beams. *Physical Review Special Topics-Accelerators and Beams*, 14(10):104202, 2011. 5

[32] Masanori Ikegami, Shinji Machida, and Tomonori Uesugi. Particle-core analysis of dispersion effects on beam halo formation. *Physical Review Special Topics-Accelerators and Beams*, 2(12):124201, 1999. 5

[33] J.A. Holmes, V.V. Danilov, J.D. Galambos, D. Jeon, and D.K. Olsen. Space charge dynamics in high intensity rings. *Physical Review Special Topics-Accelerators and Beams*, 2(11):114202, 1999. 5, 70

[34] S. Cousineau, S.Y. Lee, J.A. Holmes, V. Danilov, and A. Fedotov. Space charge induced resonance excitation in high intensity rings. *Physical Review Special Topics-Accelerators and Beams*, 6(3):034205, 2003. 5, 70

[35] Oleksandr Chorniy, Oliver Boine-Frankenheim, Peter Hülsmann, and Peter J. Spiller. Fast compression of intense heavy-ion bunches in sis18. *Proc. of HB workshop*, 2010. 6, 88

[36] P. Hülsmann, R. Balss, U. Laier, and H. Klingbeil. Bunch compression for fair. In *Proceedings of the PAC*, volume 9, 2009. 6

[37] Oliver Boine-Frankenheim. The fair accelerators: highlights and challenges. *Proc. IPAC2010, Kyoto, Japan*, page 2430, 2010. 6

[38] K. Blasche, O. Boine-Frankenheim, H. Eickhoff, M. Emmerling, B. Franczak, I. Hofmann, K. Kaspar, U. Ratzinger, and P. Spiller. Bunch compression in the heavy ion synchrotron sis at gsi. In *Europ. Part. Acc. Conf., Stockholm, Sweden*, pages 1347–1349, 1998. 6

[39] S.M. Lund, O. Boine-Frankenheim, G. Franchetti, I. Hofmann, and P. Spiller. Simulations of axial bunch compression in heavy ion rings for plasma physics applications at gsi. In *Particle Accelerator Conference, 1999. Proceedings of the 1999*, volume 3, pages 1785–1787. IEEE, 1999. 6

[40] P. Spiller, J. Ahrens, K. Blasche, M. Emmerling, O. Boine-Frankenheim, B. Franczak, P. Hulsmann, G. Moritz, C. Muhle, W. Vinzenz, et al. A new high-intensity synchrotron sis100 with strong bunch compression for gsi. In *Particle Accelerator Conference, 2001. PAC 2001. Proceedings of the 2001*, volume 5, pages 3278–3280. IEEE, 2001. 6

[41] K.Y. Ng. Space-charge effects on bunch rotation in the longitudinal phase space. In *Particle Accelerator Conference, 2001. PAC 2001. Proceedings of the 2001*, volume 4, pages 2893–2895. IEEE, 2001. 6

[42] Takashi Kikuchi, Mitsuo Nakajima, Kazuhiko Horioka, and Takeshi Katayama. Beam instability induced by space charge oscillation during final beam bunching for heavy ion inertial fusion. *Physical Review Special Topics-Accelerators and Beams*, 7(3):034201, 2004. 6

[43] T. Kikuchi, S.M. Lund, T. Katayama, and S. Kawata. Bunch compression in a ring for future riken projects. *Nuclear Instruments and Methods in Physics Research Section A: Accelerators, Spectrometers, Detectors and Associated Equipment*, 544(1-2):393–397, 2005. 6

[44] T. Kikuchi and K. Horioka. Beam behavior under a non-stationary state in high-current heavy ion beams. *Nuclear Instruments and Methods in Physics Research Section A: Accelerators, Spectrometers, Detectors and Associated Equipment*, 606(1-2):31–36, 2009. 6

[45] G. Franchetti, I. Hofmann, and G. Rumolo. Effect of space charge on bunch compression near the transition. *Physical Review Special Topics-Accelerators and Beams*, 3(8):084201, 2000. 6, 83, 84, 104

[46] K.Y. Ng. Space-charge effects on beam rotation at the compressor ring. Technical report, Fermi National Accelerator Laboratory (FNAL), Batavia, IL, 2013. 6, 83

[47] Ye Zou, Jingyu Tang, Jingfang Chen, Xiao Li, and Hong Sun. Short-bunch extraction in a rapid cycling synchrotron. *Physical Review Special Topics-Accelerators and Beams*, 17(6):060101, 2014. 6, 104

[48] J. Clerk Maxwell. A dynamical theory of the electromagnetic field. *Philosophical transactions of the Royal Society of London*, 155:459–512, 1865. 9

[49] John David Jackson. *Classical electrodynamics*. John Wiley & Sons, 2007. 10

[50] S.Y. Lee. *Accelerator physics*. World Scientific Publishing Co Inc, 2004. 11, 12, 15, 69, 86

[51] George William Hill. On the part of the motion of the lunar perigee which is a function of the mean motions of the sun and moon. *Acta mathematica*, 8(1):1–36, 1886. 11

[52] Gaston Floquet. Sur les equations differentielles lineaires. *Ann. ENS [2]*, 12(1883):47–88, 1883. 12

[53] http://mad.web.cern.ch/mad. 18, 45, 124

[54] Martin Reiser. *Theory and design of charged particle beams*. John Wiley & Sons, 2008. 21, 29, 32, 33, 44, 66

[55] Alexander Wu Chao, Karl Hubert Mess, Maury Tigner, and Frank Zimmermann. *Handbook of accelerator physics and engineering*. World scientific, 2013. 21

[56] Karlheinz Schindl. Space charge. (CERN-PS-99-012-DI):26 p, Mar 1999. 21

[57] J.A. MacLachlan. Longitudinal phase space tracking with space charge and wall coupling impedance. *Fermi National Accelerator Laboratory, FN-446,* 1987. 25

[58] Ronald C. Davidson. *Physics of nonneutral plasmas*. Imperial College Press London, 2001. 29

[59] A. Vlasov. On the kinetic theory of an assembly of particles with collective interaction. *Russ. Phys. J.*, 9:25–40, 1945. 29

[60] Tao Pang. An introduction to computational physics, 1999. 36

[61] M. Reiser. Periodic focusing of intense beams. *Part. Accel.*, 8:167–182, 1978. 37

[62] S.Y. Lee and A. Riabko. Envelope hamiltonian of an intense charged-particle beam in periodic solenoidal fields. *Physical Review E*, 51(2):1609, 1995. 40

[63] David Neuffer. Longitudinal motion in high current ion beams-a self-consistent phase space distribution with an envelope equation. *IEEE Transactions on Nuclear Science*, 26(3):3031–3033, 1979. 42, 43

[64] https://www.python.org. 45

[65] http://www.numpy.org. 46

[66] https://www.scipy.org. 46

[67] Roger W. Hockney and James W. Eastwood. *Computer simulation using particles*. crc Press, 1988. 46, 48

[68] C.K. Birdsall and A.B. Langdon. *Plasma physics via computer simulation*. CRC press, 2004. 46, 47, 125

[69] Ingo Hofmann and Oliver Boine-Frankenheim. Grid dependent noise and entropy growth in anisotropic 3d particle-in-cell simulation of high intensity beams. *Physical Review Special Topics-Accelerators and Beams*, 17(12):124201, 2014. 47

[70] Andrei Shishlo, Sarah Cousineau, Jeffrey Holmes, and Timofey Gorlov. The particle accelerator simulation code pyorbit. *Procedia Computer Science*, 51:1272–1281, 2015. 47, 54, 81, 87

[71] J.D. Galambos, J.A. Holmes, D.K. Olsen, A. Luccio, and J. Beebe-Wang. Orbit user manual version 1.10. *SNS/ORNL/AP Technical Note 011, Rev. 1*, 1999. 47

[72] Alexey Burov and Valeri Lebedev. Transverse instabilities of coasting beams with space charge. *Physical Review Special Topics-Accelerators and Beams*, 12(3):034201, 2009. 50

[73] G. Franchetti, I. Hofmann, and M. Aslaninejad. Collective emittance exchange with linear space charge forces and linear coupling. *Physical review letters*, 94(19):194801, 2005. 51, 104

[74] I. Hofmann and O. Boine-Frankenheim. Resonant emittance transfer driven by space charge. *Physical review letters*, 87(3):034802, 2001. 51

[75] I. Hofmann and G. Franchetti. Self-consistent study of space-charge-driven coupling resonances. *Physical Review Special Topics-Accelerators and Beams*, 9(5):054202, 2006. 51, 57

[76] Ingo Hofmann and Oliver Boine-Frankenheim. Parametric instabilities in 3d periodically focused beams with space charge. *Physical Review Accelerators and Beams*, 20(1):014202, 2017. 51, 75

[77] A. Goswami, P. Sing Babu, and V.S. Pandit. Beam dynamics and stability analysis of an intense beam in a continuously twisted quadrupole focusing channel. *The European Physical Journal Plus*, 131(11):393, 2016. 52

[78] Hong Qin, Moses Chung, and Ronald C. Davidson. Generalized kapchinskij-vladimirskij distribution and envelope equation for high-intensity beams in a coupled transverse focusing lattice. *Physical review letters*, 103(22):224802, 2009. 52

[79] R. Bär, I. Hofmann, P. Moritz, and U. Oeftiger. Measurement of space-charge-induced frequency shifts of quadrupolar beam oscillations in the sis. *Nuclear Instruments and Methods in Physics Research Section A: Accelerators, Spectrometers, Detectors and Associated Equipment*, 415(1):460–463, 1998. 104

[80] R. Singh, O. Boine-Frankenheim, O. Chorniy, P. Forck, R. Haseitl, W. Kaufmann, P. Kowina, K. Lang, and T. Weiland. Interpretation of transverse tune spectra in a heavy-ion synchrotron at high intensities. *Physical Review Special Topics-Accelerators and Beams*, 16(3):034201, 2013. 104

[81] K.M. Fung, M. Ball, C.M. Chu, B. Hamilton, S.Y. Lee, and K.Y. Ng. Bunch length compression manipulations. *Physical Review Special Topics-Accelerators and Beams*, 3(10):100101, 2000. 104

[82] John J. Barnard and Bojan Losic. Envelope modes of beams with angular momentum. Technical report, Lawrence Livermore National Laboratory (LLNL), Livermore, CA, 2000. 112

Yao-shuo Yuan

Curriculum Vitae

Schlossgartenstr.8
Darmstadt, 64289 Germany
☎ *(0049) 15902668543*
✉ *yuanyaoshuo@gmail.com*

Personal

- Date of Birth: March 15, 1987.
- Citizenship: China
- Languages: Chinese (native), English (fluent), German (basic)
- Hobbies: Table tennis, Jogging

Education

2014–2018	**PhD candidate**, *Technische Universität Darmstadt*, Darmstadt, Germany. Thesis title: Space-charge driven transverse beam instabilities in synchrotrons
2009–2014	**Master of Science in Physics**, *University of Chinese Academy of Sciences*, Beijing, China. Thesis title: Development of a simulation program for proton synchrotrons and its application on CSNS/RCS.
2005–2009	**Bachelor of Science in Physics**, *Northeast Normal University*, Changchun, China. Thesis title: Study of the number of the neutron yields in a D-T neutron tube.

Key publications

- Y. S. Yuan, O. Boine-Frankenheim, G. Franchetti and I. Hofmann, *Dispersion-Induced Beam Instability in Circular Accelerators*, Physical Review Letters, 118, 154801 (2017).
- Yao-Shuo Yuan, Oliver Boine-Frankenheim, and Ingo Hofmann, *Modeling of second order space charge driven coherent sum and difference instabilities*, Physical Review Accelerators and Beams 20, 104201 (2017).
- YUAN Yao-Shuo, LI Kai-Wei, WANG Na, Yoshiro Irie, WANG Sheng, *Study of the beam loading effect in the CSNS/RCS*, Chinese Physics C, 39, 047003 (2015).
- YUAN Yao-Shuo, WANG Na, XU Shou-Yan, YUAN Yue, WANG Sheng, *Theoretical study of a dual harmonic system and its application to the CSNS/RCS*, Chinese Physics C, 39, 127002 (2015).
- Yao-Shuo Yuan, Na Wang, Shou-Yan Xu, Sheng Wang, *A code for the optimization of RF voltage waveform and longitudinal beam dynamics simulation in an RCS*, Nuclear Instruments and Methods in Physics Research A, 729, pp 864-869 (2013).

Computer and software skills

- Programming Languages: C++, Python
- Operating system: Windows, Linux
- Office: MSOffice, LibreOffice, Latex